

**DISSERTATION**

**FIBER DELIVERY AND DIAGNOSTICS OF LASER SPARK IGNITION  
FOR  
NATURAL GAS ENGINES**

Submitted by

**Sachin Joshi**

Department of Mechanical Engineering

In partial fulfillment of the requirements

For the Degree of Doctor of Philosophy

Colorado State University

Fort Collins, Colorado

Fall 2008

UMI Number: 3346443

### INFORMATION TO USERS

The quality of this reproduction is dependent upon the quality of the copy submitted. Broken or indistinct print, colored or poor quality illustrations and photographs, print bleed-through, substandard margins, and improper alignment can adversely affect reproduction.

In the unlikely event that the author did not send a complete manuscript and there are missing pages, these will be noted. Also, if unauthorized copyright material had to be removed, a note will indicate the deletion.

**UMI**<sup>®</sup>

---

UMI Microform 3346443

Copyright 2009 by ProQuest LLC.

All rights reserved. This microform edition is protected against unauthorized copying under Title 17, United States Code.

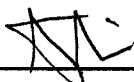
ProQuest LLC  
789 E. Eisenhower Parkway  
PO Box 1346  
Ann Arbor, MI 48106-1346

COLORADO STATE UNIVERSITY

November 7, 2008

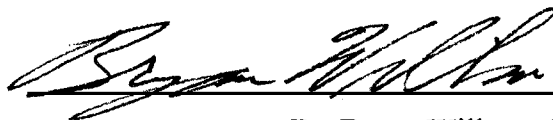
WE HEREBY RECOMMEND THAT THIS DISSERTATION PREPARED UNDER OUR SUPERVISION BY SACHIN JOSHI TITLED "FIBER DELIVERY AND DIAGNOSTICS OF LASER SPARK IGNITION FOR NATURAL GAS ENGINES" BE ACCEPTED AS FULLFILING IN PART REQUIREMENTS FOR THE DEGREE OF DOCTOR OF PHILOSOPHY.

Committee on Graduate Work



---

Dr. Azer Yalin, Advisor



---

Dr. Bryan Willson, Co-Advisor



---

Dr. Daniel Olsen, Committee Member



---

Dr. George Collins, External Committee Member



---

Dr. Allan Kirkpatrick, Head, Department of Mechanical Engineering

## **ABSTRACT OF DISSERTATION**

### **FIBER DELIVERY AND DIAGNOSTICS OF LASER SPARK IGNITION FOR NATURAL GAS ENGINES**

Laser ignition via fiber optic delivery is challenging because of the need to deliver pulsed laser beam with relatively high energy and sufficient beam quality to refocus the light to the intensity required for creating spark. This dissertation presents work undertaken towards the development of a multiplexed fiber delivered laser ignition system for advanced lean-burn natural gas engines. It also describes the use of laser ignition system to perform in-cylinder optical diagnostics in gas engines.

Key elements of the dissertation includes: i) time resolved emission spectroscopy (TRES) of laser sparks in air to investigate the dependence of spark temperatures and electron number densities on ambient gas pressures, ii) optical characterization of hollow core fibers, step-index silica fibers, photonic crystal fibers (PCFs) and fiber lasers, iii) development and on-engine demonstration of a multiplexer to deliver the laser beam from a single laser source to two engine cylinders via optical fibers, and iv) demonstration of simultaneous use of laser sparks for ignition and Laser Induced Breakdown Spectroscopy (LIBS) to measure in-cylinder equivalence ratios in a Cooperative Fuel Research (CFR) engine.

For TRES of laser sparks, the ambient gas pressure is varied from 0.85 bar to 48.3 bar (high pressures to simulate elevated motored in-cylinder pressures at time of ignition in advanced gas engines). At later stages ( $\sim 1\mu\text{s}$ ) of spark evolution, spark temperatures become comparable at all pressures. Electron number densities increase initially with increasing ambient gas pressure but become comparable at pressures greater than  $\sim 20$  bar. The effects of launch conditions and bending for 2-m long hollow core fibers are studied and an optimum launch  $f/\#$  of  $\sim 55$  is shown to form spark in atmospheric pressure air. Spark formation using the output of a pulsed fiber laser is shown and delivery of 0.55 mJ nanosecond pulses through PCFs is achieved. Successful multiplexed laser ignition of a CAT G3516C gas engine via hollow core fibers is shown. LIBS analysis conducted at equivalence ratios from 0.6 to 0.95 in the CFR engine show a linear variation and linear correlation ( $R^2 > 0.99$ ) of line intensity ratio ( $H_\alpha/O_{777}$  and  $H_\alpha/N_{\text{tot}}$ ) with equivalence ratio.

Sachin Joshi  
Department of Mechanical Engineering  
Colorado State University  
Fort Collins, CO 80523  
Fall 2008

## ACKNOWLEDGEMENTS

I would like to thank my parents, my brother and all my family members for their constant support throughout my life. I am privileged to have their love and encouragement. I cherish the memories of my late grandfather who passed away when I was concluding this Ph.D. program. He taught me to read and write.

I would like to thank Marty Malenshek, Nick Rancis and Adam Reynolds. Each played a vital role during this project. I also thank Kirk Evans and the engine control crew – Josh Schmitt, Morgan Kohls and Keegan Thompson who helped me during the engine testing. I would also like to thank Dr. Paul Puzinauskas of University of Alabama for his help during this work.

I am indebted to Dr. Bryan Willson and his family for their friendship, support and encouragement. I am thankful to Dr. Willson for giving me this opportunity to study here at CSU. I am very grateful to my mentor Dr. Azer Yalin for his guidance he provided me with during this work. Without his understanding, patience and insight, I couldn't have finished this program. I am also thankful to my other committee members for providing me with their help whenever I needed them. Additionally, I would like to acknowledge the funding support from Department of Energy, Caterpillar Inc. and Woodward Governor Company for this work.

I thank Hannah, her kids and many other people I have met during these past few years for inspiring me and for being there when I needed them.

Last but not the least, I am very thankful to Larissa and her daughter whom I met while I was pursuing this program. They were a constant source of joy, happiness and inspiration.

To my grandfather

&

Paree

# TABLE OF CONTENTS

## Chapter 1

Introduction and Background .....	1
1.1 Ignition Systems for High BMEP Gas Engines.....	2
1.2 Physics of Laser Ignition .....	5
1.2.1 Early Stages of Laser Spark Formation .....	5
1.2.2. Early Flame Growth and Ignition .....	7
1.2.3 Dependence of Breakdown Threshold on Pressure .....	9
1.2.4 Minimum Ignition Energy for Laser Ignition and Lean Limit .....	11
1.3 Laser Ignition Technology – Challenges and Opportunities .....	13
1.3 Goals and Scope of the Present Work.....	16
1.4 Outline of the Manuscript .....	17
References.....	19

## Chapter 2

Time Resolved Spectroscopic Study of Laser Sparks in Air at High Pressures .....	22
2.1 Introduction.....	23
2.2 Experimental Setup.....	26
2.3 Results and Discussions.....	29
2.3.1 Spark Temperature Measurements .....	32
2.3.2 Spark Electron Number Density Measurements.....	41
2.4 Conclusions.....	49
References.....	51

## Chapter 3

Experimental Study of Optical Fibers for Spark Delivery and Laser Ignition .....	
in Gases.....	54

3.1 Introduction.....	54
3.2 Optical requirements for Fiber Delivered Ignition .....	58
3.3 Hollow Core Fiber Testing .....	63
3.4 Photonic Crystal Fiber Testing .....	68
3.5 Solid Core Silica Fiber Testing.....	72
3.6 Fiber Lasers.....	78
3.7 Conclusions.....	79
References.....	82

## **Chapter 4**

Development of a Multiplexed Fiber Delivered Laser Ignition System for Natural Gas Engines.....	86
4.1. Introduction.....	87
4.2. Multiplexer Design and Benchtop Testing .....	89
4.3. System Integration .....	94
4.3.1 Selection of Laser Ignited Cylinders.....	94
4.3.2 Vibration Isolation .....	96
4.3.3 Multiplexer Control System.....	97
4.4. Preliminary Engine Test Results.....	99
4.5. Conclusions.....	101
References.....	102

## **Chapter 5**

Laser Induced Breakdown Spectroscopy for In-Cylinder Equivalence Ratio Measurements in Laser Ignited Natural Gas Engines.....	104
5.1. Introduction.....	105
5.2. Experimental Setup.....	109
5.2.1 Overview .....	109
5.2.1 Engine Set up .....	110
5.2.2 Optical Setup.....	111
5.2.3 Analysis of Spectra .....	113
5.3. Results and Discussion .....	115

5.3.1 Overview.....	115
5.3.2 Effect of Compression Ratios and Laser Energy.....	118
5.3.3 Signal to Noise and Variability.....	120
5.4. Conclusions.....	124
References.....	125

## **Chapter 6**

Conclusions and Future work .....	128
-----------------------------------	-----

# LIST OF FIGURES

Figure 1.1: Schlieren images of a turbulent flame kernel at 1 atmospheric pressure and $\Phi = 0.7$ in propane-air mixture for different time delays ( $t$ ) from the initial breakdown.....	8
Figure 1.2: Pressure dependence of breakdown field strength(E) .....	10
Figure 1.3:Plot of minimum ignition energy (MIE) and minimum pulse energy (MPE) for laser ignition. ....	12
Figure 2.1:Experimental Setup for laser spark diagnostics at ambient high pressures.....	27
Figure 2.2: Percentage of Laser energy absorbed by laser sparks at different ambient pressures. ....	30
Figure 2.3a:Emission spectra from laser spark at 0.85 bar. ....	32
Figure 2.3b:Emission spectra from laser spark at 34.5 bar.....	33
Figure 2.4: Example of a measured spectrum at 34.5 bar and $1\mu\text{s}$ gate delay and fit in 700 -780 nm region including contributions from individual peaks.....	35
Figure 2.5:Plasma temperature vs. delay for six pressures at incident laser pulse energy of 26 mJ .....	38
Figure 2.6: Ratio of plasma temperature at various delays and pressures. ....	40
Figure 2.7a: Emission spectra from laser sparks at 1 bar. ....	42
Figure 2.7b: Emission spectra from laser sparks at 34.5 bar. ....	43
Figure 2.8: Example of a measured spectrum at 34.5 bar and $1\mu\text{s}$ gate delay and fit in 644 - 674 nm region including contributions from the individual peaks.....	44
Figure 2.9:Temporal evolution of electron number density ( $n_e$ ) for different pressures. ....	46
Figure 2.10:Temporal evolution of electron number density ( $n_e$ ) for 0.85 bar, 20.7 bar and 34.5 bar.....	47
Figure 3.1: Schematic of the laser light exiting the fiber.....	59
Figure 3.2: Cross-sectional view of the coated hollow core fiber. ....	64
Figure 3.3: Schematic of the setup for 2m long hollow core fiber. ....	64

Figure 3.4: Large Mode Area solid core PCF fiber (from Crystal Fiber A/S).....	69
Figure 3.5: Experimental setup for photonic Crystal Fiber . .....	70
Figure 3.6: Transmission of a 25 $\mu$ m core LMA-PCF.....	71
Figure 3.7: Experimental setup for solid core fibers.....	73
Figure 3.8: Achievable focal intensity for the solid core fibers.....	77
Figure 3.9: Experimental setup of the fiber laser. ....	78
Figure 4.1: HeNe laser beam multiplexed into six spots using a galvo.....	89
Figure 4.2: Modified multiplexer for use with a step-and-hold galvanometer. ....	90
Figure 4.3: Optical spark plug. ....	91
Figure 4.4: Schematic of optics used in optical plug. ....	92
Figure 4.5: Diagram showing the engine from the top with the cylinders numbered. ....	95
Figure 4.6: Vibration isolation setup.. ....	96
Figure 4.7: Multiplexer system for Caterpillar G3516 C engine.....	97
Figure 4.8: Laser spark (tiny white light) and subsequent combustion (bright white flash) are shown in the bottom left and right pictures respectively.....	99
Figure 4.9: Pressure curves for laser ignited cylinder.....	100
Figure 5.1a: Experimental setup for laser ignition and LIBS. ....	109
Figure 5.1b: Experimental setup for laser ignition and LIBS on CFR engine.....	111
Figure 5.2: A single shot spectrum for $\Phi = 0.6$ and CR = 11 at energy level of 21mJ. ....	113
Figure 5.3: LIBS intensity ratio plotted against equivalence ratio ( $\Phi$ ) at CR =11 and input laser energy of 21mJ (data points are normalized to the initial value at $\Phi =0.6$ ).....	115
Figure 5.4: Integrated LIBS signal for $H_{\alpha}$ , $O_{777}$ and $N_{tot}$ plotted against equivalence ratio ( $\Phi$ ) at a CR = 9 and E = 26mJ.....	117
Figure 5.5: Line intensity ratios of $H_{\alpha}/O_{777}$ and $H_{\alpha}/N_{tot}$ plotted against equivalence ratio ( $\Phi$ ) at input energy level of 21 mJ. ....	118
Figure 5.6: Line intensity ratios of $H_{\alpha}/O_{777}$ and $H_{\alpha}/N_{tot}$ plotted against equivalence ratio ( $\Phi$ ) at CR = 9.....	119
Figure 5.7: Single shot line intensity ratios of $H_{\alpha}/O_{777}$ for $\Phi =0.6$ and $\Phi =0.7$ at CR =11. Solid lines are the average values of intensity ratios. ....	121
Figure 6.1: a) A combination of an EOM and a beam splitter to change the beam direction, b) Multiple EOMs and beam splitters for multiplexing the laser beam from a single source to multiple fibers.....	130

## LIST OF TABLES

Table 2.1: Relevant atomic data for the observed spectral lines. ....	29
Table 3.1: Calculated FOM values for different fibers. ....	61
Table 3.2: Effect of Launch Geometry on 2 m Long Hollow Waveguides. ....	66
Table 3.3. Effect of Bending Configuration for input $f_{\#} = 55$ . ....	67
Table 3.4: Beam properties at the solid core step index fiber exit. ....	75
Table 3.5: Safe Energy limit for solid core step index fiber. ....	76
Table 4.1: Measured transmission (%) for individual components of the multiplexer unit.....	93
Table 5.1: Relevant atomic data for the observed spectral lines. ....	114

# Chapter 1

---

## Introduction and Background

The focus of this dissertation is on research and development of a practical laser ignition system for stationary natural gas engines typically used for power generation and natural gas compression. A number of studies on laser ignition of gas engines have reported on the ability of laser ignition to extend the lean operation limit, reduce exhaust emissions and increase engine efficiency<sup>1-4</sup>. Despite these benefits, the laser ignition technology is still not used in industrial environments due to lack of robust and cost effective practical methods to deliver the megawatt peak power pulsed laser beam from a laser source to the engine cylinders. This dissertation reports on the initial steps taken to fulfilling this gap.

## 1.1 Ignition Systems for High BMEP Gas Engines

In order to achieve high efficiencies, stationary reciprocating natural gas engines need to be operated at high brake mean effective pressure (BMEP) levels<sup>4</sup>. The US Department of Energy's emissions and efficiency target for reciprocating stationary gas engines from 0.5 megawatt (MW) to 6.5 MW by 2010 is: nitrous oxide ( $\text{NO}_x$ ) < 0.1 g/bhp-hr (0.134 g/kW-hr) and brake thermal efficiency  $\geq 50\%$ <sup>5</sup>. These two targets can be achieved by operating gas engines at lean conditions (low equivalence ratio) and at high BMEP levels (for e.g. by using high intake boost)<sup>4,6-8</sup>. Lean operation of gas engines leads to low in-cylinder combustion temperatures resulting in low  $\text{NO}_x$  emissions<sup>9</sup>. Use of high intake boost or Miller Cycle in the high BMEP engines at lean equivalence ratios results in increased thermal efficiencies<sup>9</sup>. However, operation of gas engines at very lean conditions can also result in increased misfire rates<sup>8</sup>. Hence, high BMEP engines need to be operated at optimum lean fuel-air mixture conditions and optimum boost levels (to avoid knocking).

One of the key areas that needs to be addressed for reliable lean operation of these high BMEP modern gas engines is ignition<sup>4,7,10-12</sup>. Conventional ignition systems that use electric spark plugs do not operate reliably at targeted high in-cylinder pressures and lean conditions<sup>4</sup>. Consistent with Paschen's law, for a fixed spark plug gap (say,  $\sim 0.3\text{mm}$ ) high voltages are required to create sparks at high pressures<sup>13</sup>. High voltage requirements ( $\sim 15\text{-}20\text{ kV}$ ) can lead to a rapid deterioration (erosion) of spark plug electrodes (such as due to sputtering)<sup>14</sup>. It also leads to dielectric breakdown of the secondary ignition wires due to their insufficient dielectric strength to deliver high energy (high voltages) to the

spark plug gaps<sup>4,11,12</sup>. Spark plugs can be operated at high pressures with smaller spark gaps to reduce the voltage requirements. However, small spark plug gaps result in small electric sparks which are more prone to quenching effects from the spark plug electrodes. This results in insufficient ignition energy being delivered to the plasma and hence, results in increased misfires in lean fuel-air mixtures<sup>15</sup>. Hence, electric spark plugs cannot operate lean high BMEP engines to meet the efficiency, emissions and maintenance cost requirements<sup>4</sup>.

However, a number of potential ignition technologies do exist for high BMEP modern gas engines such as, (i) Laser Ignition, (ii) Pre-combustion Chamber, (iii) Radio Frequency Electrostatic Ignition and (iv) Micro-Pilot Ignition.

Pre-combustion chambers are high ignition energy sources to ignite lean fuel-air mixtures. A pre-combustion chamber consists of a small chamber with its own fuel supply system and is attached to the main combustion chamber<sup>16</sup>. Unlike the lean fuel-air mixture in the main combustion chamber, the pre-combustion chamber receives a nearly stoichiometric fuel air mixture which is compressed along with the fuel-air mixture in the main combustion chamber and ignited by an electric spark plug. Note that it is easier to ignite stoichiometric mixtures than lean mixtures<sup>14</sup>. The resulting flame jet coming out of the pre-combustion chamber nozzle then acts as an ignition source for combustion of lean mixtures inside the main combustion chamber. However, as discussed earlier, raising the BMEP of the engine increases the overall compression pressure and thermal overload of the spark plugs resulting in a shorter spark plug life.

Radio frequency ignition system utilizes a tuned circuit consisting of a secondary coil (with its inductance and capacitance) and an insulated electrode installed in the

combustion chamber. The insulated electrode and the combustion chamber walls together act as a “discharge capacitor” which has its own capacitance. This tuned circuit is operated at a resonance frequency between 50 – 2000 kHz by a primary coil resulting in a large radio frequency alternative current (AC) between the electrode and the combustion chamber. This highly energetic large AC ionizes the fuel air mixture and forms multiple flame initiation spots inside the combustion chamber<sup>15</sup>. This patented technology is still in development phase and not much published work is available.

Micro-Pilot ignition utilizes the auto-ignition characteristics of small amount of diesel fuel or engine oil injected into the main combustion chamber to ignite lean fuel/air mixtures. Although this system replaces the spark plugs, it requires its own different fuel and supply system. This system is still in development phase and has been tested only on low BMEP low speed gas engines<sup>17</sup>.

Laser ignition system, on the other hand, utilizes a combustion initiating spark formed by tightly focusing a high power pulsed laser beam inside an engine cylinder. Unlike conventional electric sparks, with suitable focusing optics, laser sparks can be freely located anywhere inside a combustion chamber for optimized combustion<sup>18</sup>. Advantages of a laser spark stem from its characteristically different early plasma property compared to conventional electric spark, such as hotter temperature (>100,000 K), higher flame speed<sup>19,20</sup> and also due to the obviation of the spark plug electrodes which otherwise act as quenching surfaces for the sparks<sup>20</sup>. Furthermore, laser spark formation becomes easier at elevated pressures (the breakdown threshold intensity decreases and is discussed in detail in Section 1.2.3. Past research on laser ignition in engines have shown shorter ignition delays and stable combustion at lean conditions<sup>4,7</sup>.

Laser ignition system also allows for collection of light emission from laser sparks as well as combustion flame to perform optical combustion diagnostics. The laser beam that is delivered to an engine cylinder is generally intense enough at the window (~ 0.2 – 0.5 J/cm<sup>2</sup> for nanosecond pulses) for self cleansing of the window, i.e, the optical window is kept clear of the combustion products such as soot, oil etc by the intense laser beam<sup>4,21</sup>. Hence, unlike the other ignition systems described earlier, the laser ignition technology allows for real time in-situ in-cylinder combustion diagnostics to monitor equivalence ratio of fuel-air mixtures, misfires etc which are essential for robust operation control of lean burn high BMEP engines.

## **1.2 Physics of Laser Ignition**

When radiation of sufficient intensity is focused on solids, liquids or a volume of gas, the medium breaks down and a hot and dense plasma is formed. The plasma formed in a gaseous volume is termed as a “laser spark” The first observation of gas breakdown by a laser beam was reported by Maker et al.(1963)<sup>22</sup> and Meyerand and Haught(1963)<sup>23</sup>.

### **1.2.1 Early Stages of Laser Spark Formation**

A number of theories exist for the initial breakdown (laser spark formation) mechanisms, such as multiphoton ionization, non resonant cascade breakdown etc<sup>19, 24-26</sup>. Multiphoton ionization is a process by which ionization of atoms is achieved by simultaneous absorption of several quanta of light. However, the ionization energy for most gases is in the range of 10 -20 eV and the required laser beam intensity to detach an electron in the focal volume is approximately equal to the experimentally measured

breakdown thresholds<sup>25</sup>. Hence, this process can only cause appearance of initial priming electrons and is not believed to be the main mechanism for the observed laser spark formation<sup>19,25,27,28</sup>. The most common mechanism for laser spark formation for nanosecond pulses (5 ~ 10ns) and 1064 nm laser radiation is the non-resonant breakdown (or electron-impact ionization)<sup>28</sup>. This mechanism is initiated by a few seed electrons which are either present as impurities (or produced by multiphoton ionization of already small amount of ionized gas present due to cosmic rays or natural radioactive of the earth<sup>25</sup>). These primary electrons absorb energy from the laser beam radiation through electron-neutral inverse bremsstrahlung collisions but also lose energy through elastic and inelastic collisions with neutral particles, diffusion and electron recombination. Nonetheless, in the presence of high laser intensity some electrons gain enough energy that exceeds the ionization energy of atoms in the gas. As a result, the electrons ionize neutral atoms and leads to creation of secondary electrons. This process of creation of secondary electrons through repetitive collision process is called electron cascade which leads to an avalanche growth and initial breakdown<sup>6,29</sup>. Following the initial ionization, electron-neutral or electron-ion (inverse bremsstrahlung) process leads to absorption of laser energy resulting in formation of a robust laser spark with high initial temperatures (>100,000 K) and pressures (>1000 bar)<sup>20,30,31</sup>. A short review on physics of laser ignition is presented in the following section. A more detailed review of laser ignition physics can be found in [20] and references therein.

### 1.2.2. Early Flame Growth and Ignition

Laser ignition is achieved by focusing the output of a high power pulsed laser source into a tiny focal volume. Since, the energy deposition in the spark is very rapid (5-10ns) and the plasma temperatures and pressures are high, an elongated ellipsoidal shock wave propagates from the spark volume and detaches from the plasma within 0.3 - 0.5 $\mu$ s<sup>19,20</sup>. This shock wave carries away a significant amount of the deposited laser energy (~50 -70% of total laser energy)<sup>31</sup>. Within a short duration of 15 – 50  $\mu$ s<sup>20</sup> the shock wave dissipates into a sound wave and the plasma kernel expands so as to obtain an approximately uniform temperature (albeit higher temperatures ~ 10,000 K than surrounding gas ) and pressures (ambient pressure)<sup>31</sup>. Instead of playing a direct role in the flame development, the shock wave is believed to radially spread the energy and help in inducing better mixing of reactive mixtures during its propagation through the medium<sup>31</sup>. A propagating flame structure doesn't appear till a longer duration (~ 100 – 300  $\mu$ s). Although it is hard for one to pinpoint the exact time for transition from plasma kernel to flame kernel, the time duration for transition of plasma kernel to flame kernel is taken as an initial few hundred microseconds (100-300 $\mu$ s) and combustion after few milliseconds from initial breakdown<sup>20</sup>.

After the initial plasma kernel expansion and shock wave dissipation, the plasma kernel undergoes a series of gas dynamic effects. As a result, the plasma kernel obtains a toroidal volume (with two counter rotating toroidal rings) due to outward propagation of a rarefaction wave. This rarefaction wave causes the pressure in the plasma kernel to drop below ambient pressure prior to returning to ambient pressures. This results in formation

of a third lobe (in an opposite direction to the laser beam propagation). The time scale for these phenomena is between 15 and 100  $\mu\text{s}$  after initial breakdown.

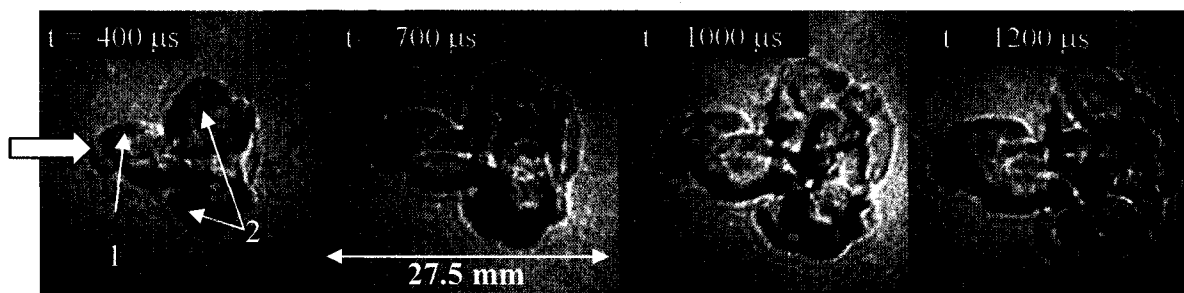


Figure 1.1: Schlieren images of a turbulent flame kernel at 1 atmospheric pressure and  $\Phi = 0.7$  in propane-air mixture for different time delays ( $t$ ) from the initial breakdown<sup>20</sup>. The arrow shows the direction of the laser beam propagation.

Figure 1.1 shows an already developed flame kernel in an igniting turbulent propane-air mixture. As can be seen from the figure, the flame kernel has a toroidal volume with two lobes on either side (labeled 1) and a third lobe (labeled 2). The time duration for these structures depends on the turbulence in the medium (with shorter duration for high turbulence). These structures are thought to have a significant influence on early flame propagation.

Studies conducted by Bradley et al.<sup>20</sup> on laser ignition of propane air mixtures showed that during initial stages of flame kernel development, the kernel propagates with flame speeds that exceed the laminar flame speed (termed as “overdriven flame speeds”). This overdrive is strongest in lean mixtures resulting in a sustained flame growth despite initial high flame stretch at early times. This overdriven flame speed phenomenon observed in laser ignited flames is in contrast to flames produced by conventional low

energy electric spark ignition, where flame speeds start at a comparatively lower value at early times and reach the laminar flame speed. Hence, flames produced by conventional ignition systems in lean conditions are more prone to extinction at early times.

Based on the physics of early flame development, laser ignition is a more robust ignition source than conventional electric ignition source for igniting lean fuel-air mixtures where high flame stretch (enhanced in turbulent ambient conditions) at early times can quench the flame. These benefits make laser ignition a suitable ignition source for stationary high BMEP natural gas engines and gas turbine engines where igniter lifetime is a limitation<sup>32</sup> and aircraft engines where flame extinction and relighting in adverse high altitude can be problematic.

### **1.2.3 Dependence of Breakdown Threshold on Pressure**

Typical breakdown threshold intensities ( $I_{thr}$ ) required to create laser sparks at atmospheric air has been observed to be  $\sim 300\text{GW/cm}^2$ <sup>4,6,12,29,3-35</sup>. The breakdown threshold intensity depends on various factors such as (i) type of gas, (ii) laser frequency and (iii) ambient pressure, the latter having the most dominant effect<sup>19</sup>. Consistent with the electron impact ionization theory for the breakdown (discussed in Section 1.2.1), the breakdown threshold intensity decreases with increasing pressures (as a result of higher collision frequency and ionization). Figure 1.2 shows the pressure dependence of breakdown field strength (E).

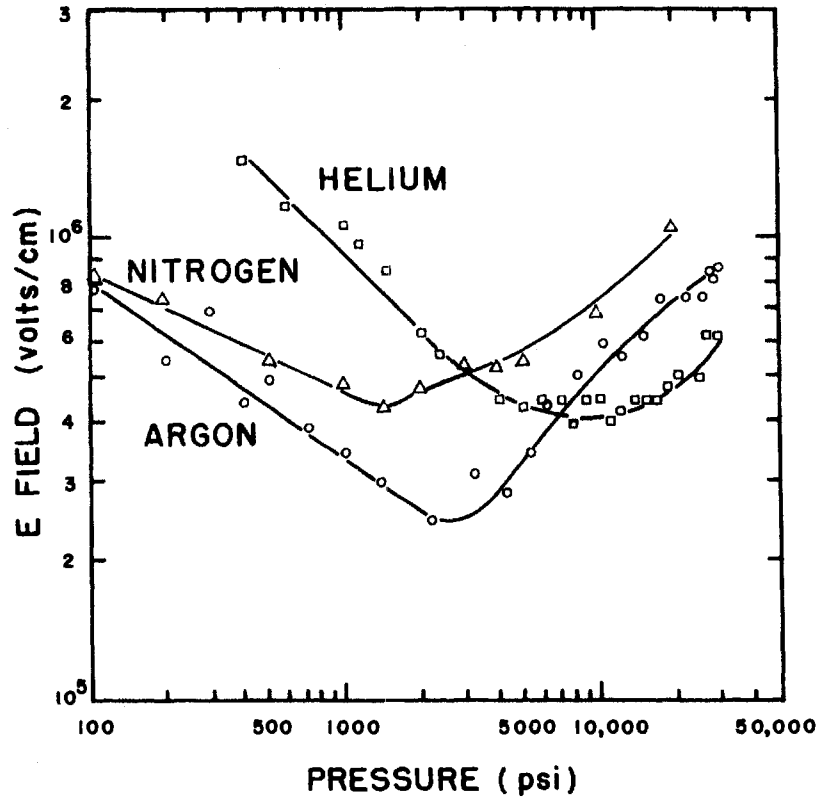


Figure 1.2: Pressure dependence of breakdown field strength ( $E$ )<sup>28</sup>.

In Fig. 1.2, the breakdown electric field strength ( $E$ ) is plotted versus different pressures for helium, nitrogen and argon. Note that the intensity is related to electric field strength by  $I_{thr} \propto E^2$ . The observed minima in the breakdown field strength occurs when the frequency of the light radiation equals the electron momentum-transfer collision frequency with neutrals<sup>28</sup>.  $I_{thr}$  approximately follows  $I_{thr} \propto p^k$ , where  $p$  is the ambient pressure and  $k$  varies from -0.3 to -0.9, depending on gas, frequency of the laser etc<sup>36</sup>. Compared to the threshold intensity of  $\sim 300 \text{ GWcm}^{-2}$  in atmospheric air,  $I_{thr}$  now becomes significantly lower for pressures of interest (approximately 15 bar - 50 bar at ignition timing for high BMEP engines). This suggests lower laser energy requirement

for creating laser sparks at higher pressures. However, as will be discussed in the following Section 1.2.4, laser ignition in engines requires a higher amount of laser energy (than that required for initial spark formation) for sustained flame growth in lean conditions.

### 1.2.4 Minimum Ignition Energy for Laser Ignition and Lean Limit

For a simplified ignition analysis for a point spark, we can define a critical spherical gas-volume radius ( $R_{cr}$ ) such that the flame will not propagate if the actual radius is smaller than this<sup>37</sup>. Considering the conduction losses to the cold unburnt gases (quenching)), the critical volume radius becomes,

$$R_{cr} = a \frac{\alpha}{S_L} \quad (1)$$

where,  $a > 1$ ,  $\alpha$  is the thermal conductivity of the gas and  $S_L$  is the laminar flame speed.

The minimum ignition energy (MIE), assuming the energy added by the spark is to heat the critical volume to a burned gas temperature, then becomes,

$$MIE \propto P \frac{c_p}{R_b} \frac{(T_b - T_u)}{T_b} \left( \frac{\alpha}{S_L} \right)^3 \quad (2)$$

where,  $c_p$  is the specific heat capacity,  $P$  is the ambient pressure,  $T_u$  is the unburnt gas temperature,  $T_b$  is the burnt gas temperature,  $\alpha$  is the gas thermal conductivity and  $S_L$  is the laminar flame speed. Note that the effect of pressure on MIE is the direct influence of  $P$  as shown in eqn. 2 and through indirect influences buried in  $\alpha$  and  $S_L$  resulting in an

inverse relationship between MIE and the square of ambient pressure. So, at higher pressures, low MIE is required. The effect of equivalence ratio on the MIE is through an indirect effect on the flame temperature that affects the laminar flame speed,  $S_L$ . For methane,  $S_L$  is maximum at a slightly rich mixture and falls off on either side<sup>37</sup>. For stoichiometric methane-air mixtures, typical value of MIE with electric spark ignition is around 0.4 - 1 mJ<sup>14</sup>. However, MIE for laser ignition is significantly higher and is likely to be associated with a larger spark volume ( 2-3mm<sup>3</sup>), shock losses and radiative losses<sup>24,31</sup>.

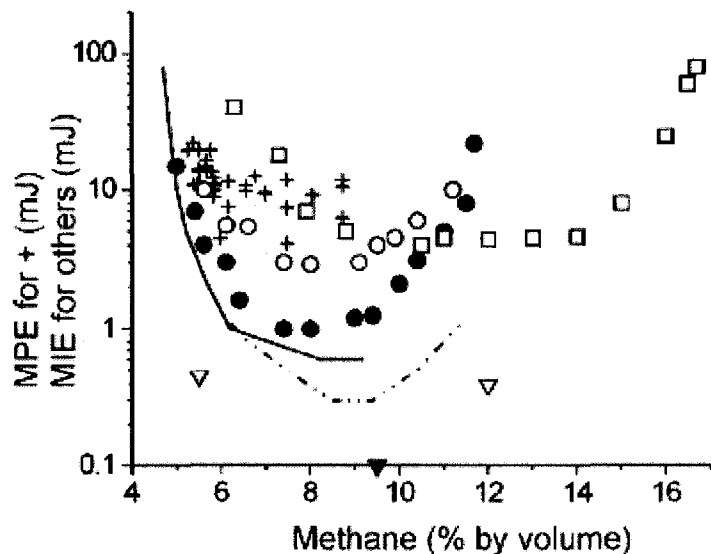


Figure 1.3: Plot of minimum ignition energy (MIE) and minimum pulse energy (MPE) for laser ignition. Data labeled as “+”, black dots (ns), circles (ps), squares, and line are for laser ignition whereas, the dotted line is for conventional spark and black triangles are for computations<sup>6</sup>. (Methane % by volume at stoichiometric condition is 9.5% and is indicated by an solid inverted triangle; lower flammability limit for methane is  $\Phi = 0.46$  or, 5% of methane by volume).

Figure 1.3 shows the minimum ignition energy and minimum pulse energy required for laser ignition and conventional electric spark ignition. The crosses are for 30

bar pressure conditions whereas the rest is for atmospheric condition. As can be seen from the figure, both MIE and MPE increases for lean as well as rich mixtures and is the lowest at around stoichiometric conditions. Based on this figure, MIE and MPE required for laser ignition can be taken as 15-20 mJ for igniting lean fuel air mixtures (% of methane by volume < 6%). As will be discussed in Chapter 2, this energy requirement becomes the driving factor for selection of appropriate laser delivery method for laser ignition.

The lower flammability limit (or, “lean limit”) for methane air mixture is  $\Phi = 0.46$  (or 5% of methane by volume<sup>38</sup>). However, the experimental lean limits for methane–air mixtures for laser ignition varies from equivalence ratio ( $\Phi$ ) of 0.4545 to 0.513<sup>10,39</sup> (depending on the experimental conditions). Kopecek et al. have shown successful laser ignited engine operation with  $\Phi$  only above of 0.47619. They obtained the lowest NO<sub>x</sub> values of 0.22 g/kWh (or, 0.16 g/bhp-h) at  $\Phi$  of 0.4878<sup>10</sup>.

### **1.3 Laser Ignition Technology – Challenges and Opportunities**

Initial study for the use of lasers for combustion was done in the late 1960s<sup>40</sup>. The first laser ignited engine was run on a CO<sub>2</sub> laser by J.D. Dale in 1979<sup>1</sup>. Subsequent work by other researchers have shown the potential of laser ignition to extend the operational limit of the engine into a leaner operation region with potential reduced NO<sub>x</sub> emissions benefits<sup>4, 41</sup>.

All of the published works concerning laser ignition system have used open-beam path delivery in which mirrors mounted in free space were used to guide a laser beam in the air from a laser into the engine cylinders. This approach is not suitable for practical

use on engines because of thermal, vibration and safety issues. A cost effective and safe laser ignition system can be based on a fiber delivery method in which a laser beam is delivered from a single laser source to multiple engine cylinders via optical fibers. With a multiplexer to switch the laser beam to different locations (fibers), a single laser source can be multiplexed to many different cylinders, hence eliminating the need of many lasers. As will be discussed later in Chapter 3, there are other approaches but are currently not cost effective and hence the fiber delivery approach is a part of the focus of this study.

With fiber delivery approach, the biggest technical challenge is to successfully deliver laser pulses with enough ignition energies without exceeding the damage threshold (tens of mJ) of the fibers. This situation is further constrained by the need to deliver laser pulses with sufficient beam quality ( $M^2$ )<sup>42</sup> at the fiber output (the fibers degrade the beam quality) so that it can be focused to a required breakdown threshold intensity ( $\sim 300 \text{ GW/cm}^2$ ) at atmospheric air. First successful laser spark in atmospheric air via a 1 m long coated hollow core fiber (with 700  $\mu\text{m}$  core diameter using 1064nm light) was demonstrated by Yalin et al<sup>12</sup>. They also demonstrated a successful laser ignited single cylinder engine operation with a 1m long and 1000  $\mu\text{m}$  core diameter coated hollow core fiber<sup>43</sup>.

Based on the above mentioned accomplishments and challenges, there exists opportunities to further enhance the development of fiber delivery laser ignition systems. With new developments in the areas of photonic crystal fibers (PCFs) and fiber lasers, high power transmission is possible with minimum laser beam quality ( $M^2$ ) degradation. These developments provide an opportunity to demonstrate a potential practical fiber

delivery method with a multiplexer and suitable multiple fibers for delivering laser sparks to multiple engine cylinders.

As was discussed in Section 1.2.2, there exists a big time window between initial spark formation (breakdown) and combustion (hundreds of  $\mu\text{s}$  to few ms). During the later stages of spark kernel development ( $\sim 1\mu\text{s}$ ), the spark plasma is still very hot ( $\sim 10,000\text{ K}$ ) for highly excited ions, atoms and electrons to exist in a large density. When these excited species cool down, they emit light characteristic to their transition frequencies. These light emissions can be used for determining species concentration inside the spark focal volume. Based on the light intensity ratios, it then becomes possible to determine the equivalence ratios of the fuel-air mixture inside the engine cylinder. This technique is termed as Laser Induced Breakdown Spectroscopy (LIBS). Although LIBS has been routinely used for solid and liquid –phase LIBS (where breakdown thresholds are a magnitude lower), gas-phase LIBS do not currently use fiber delivery. Since, laser ignition provides a “window” into the combustion chamber, one can potentially use LIBS and optical emission spectroscopy (from combustion flame) to monitor knock formation<sup>44</sup>, ignition vitality, equivalence ratio<sup>45</sup> etc.

In order to conduct LIBS in high pressure environments (expected in engines), one needs to have a basic understanding of plasma environment at high pressures. No detailed published works on effect of high engine like pressures on laser plasmas exist. This study is important in order to assess the plasma environment (i.e, temperature and electron number density) that can have a significant effect on the light intensity emitted from the plasma and hence on LIBS calibration issues. Hence, detailed spectroscopic investigation of plasma at high pressures is needed. Furthermore, to our knowledge, no

published works exist on simultaneous laser ignition and LIBS to monitor in-cylinder equivalence ratios.

### **1.3 Goals and Scope of the Present Work**

Given this background, the goal of this work was to develop a laser ignition system based on fiber delivery and to show in-cylinder optical diagnostics capability of the laser ignition system. In order to meet these objectives, it was desired to:

1. investigate the effect of high engine like pressures on plasma environment (temperature and electron number density) through spectroscopic methods,
2. investigate potential candidate fibers capable of fiber delivery of laser sparks with required ignition energies,
3. develop and demonstrate a multiplexed laser ignition system on an engine, and
4. demonstrate LIBS on a laser ignited engine cylinder for monitoring of in-cylinder equivalence ratios.

Having determined the objectives of this research work, it was also important to clearly identify the scope as well. For conducting experiments on the effect of high pressures on laser spark characteristics, the pressures selected was between 1 bar and ~ 48 bar (characteristic of engine pressures at ignition timing). It is well known that the evolution of plasma temperature and electron number density is coupled through radiation losses, diffusion, plasma volume expansion and electron recombination. The plasma temperature and electron density also depends on the laser input energy, focal volume etc. An investigation into contribution of these individual factors to plasma temperature and electron density itself can become a major study. Hence, only a general

discussion of the effect of pressure on evolution of plasma temperature and electron density at a fixed input laser energy level was conducted. The number of laser ignited engine cylinders that can be multiplexed depends on the available repetition rate of the laser. Since the available laser was capable of running only at 30 Hz, only two cylinders of a natural gas CAT G3516C engine with 1800 rpm engine speed were laser ignited. To demonstrate LIBS for measuring in-cylinder equivalence ratio in an engine, a single cylinder cooperative fuel research (CFR) gas engine was ignited with laser ignition. Since this work focused primarily on LIBS, no detailed work was done to analyze the combustion and emissions as a result of laser ignition.

#### **1.4 Outline of the Manuscript**

Chapter 2 presents the experimental investigation of laser spark environment in high pressures. Results from spectroscopic techniques to measure plasma temperature and electron number density (from few hundred nanoseconds to few microseconds from the onset of the laser spark) are discussed. Chapter 3 discusses few other laser ignition system approaches by other researchers. An analytical figure of merit approach to determine the suitability of solid core fibers, hollow core fibers, photonic crystal fibers and fiber lasers is presented. Results from investigation into transmission characteristics of these fibers are shown. Chapter 4 presents the design and development of a multiplexer made in co-operation with Woodward Industrial, Fort Collins. Initial results from on-engine testing are presented. Chapter 5 presents the experimental investigation conducted in a single cylinder CFR engine to demonstrate simultaneous laser ignition and

LIBS. A linear correlation between the measured equivalence ratio and LIBS intensity ratios at different compression ratios and laser energy levels is shown.

This dissertation is written in a form so that each chapter is complete within itself and hopefully is a journal/conference paper.

## References

1. J. D. Dale, P. R. Smy, and R. M. Clements, "Laser ignited internal combustion engine-an experimental study," SAE (SAE Paper 780329), 1539-1548 (1979).
2. M. Weinrotter, H. Kopecek, M. Tesch, E. Wintner, M. Lackner, and F. Winter, "Laser ignition of ultra-lean methane/hydrogen/air mixtures at high temperature and pressure," *Exptl. Therm. and Fluid Sci.* **29**, 569-577 (2005).
3. A. Stakhiv, R. Gilber, H. Kopecek, A. M. Zheltikov, and E. Wintner, "Laser ignition of engines via optical fibers?" *Laser Phys.* **14**, 738-747 (2004).
4. G. Herdin, J. Klausner, E. Wintner, M. Weinrotter, and J. Graf, "Laser ignition-a new concept to use and increase the potentials of gas engines," in *ASME Internal Combustion Engine Division 2005 Fall Technical Conference*, (2005), pp. 1-9.
5. [http://www.eere.energy.gov/de/gas\\_fired/projects.html](http://www.eere.energy.gov/de/gas_fired/projects.html).
6. H. Kopecek, H. Maher, G. Reider, F. Winter, and W. E., "Laser ignition of methane-air mixtures at high pressures," *Exptl. Therm. and Fluid Sci.* **27**, 499-503 (2003).
7. B. Bihari, S. Gupta, R. Sekar, J. Gingrich, and J. Smith, "Development of advanced laser ignition system for stationary natural gas reciprocating engines," presented at the ASME Internal Combustion Engine Division 2005 Fall Technical Conference, Ottawa, Canada, Sept 11-14, 2005, 2005.
8. H. M. Cho and B.-Q. He, "Spark ignition natural gas engines - A review," *Energy Conversion and Management* **48**, 608-618 (2007).
9. J. B. Heywood, *Internal Combustion Engine Fundamentals* (1988).
10. H. Kopecek, S. Charareh, M. Lackner, C. Forsich, F. Winter, J. Kausner, G. Herdin, and E. Wintner, "Laser Ignition of Methane-Air Mixtures at High Pressure and Diagnostics," *Jnl. of Eng. for Gas Turb. and Power* **127**, 213-219 (2005).
11. M. McMillian and e. al., "Laser-Spark Ignition for Natural Gas Fueled Reciprocating Engines," presented at the Gas Machinery Conference, 2003.
12. A. P. Yalin, M. Defoort, B. Willson, Y. Matsuura, and M. Miyagi, "Use of hollow-core fibers to deliver nanosecond Nd:YAG laser pulses to form sparks in gases," *Optics Letters* **30**(16), 2083-2085 (2005).
13. J. A. Rees, ed., *Electrical Breakdown in Gases* (1973).

14. J. C. Hilliard and G. S. Springe, eds., *Fuel Economy in Road Vehicles Powered by Spark Ignition Engines* (1984).
15. P. D. Freen, "Radio Frequency Electrostatic Ignition System Feasibility Demonstration," (Etatech, Inc., 2005).
16. K. Hideo, "Engine with precombustion chambers," (1996).
17. E. D. Ted Bestore, "Annual Report - Improvement to Pipeline Compressor Engine Reliability through Retrofit Micro-Pilot Ignition System - PHASE I, <http://www.osti.gov/bridge/servlets/purl/823051-m75LcK/native/823051.pdf>," (Colorado State University, 2003).
18. D. L. Ahrens and Colorado State University. Dept. of Mechanical Engineering., "Development of an open path laser ignition system for a large bore natural gas engine," Thesis (M.S.) (Colorado State University, 2005., 2005).
19. G. V. Ostrovskaya and A. N. Zaidel, "Laser spark in gases," *Soviet Physics Uspekhi* **16**, 834-855 (1973).
20. D. Bradley, C. G. W. Sheppard, I. M. Suardjaja, and R. Wooley, "Fundamentals of high-energy spark ignition with lasers," *Combustion and Flame* **138**, 55-77 (2004).
21. T. X. Phuoc, "A comparative study of the photon pressure force, the photophoretic force, and the adhesion van der Waals force," *Opt. Commun.* **245**, 27-35 (2005).
22. P. D. Maker, R. W. Terhune, and C. M. Savage, presented at the Quantum Electronic Conference, Paris, 1963.
23. R. G. Meyerand and A. F. Haught, "Optical-Energy Absorption and High-Density Plasma Production," *Phys. Rev. Lett* **13**, 7-9 (1964).
24. P. D. Ronney, "Laser versus conventional ignition of flames," *Opt. Eng.* **33**, 510-521 (1994).
25. L. J. Radziemski and D. A. Cremers, eds., *Laser-induced plasmas and applications* (1989).
26. C. G. Morgan, "Laser-induced breakdown of gases," *Rep. Prg. Phys.* **38**, 621-665 (1975).
27. R. W. Minck, "Optical Frequency Electrical Discharges in Gases," *Communications, Journal of Applied Physics* (1963).
28. D. H. Gill and A. A. Dougal, "Breakdown minima due to electron-impact ionization in super-high-pressure gases irradiated by a focused giant -pulse laser," *Physical Review Letters* **15**(22), 845-847 (1965).
29. T. X. Phuoc and F.P.White, "Laser-Induced Spark Ignition of CH<sub>4</sub>/Air Mixtures," *Combustion and Flame* **119**, 203-216 (1999).
30. Y. L. Chen and J. W. L. Lewis, "Visualization of laser-induced breakdown and ignition," *opt. Exp.* **9**, 360-372 (2001).

31. T. X. Phuoc, "An experimental and numerical study of laser-induced spark in air," *Opt. and Lasers in Eng.* **43**(113-129)(2005).
32. J. D. Few and J. W. L. Lewis, "Gas turbine photon ignition system," 7947640 (1989).
33. I. C. E. Turcu, M. C. Gower, and P. Huntington, "Measurement of KrF laser breakdown threshold in gases," *Opt. Commun.* **134**, 66-68 (1997).
34. J. P. Davis, A. L. Smith, C. Giranda, and M. Squicciarini, "Laser-induced plasma formation in Xe, Ar, N<sub>2</sub>, and O<sub>2</sub> at the first four Nd:YAG harmonics," *Applied Optics* **30**, 4358-4364 (1991).
35. R. Tambay and R. K. Thereja, "Laser-induced breakdown studies of laboratory air at 0.266, 0.355, 0.532, and 1.06  $\mu\text{m}$ ," *J. Appl. Phys.* **70**, 2890-2892 (1991).
36. A. Sircar, R. K. Dwivedi, and R. K. Thereja, "Laser induced Breakdown of Ar, N<sub>2</sub>, and O<sub>2</sub> gases using 1.064, 0.532, 0.35 and 0.266 $\mu\text{m}$  radiation," *Applied Physics B* **63**, 623-627 (1996).
37. S. R. Turns, *An Introduction to Combustion: Concepts and Application w/Software* (2005).
38. R. Friedman, *Principles of Fire Protection Chemistry and Physics* (1998).
39. M. McMillian, S. Richardson, and S. D. Woodruff, "Laser-Spark Ignition Testing in a Natural Gas-Fueled Single-Cylinder Engine," (U.S.DOE, NETL, 2004).
40. J. H. Lee, and Knystautas, R., "Laser spark ignition of chemically reactive gases," *AIAA Journal*, **7**(2)(1969).
41. J. X. Ma, D. R. Alexander, and D. E. Poluain, "Laser spark ignition and combustion characteristics of methane-air mixtures.," *Combustion and Flame* **112**, 492-506 (1998).
42. A. E. Siegman, "Output beam propagation and beam quality from a multimode stable cavity laser," *IEEE J. Quantum Electron* **29**, 1212-1217 (1993).
43. A. P. Yalin, M. Defoort, S. Joshi, D. B. Olsen, B. Willson, Y. Matsuura, and M. Miyagi, "Laser ignition of natural gas engines using fiber delivery," in *ASME ICE Division 2005 Fall Technical Conference*, (Ottawa, 2005).
44. L. Stenike, E. Linder, H. Maurer, K. Muller, and F. Rieger, "Optical Engine knock sensing system," (1983).
45. T. X. Phuoc, "Laser-induced spark for simultaneous ignition and fuel-to-air ratio measurements," *Optics and Lasers in Engineering*, **44**, 520-534 (2006).

## Chapter 2

---

### Time Resolved Spectroscopic Study of Laser Sparks in Air at High Pressures

A fundamental 1064 nm neodymium yttrium aluminum garnet (Nd:YAG) laser was used to create sparks in air at pressures ranging from 0.85 to 48.3 bar. A detailed spectroscopic investigation on the effects of ambient pressures on spark (plasma) temperatures and electron number densities was conducted for temporal windows between 0.1  $\mu\text{s}$  and 5  $\mu\text{s}$  from the plasma onset. Neutral atomic oxygen lines at 715 nm and 777 nm were used for temperature measurement through a Boltzmann analysis. Electron number density was measured by using Stark broadening of atomic hydrogen ( $H_{\alpha}$ ) lines at 656 nm. Full Width Half Maximums (FWHM) of  $H_{\alpha}$  lines were measured and correlated with tabulated data of FWHM and electron number density at different temperatures. At later stages ( $\sim 1\mu\text{s}$ ) of spark evolution, spark temperatures became comparable at all pressures, whereas electron number densities increased initially with increased ambient gas pressures but became comparable only at pressures greater than  $\sim 20$  bar.

## 2.1 Introduction

Laser sparks have been used extensively for applications such as laser induced breakdown spectroscopy (LIBS), laser-plasma X-ray sources (LPXS), gamma ray-radiography etc<sup>1</sup>. Laser spark is also viewed as a potential ignition source for high pressure combustion applications such as in gas engines<sup>2,3</sup>. Experiments have shown that laser ignition in turbocharged natural gas engines has the potential to extend the lean limit and increase peak pressures leading to reduced nitrous oxides (NO<sub>x</sub>) emissions and high operating efficiencies<sup>4,5</sup>.

Unlike electrical breakdown in conventional spark plugs, laser sparks are produced by focusing a megawatt peak power pulsed laser beam in a gaseous medium. As was discussed in Chapter 1, typical breakdown intensities in atmospheric pressure gases and nanosecond laser beams are  $\sim 300 \text{ GW/cm}^2$ <sup>6-9</sup>. Resulting laser sparks have initial peak temperatures ( $\sim 100000 \text{ K}$ ) and pressures ( $>1000 \text{ bar}$ )<sup>10,11</sup>. Furthermore, laser sparking becomes easier at higher pressures since the breakdown threshold intensity decreases<sup>10,12,13</sup>. Laser ignition in gas engines also provides an opportunity for performing LIBS for in-cylinder equivalence ratio measurements. Since laser ignition and LIBS measurement inside the engine cylinder takes place at elevated pressures, detailed spectroscopic study of laser sparks at high pressure conditions to measure spark temperature and electron number density is required. This study is also useful for modeling of subsequent ignition and combustion<sup>1</sup>.

Most of the published works have focused on understanding the effects of high pressures on breakdown threshold intensity<sup>10,12,13</sup> or they have characterized laser sparks

at only atmospheric and sub-atmospheric pressure conditions<sup>10,14,15</sup>. Yalcin et al. investigated the effect of ambient conditions on laser spark in air at atmospheric pressure<sup>15</sup>. It was showed that changing the ambient gas, the laser energy, particulate levels, and humidity levels produced little variation in the temperature and electron density in the laser spark. However, the effects of changing the ambient air pressure on laser air spark characteristics were not investigated.

Glumac et al. investigated the effects of sub-atmospheric pressure (0.1 bar to 1 bar) on temperature and electron density of laser sparks formed in air<sup>14</sup>. For the possible exception of the lowest pressure (0.1 bar) and for a fixed input laser energy level, no difference in temperature from 0.5  $\mu$ s to 1  $\mu$ s over the sub-atmospheric pressure ranges was observed. But a strong dependence of pressure on electron number density was found. The electron number density of the plasma decreased linearly with decreasing ambient sub-atmospheric pressure. The reported temperature and electron density at atmospheric pressure in Glumac et al.'s study were consistent with Yalcin et al.'s results.

Time resolved spectroscopic measurements of laser produced hydrogen plasma were conducted by Litvak et al. for pressures ranging from 1 bar to 71 bar<sup>16</sup>. The plasma was produced by a 0.5 – 5 megawatt peak power ruby laser at 694.3 nanometer (nm) with a pulse width of 18 – 36 ns. For plasma formation at atmospheric pressure, plasma temperature was reported to be 150,000 K at 0.1  $\mu$ s which dropped to 35,000 K at 1  $\mu$ s while electron density dropped from  $2.8 \times 10^{18} \text{ cm}^{-3}$  at 0.1  $\mu$ s to  $0.35 \times 10^{18} \text{ cm}^{-3}$  at 1  $\mu$ s. However, at elevated pressures, for example at 28.6 bar, initial plasma temperature was still measured to be 150,000 K at 0.1  $\mu$ s which dropped to 70,000 K at 1  $\mu$ s. Similarly, electron density dropped from  $8.5 \times 10^{18} \text{ cm}^{-3}$  at 0.1  $\mu$ s to  $1 \times 10^{18} \text{ cm}^{-3}$  at 1  $\mu$ s. Although

the reported electron density is comparable with the results from two reported experiments by Yalcin et al. and Glumac et al., the measured plasma temperature in Litvak et al.'s work (especially at 1  $\mu$ s gate delay) was considerably higher. This difference in temperature might also be due to the different focal lengths of the focusing lens and the ambient gas used in the experiments. Yalcin et al. and Glumac et al. used 100 mm long focal length lens to produce laser sparks in air while Litvak et al. used a 25 mm long focal length lens to make laser sparks in hydrogen. The measured plasma temperature and electron density in Litvak et al.'s experiment was used to determine the temperature decay due to radiation, expansion cooling and electron loss because of collisional- radiative recombination. It was found that the temperature leveled off at a value that was sensitive to the balance between cooling effects and the heating of the electron gas during electron recombination (i.e, plasma heating by the energy recovered from recombination of electrons with ions).

This short survey of the published work show that most of the work on characterizing plasmas was done with 1064 nm radiation in atmospheric air conditions. The only high pressure work was done by Litvak et al. with a ruby laser at 694.3 nm in hydrogen atmosphere. Since laser spark formation depends on the nature of the gas, wavelength of the laser radiation and pressures, one may expect different results from those reported in the published literature for laser sparks created in air with a 1064 nm laser beam. To our knowledge, there have been no published works on quantifying the effects of high pressures on the temporal evolution of temperature and electron density of a laser spark produced by focusing 1064 nm Nd:YAG lasers with Q-switched nanosecond

(5–10 ns) pulses in air. In this work we present the results from spectroscopic study of these laser sparks in pressures ranging from 0.85 – 48.3 bar.

The layout of the chapter is as follows. In section 2.2, we discuss the experimental setup to perform the spectroscopic study of laser sparks. In section 2.3, we first discuss the laser energy absorption by the laser sparks at different elevated pressures. We then present the temperature measurement procedures and measured plasma temperature at various delay settings. The plasma electron number density measurement procedures and results are then presented. In section 2.4, we present conclusions and discuss the possible effect of pressure on LIBS measurement at high pressures.

## 2.2 Experimental Setup

Figure 2.1 illustrates the experimental setup for laser spark characterization at high pressures. A 1064 nm Q-switched Nd:YAG laser from Big Sky was used to create laser sparks at 10 Hz. The pulse duration of the laser was 8 ns and the input laser energy level was kept constant at ~26 mJ. As shown in Fig. 2.1, the laser beam was turned ninety degrees into a high pressure optical cell by a coated mirror which reflects 1064 nm light while transmitting other wavelengths. The high pressure optical cell was constructed from aluminum and had two optical ports (in line with the laser beam) and two gas ports (perpendicular to the laser beam). High pressure air with 1% hydrogen (by volume) was fed into the optical cell through the inlet port, labeled 10. The hydrogen was added in order to get good signals for  $H_{\alpha}$  lines at high pressures for electron density measurements. A tiny leak was maintained at the exit port to maintain a continuous flow of gas inside the optical cell.

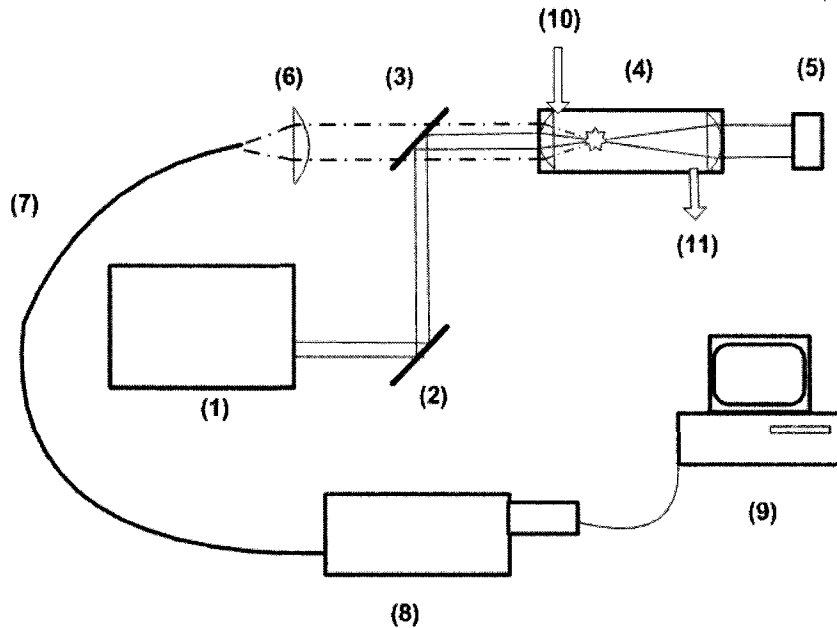


Figure 2.1: Experimental setup for laser spark diagnostics at ambient high pressures.(1) 1064nm Nd:YAG laser , (2) Mirror , (3) Mirror , (4) High Pressure Optical Cell , (5) Energy meter , (6) Focusing lens , (7) Optical Fiber , (8) Spectrometer/ICCD , (9) Data Acquisition System (WINSPEC), (10) High Pressure Air Inlet, (11) High Pressure Air Outlet. Note: The solid line indicates the laser beam. The dotted lines indicate the light emission from the laser spark.

The pressure inside the optical cell was constantly monitored by a pressure gauge. A set of six pressures (0.85 bar, 3.5 bar, 6.9 bar, 20.7 bar, 34.5 bar and 48.3 bar) was tested. Note that 0.85 bar is used to denote the atmospheric pressure in Fort Collins. The laser beam was focused inside the high pressure optical cell by a 25 mm focal length plano-convex lens fixed at the first optical port of the cell. The laser beam that was not absorbed by the spark was collected through the second lens fixed at the second optical port (the right optical port of the high pressure cell) and was measured by an energy meter. The light from the laser spark was collected through the first focusing lens (at the left optical port) in the optical cell and the coated mirror and focused by a 35 mm focal

length lens into a 1 mm diameter fiber optic. This fiber optic was connected to a 0.3 m Roper Scientific ACTON series Spectra Pro - 2300i spectrometer attached to an Intensified Charged Couple Device (ICCD) camera. A 300 grooves/mm grating and a 1200 grooves/mm grating (both blazed at 750 nm) were alternatively used for temperature and electron number density measurement respectively. The instrumental FWHM of the system (spectrometer/ICCD camera) was measured with a 543.5 nm helium-neon laser. FWHMs of 0.6 nm and 0.1 nm were obtained for the system with 300 grooves/mm and 1200 grooves/mm gratings respectively. In order to acquire spectra at different delays from the plasma onset, the ICCD camera was synchronized relative to the laser pulse using a Q-switch synchronization signal. The gating of the ICCD was controlled to capture spectra at different delays from plasma onset.

Two sets of experiments were conducted. The first set of experiments involved collecting spectra with neutral oxygen (O) atomic lines at 715 nm and 777 nm lines for temperature measurement. Relevant spectroscopic details of O atomic lines at 715 nm and 777 nm as well as  $H_{\alpha}$  at 656 nm are provided in Table 2.1. The second measurement involved collecting spectra with atomic hydrogen lines ( $H_{\alpha}$ ) at 656 nm for electron number density measurement. For each pressure, a total of nine spectra were collected for delay settings from 0.1  $\mu$ s to 5  $\mu$ s from the laser spark onset. A gate width of 100 ns was used for all delays less than 1  $\mu$ s (except at pressures higher than 20.7 bar where a gate width of 200 ns was used for gate delays of 0.5 and 0.75  $\mu$ s). For gate delays of 1, 2 and 3  $\mu$ s, a 1  $\mu$ s gate width window was used. A 5  $\mu$ s gate width was used for gate delay of 5  $\mu$ s to compensate for reduction in light intensity at longer delays. A set of 100 spectra was collected for each delay setting and averaged. A relative intensity calibration was

performed for the system with a LS1-CAL tungsten calibration lamp from Ocean Optics. All the collected spectra were then adjusted with the relative intensity calibration values to remove any wavelength dependent spectral response.

Table 2.1: Relevant atomic data for the observed spectral lines<sup>23</sup>.

Atomic lines	Wavelength (nm)	$E_i$ (cm <sup>-1</sup> ) - $E_k$ (cm <sup>-1</sup> )	$A_{ki}$ (s <sup>-1</sup> )
H $_{\alpha}$	656.28	82,259.28 – 97,492.35	6.46e+07
O <sub>715</sub>	715.67	102,662.02 – 116,631.09	5.05e+07
O <sub>777</sub>	777.19	73,768.20 – 86,631.45	3.69e+07
O <sub>777</sub>	777.41	73,768.20 – 86,627.77	3.69e+07
O <sub>777</sub>	777.53	73,768.20 – 86,628.75	3.69e+07
N <sub>742</sub>	742.36	83,284.07 – 96,750.84	5.95e+06
N <sub>744</sub>	744.22	83,317.83 – 96,750.84	1.24e+07
N <sub>746</sub>	746.83	83,364.62 – 96,750.84	1.93e+07

*Note:  $i$  and  $k$  represent lower and upper levels of the atomic transitions respectively.  $E$  represents energy level of the atomic transition and  $A$  represents the transition probability.*

## 2.3 Results and Discussions

Figure 2.2 illustrates the percentage of laser energy absorbed by laser sparks at various pressures. The sparking rate was observed to be 100% at all pressure conditions.

For these experiments, input laser energy level was kept constant at 26 mJ. Estimation of focal spot diameter spark location resulted in the breakdown intensity of  $\geq 300 \text{ GW/cm}^2$  at atmospheric pressure which is consistent with published results. As can be seen from the figure, the energy absorption increases rapidly from  $\sim 65\%$  at atmospheric pressure to  $\sim 85\%$  at pressures of 6.9 bar. Loss by scattering, at least for initial pressures, was assumed to be small.

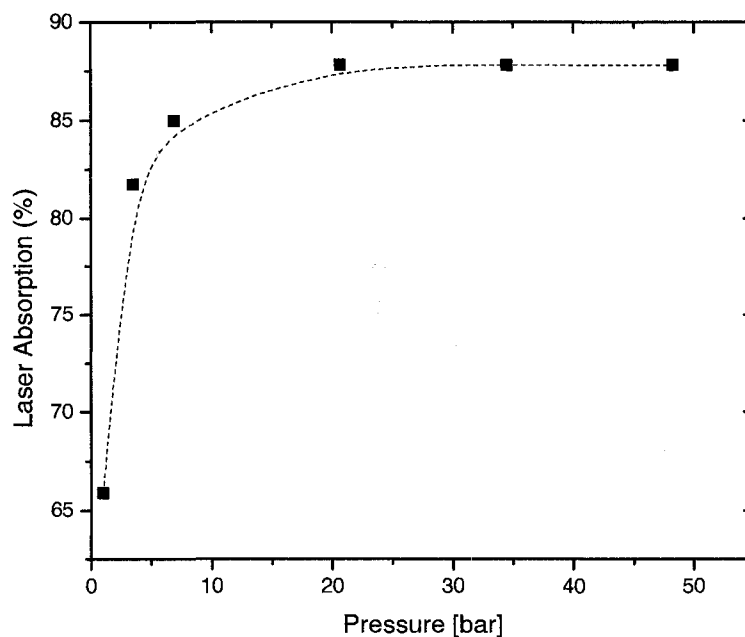


Figure 2.2: Percentage of laser energy absorbed by laser sparks at different ambient pressures.

---

Note that the observed increase in energy absorption is consistent with electron inverse bremsstrahlung absorption of laser energy by the spark (as was discussed earlier in Chapter 1). In this absorption process, plasma absorption coefficient increases

with the square of electron density in the plasma (and hence the square of ambient pressure)<sup>11,16-18</sup>. Furthermore, the breakdown threshold intensity decreases and less energy is required for the breakdown. However, as higher pressures are reached, for example from ~20.7 bar to ~48.3 bar, the percentage of laser energy absorbed by the plasma was observed to be constant at 88%. We conjecture that this phenomenon is due to the plasma becoming opaque to the laser pulse at some initial times of the laser pulse. At constant input laser energy and high pressures, the ionizing electron avalanche (discussed in Section 1.2) might result in an electron density flux higher than a critical amount needed for the plasma to absorb the laser energy. At these high electron density flux (at early times of the laser pulse) the plasma frequency becomes higher than the laser frequency<sup>11</sup>. This results in the plasma becoming opaque to the laser pulse and hence the plasma reflects a portion of the laser beam for some initial time of the laser pulse duration<sup>19</sup>. Indeed in a separate experiment, when spark emission spectra were collected with an Ocean Optics HR4000 spectrometer (with a spectral range from 400 nm – 1100 nm), the 1064 nm light was also detected in the laser spark emission spectra. The detected 1064 nm light was the back reflected light from the focusing lens. However, the intensity of this 1064 nm light increased with increasing pressures for a constant input laser energy level. A similar conjecture was made by researchers who observed saturation effects in laser plasma X-ray emissions<sup>19</sup>. They attributed this saturation effect to the opacity of the plasma to the laser beam at some initial time duration.

### 2.3.1 Spark Temperature Measurements

For spark temperature measurements, a 300 grooves/mm grating was used to obtain spectra between 700 nm and 780 nm. Figure 2.3a shows an example of emission spectra at atmospheric pressure for various delays. For comparison purpose, emission spectra of the laser spark at 34.5 bar are shown in Fig 2.3b.

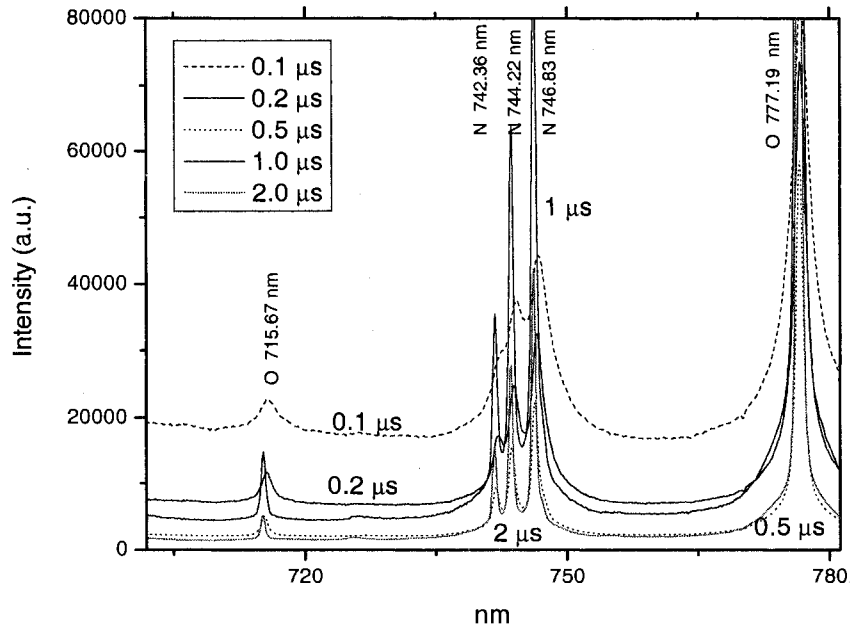


Figure 2.3a: Emission spectra from laser spark at 0.85 bar.

---

In fig 2.3a (~0.85 bar), one can observe a high continuum emission (~ 18,000 counts) at 0.1  $\mu$ s. The continuum emission from the plasma is a superposition of several continuum spectra due to free-free radiation, recombination or free-bound radiation, negative ion emission, and pseudo-continuum of strongly broadened lines<sup>1, 20</sup>. The neutral

O atomic lines at 715 nm and 777 nm are clearly visible. The neutral nitrogen atomic lines (N) at 744 and 746 nm are also visible and resolved whereas, the peak of N atomic line at 742 nm is less resolved. At a delay setting of 0.2  $\mu\text{s}$ , the overall baseline continuum emission has decreased to  $\sim 7000$  counts and the three N atomic lines at 742 nm, 744 nm and 746 nm are well resolved (though overlapping). As the delay increases to 2  $\mu\text{s}$ , the continuum decreases ( $\sim 1550$  counts) and the neutral atomic lines of N and O become narrower and more intense.

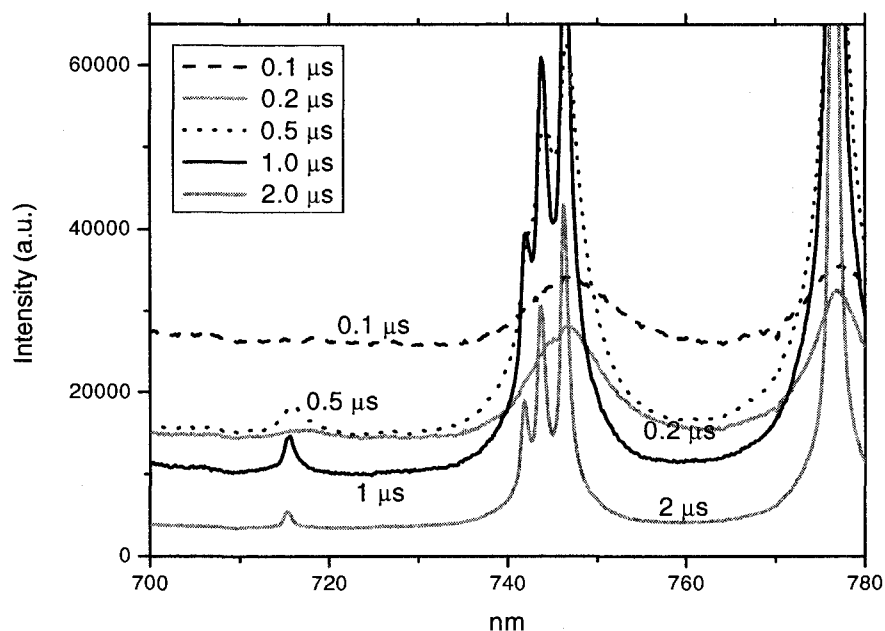


Figure 2.3b: Emission spectra from laser spark at 34.5 bar.

In fig 2.3b ( $\sim 34.5$  bar), one observes a higher continuum emission ( $\sim 28,000$  counts) at 0.1  $\mu\text{s}$  gate delay compared to the emission at atmospheric pressure. The neutral O atomic line at 715 nm is not visible and none of the three N atomic lines at 742,

744 and 746 nm are resolved. At 777 nm, the O atomic line is visible but is broader and less intense than the corresponding O atomic line at 1 bar due to collisional quenching which becomes pronounced at higher pressures<sup>21</sup>. At a gate delay of 0.2  $\mu$ s, the continuum emission has decreased to 15000 counts (still higher compared to atmospheric condition). The O atomic line appears at 715 nm and only the N line at 746 nm is resolved. At a delay setting of 2  $\mu$ s, the baseline continuum emission has decreased to ~ 3500 counts (higher than the corresponding baseline continuum emission in atmospheric pressure) and the atomic lines of O and N have become relatively narrow and more intense. Overall, one observes that as the ambient pressure is increased, the continuum emission increases and the atomic lines become broader and less intense. At higher pressures, the O atomic line at 715 nm appears relatively late and hence, temperature measurements become possible only for later times of plasma evolution.

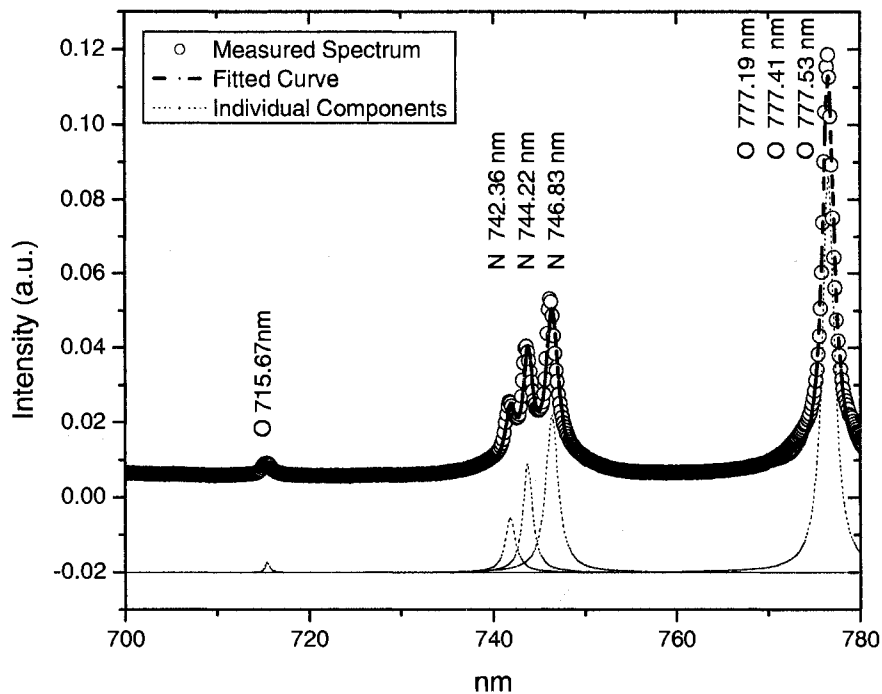


Figure 2.4: Example of a measured spectrum at 34.5 bar and 1 $\mu$ s gate delay and fit in 700 -780 nm region including contributions from individual peaks.

The spectra from various pressures and delay settings were analyzed for line ratios of neutral atomic O at 715 nm and 777 nm. A linear baseline subtraction was performed to remove the contribution of continuum emission and the resulting atomic lines were fitted with Voigt profiles. Figure 2.4 illustrates an averaged spectrum from plasma emission at 34.5 bar at a gate delay of 1  $\mu$ s. The figure shows the measured spectrum along with the fitted curve and the individual components (with an offset for visual clarity). In the figure, the atomic line of O at 715.67 nm is clearly identifiable. The N atomic lines at 742.36 nm, 744.22 nm and 746.83 nm are also well resolved but partially overlap. However, due to the instrumental FWHM of 0.6 nm, the triplet O

atomic lines at 777.19 nm, 777.41 nm and 777.53 nm are not resolved and are observed as a single feature at ~777 nm.

During this study, the plasmas at all pressures and times were assumed to be optically thin. Although no experimental investigation was performed to check the optical thickness of the plasmas, it should be noted that the effect of optical thickness is strong only for early times in plasma evolution (earlier than 150 ns)<sup>14</sup>. Our measurements are comparatively at later times and hence the effects of optical depth on measurements should be small. Furthermore, when strong plasma optical depth effects exist, a significant departure in the shapes of the atomic lines can be observed<sup>22</sup>. No departure in the atomic line shapes was observed during this work.

The plasma was also assumed to be under local thermal equilibrium (LTE). This assumption is justified since the plasma electron density and temperature are often high enough so that fast collision rate dominates the slower radiative processes to keep the plasma under LTE<sup>15</sup>.

Under these conditions, the temperature of plasma can be obtained by a Boltzmann analysis of atomic lines of O at 715 nm and 777 nm, as shown in equation 1.

$$T = \frac{E' - E}{k \ln \left( \frac{I' g' A' \nu'}{I g A \nu} \right)} \quad (1)$$

In Equation.1, T and I denote plasma temperature and line intensities (areas) respectively, A is the coefficient of the transition, E is the upper -level energy, g is the statistical weight of the upper state of the line, k is the Boltzmann's constant and  $\nu$  is the frequency. The parameters for O lines are given in Table 2.1. The prime symbol indicates

the corresponding quantities for O atomic line at 715 nm. These O atomic lines have a large separation of their upper level energies and are relatively intense. Hence, they were chosen for plasma temperature measurements. The corresponding intensity (I) is the line intensity (area) obtained from fitting the lines with Voigt profile. Since the wavelength resolution of the detection system was low, the oxygen triplet was treated as a single feature. Assuming similar frequencies and upper level energies for the triplet O lines, the statistical weight of the upper state (g) for O at 777 nm in equation 1 becomes just the sum of statistical weights of the three lines of the O triplet at 777.19 nm, 777.41 nm and 777.53 nm.

A temperature error measurement procedure was followed as discussed in reference [1]. The relative uncertainties in temperature measurement can be expressed as:

$$\left| \frac{\Delta T}{T} \right| = \frac{kT}{E' - E} \left| \frac{\Delta X}{X} \right| \quad (2)$$

where,

$$\left| \frac{\Delta X}{X} \right| \cong \frac{\Delta I}{I} + \frac{\Delta I'}{I'} + \frac{\Delta A}{A} + \frac{\Delta A'}{A'} \quad (3)$$

The relative uncertainty in temperature is denoted by  $\frac{\Delta T}{T}$  in eqn. 2.  $\frac{\Delta X}{X}$  represents total relative uncertainty from Einstein coefficients, contribution from calibration procedure and baseline continuum fitting. Relative uncertainties in Einstein coefficient are estimated at 3% and 10% for O atomic lines at 715 nm and 777 nm<sup>23</sup>. The contribution from calibration procedures and baseline continuum fitting is expressed as the first two terms in the right hand side of eqn.3 and is conservatively estimated at 10%.

Total uncertainty is thus 23%. The difference in upper-level energies in eqn. 2 is about  $5.96 \times 10^{-19}$  J. Hence, relative uncertainty in temperature is  $5.3 \times 10^{-6}$  T.

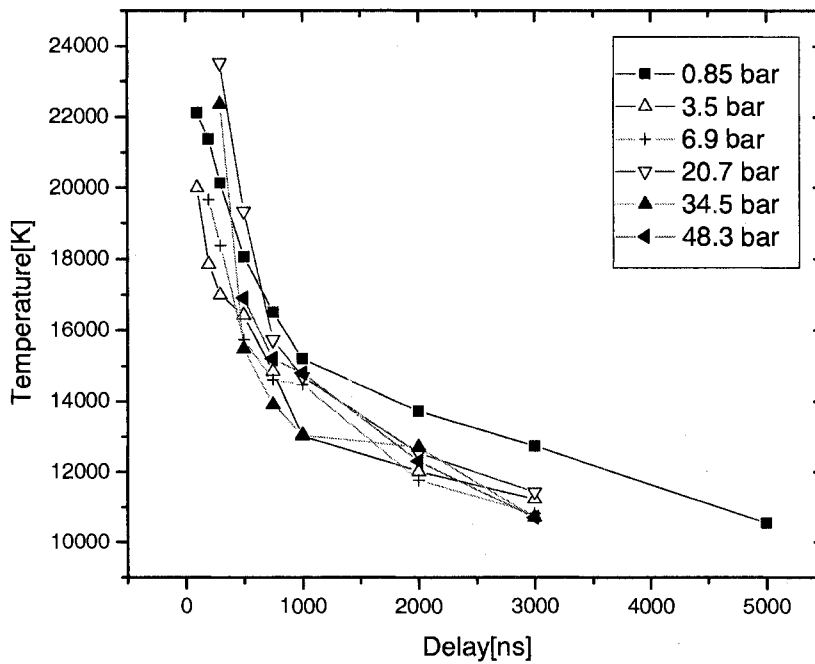


Figure 2.5: Plasma temperature vs. delay for six pressures at incident laser pulse energy of 26 mJ.

Figure 2.5 shows the time dependence of plasma temperature for six different initial ambient pressures. Temperature measurement over the full range between 0.1  $\mu$ s and 5  $\mu$ s gate delay was possible only for plasma at atmospheric condition ( $\sim$ 0.85bar). For higher pressures, the lack of O line at 715 nm for a gate delay of 5  $\mu$ s makes it

difficult to obtain temperature for that time delay. As pressure is increased, O line at 715 nm also starts to appear increasingly later during the early plasma evolution. Hence, for pressures greater than 6.9 bar, plasma temperature measurement became possible only after 0.3  $\mu$ s.

In Fig. 2.5, one can observe the plasma temperature decaying faster during initial plasma evolution ( $<1 \mu$ s), as compared to after 1 $\mu$ s where the decay is slower. For the laser spark at atmospheric pressure one can observe a rapid temperature drop from an initial value of  $\sim 22,000$  K (at 0.1 $\mu$ s) to  $\sim 15,200$  K (at 1  $\mu$ s). The plasma temperature then drops more slowly from  $\sim 13,000$  K at 3  $\mu$ s to  $\sim 11,000$  K at 5  $\mu$ s. Extrapolating the measured temperatures in Fig 2.5 to smaller times may yield comparably higher temperatures. Bradley et al. have estimated peak spark temperatures to be higher than 100,000 K for 1064 nm spark formation at atmospheric pressures<sup>11</sup>.

Also from the figure, one can observe that the temperature drop at early times is faster for higher pressures. However at later times, for example at 3  $\mu$ s, plasma temperature for 34.5 and 20.7 bar is  $\sim 11000$  K. Hence, despite initial higher temperatures and different temperature decay rates, the temperature at later times of the plasma evolution in high pressure conditions become comparable (albeit being lower than at atmospheric condition). Note that these measured temperatures are much lower than the temperature obtained by Litvak et al. in their experiments in hydrogen plasmas (discussed earlier in Section 2.1).

The rapid decrease in temperature during early plasma life times (initial stage of expansion) of the plasma are due to the adiabatic expansion of the plasma, energy losses due to line and continuum radiation (from bremsstrahlung and blackbody radiation when

LTE is assumed) and heat conduction<sup>16</sup>. During the initial adiabatic expansion, thermal energy is converted into kinetic energy and the plasma cools rapidly. Furthermore, when radiation losses are assumed to be mainly due to bremsstrahlung<sup>24</sup> and blackbody radiation, the losses are proportional to  $\sqrt{T}$  and  $T^4$  respectively. This suggests larger losses for higher pressure conditions and hence larger rate of temperature drop. However, at later times of the plasma evolution, the cooling rate decreases as a result of competing effects of slowing of adiabatic plasma expansion and the additional energy released due to recombination of electrons with ions (recombination heating)<sup>10,16</sup>. As suggested by Litvak, the temperature at later stage of plasma expansion is determined by a sensitive balance of cooling effects and recombination heating<sup>16</sup>, the calculations of which are out of scope for this work.

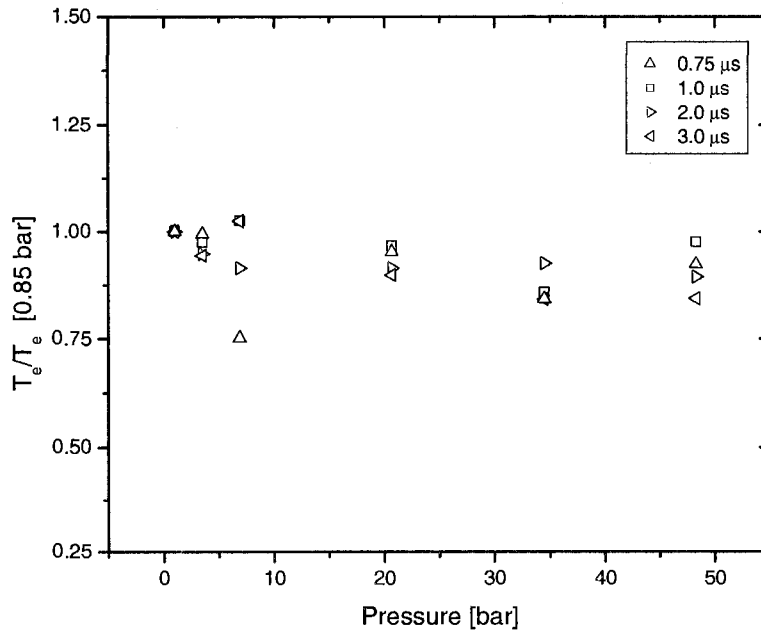


Figure 2.6: Ratio of plasma temperature at various delays and pressures.

Figure 2.6 shows the plasma temperature ratios at various delays (later times of plasma evolution) versus different pressures. Temperatures are normalized with respect to temperatures at 0.85 bar. No significant dependence of plasma temperature (especially for later times) on initial ambient pressure can be observed.

### 2.3.2 Spark Electron Number Density Measurements

Electron density of plasma can be inferred from the widths of Stark broadened hydrogen Balmer Series line,  $H_{\alpha}$  at 656 nm<sup>10,25-27</sup>, although other atomic and ionic lines are also possible. The main broadening mechanism of atomic lines are Gaussian (Doppler and instrumental broadening) and the pressure broadening (natural, van der Waals, resonance broadening and Stark broadening). Stark broadening results from Coulomb interactions between the radiator (hydrogen atoms, in this case) and the charged particles (electrons and ions) present in the plasma. Theories for hydrogen and hydrogenic ions are well established<sup>28</sup>. Furthermore, they exhibit a linear Stark effect resulting in larger FWHMs. Other atoms and ions exhibit a quadratic Stark effect, and so have a much smaller Stark broadened linewidths<sup>15,25</sup>.

In this experiment, laser spark emission spectra were obtained with a 1200 grooves/mm grating between a spectral window of 644 nm and 674 nm. The acquired spectra were adjusted with a linear baseline correction. Stark broadened  $H_{\alpha}$  line at 656 nm and neighboring atomic lines of singly ionized N (II) lines at 648 nm, 661 nm and 666 nm were fitted with Lorentzian profiles, characteristic of Stark broadening. This is justified since for  $H_{\alpha}$  atomic line the Gaussian contribution, natural broadening, van der

walls and resonance broadening are much smaller than Stark broadening<sup>29,30</sup>. The measured widths of the stark broadened  $H_{\alpha}$  line was used to determine the electron number density by interpolating from the tabulated data using calculated plasma temperatures<sup>28</sup>.

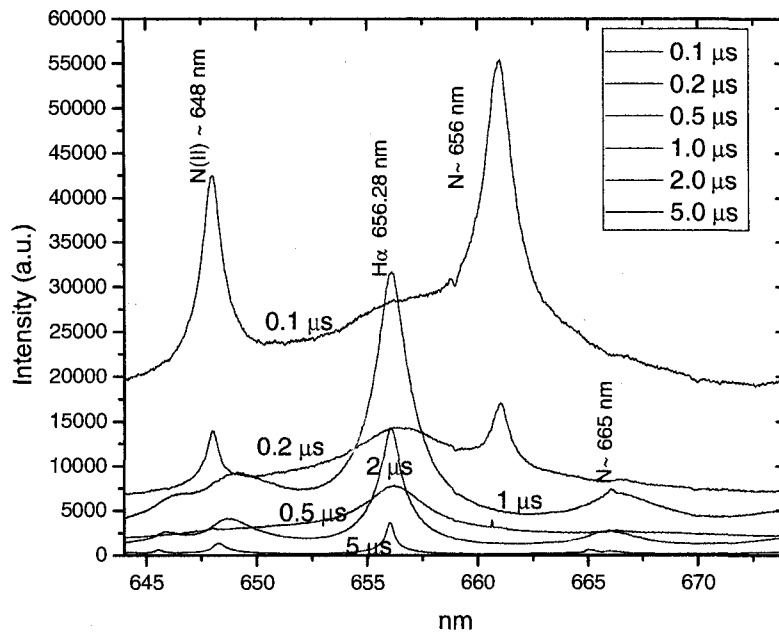


Figure 2.7a: Emission spectra from laser sparks at 0.85 bar.

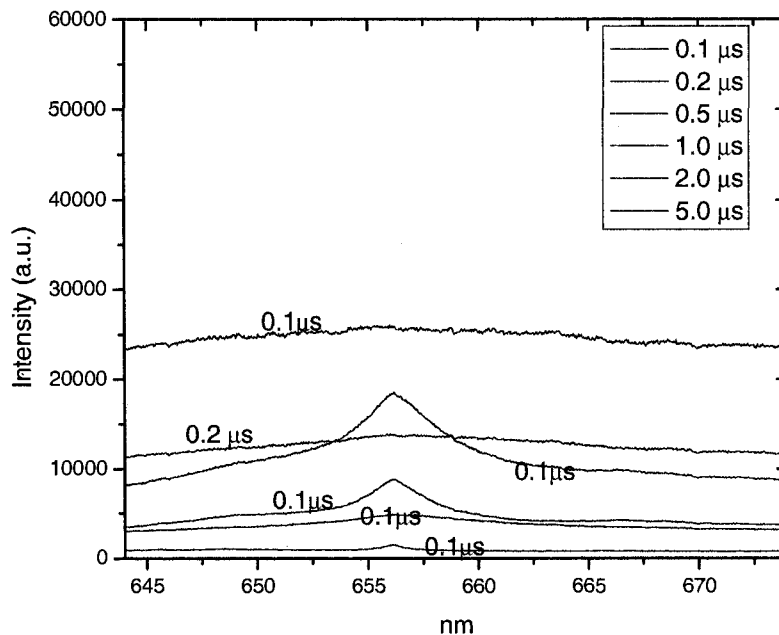


Figure 2.7b: Emission spectra from laser sparks at 34.5 bar.

Figures 2.7 a) and b) show examples of spectra obtained at different delays for 0.85 bar and 34.5 bar pressure conditions respectively. In Fig. 2.7a, strong and intense singly ionized N (II) lines at 648 nm and 661 nm can already be seen at 0.1  $\mu\text{s}$  gate delay. The  $H_{\alpha}$  atomic line at 656 nm is barely visible and is strongly broadened. As the plasma evolves, the  $H_{\alpha}$  atomic line becomes more pronounced and narrow and the N (II) line at 661 nm disappears. The maximum signal for  $H_{\alpha}$  is obtained at a gate delay of 1  $\mu\text{s}$ . Broad peaks consisting of overlapping atomic and ionic nitrogen lines (between 646 nm and 650 nm; 665 nm and 672 nm) can also be seen at 1  $\mu\text{s}$ . One can also observe that as the delay increases, the stark broadened  $H_{\alpha}$  atomic line becomes narrower suggesting decreasing electron density. The  $H_{\alpha}$  atomic line can still be observed at 5  $\mu\text{s}$  from the onset of the

plasma. At 34.5 bar in Fig. 2.7b, for 0.1  $\mu\text{s}$  delay one can observe just a broad continuum with no  $H_{\alpha}$  or N (II) lines. In fact, the N (II) line at 661 nm and 646 – 650 nm are not resolved for any of the delays. It should be noted from Fig. 2.7a) and b), that the  $H_{\alpha}$  atomic lines at all delays in high pressure conditions are much broader and less intense compared to  $H_{\alpha}$  atomic lines at atmospheric pressure condition.

Figure 2.8 illustrates a spectrum from laser spark emission at  $\sim 34.5$  bar and a gate delay of 1  $\mu\text{s}$ . The figure shows a measured spectrum along with the fitted curve and individual components. The higher pressure cases proved more difficult for peak fitting because of lower peak to baseline continuum ratio and hidden N (II) lines, especially during earlier plasma life times.

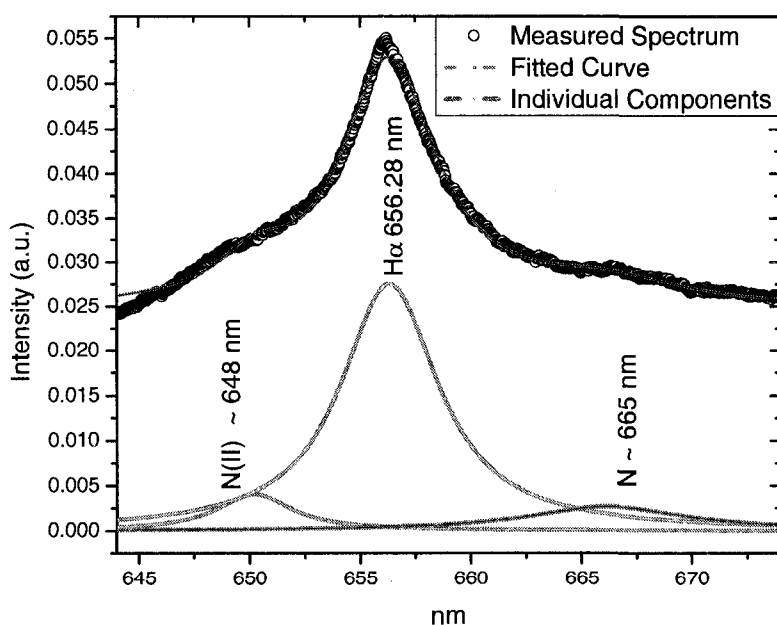


Figure 2.8: Example of a measured spectrum at 34.5 bar and 1  $\mu\text{s}$  gate delay and fit in 644 - 674 nm region including contributions from the individual peaks.

In this work, the electron density measurement was based on Oks' data on theoretically derived values of electron density for different Stark widths of  $H_{\alpha}$  atomic line at various temperatures<sup>28</sup>. Oks' data reports better accuracy than Griem's theoretical results because of additional contributions of coupling phenomena and ion dynamics to Stark broadening<sup>31</sup>. The theoretical results of Griem indicate that one can expect electron density accuracies of 20%<sup>15,20</sup>. In this work, we consider errors in electron density measurement as a result of approximately 20% error on FWHM of  $H_{\alpha}$  line measurements for time delays less than 0.3  $\mu$ s and 10% error on FWHM measurement for time delays after 0.3  $\mu$ s. These errors are due to calibration, baseline fitting and peak fitting. This error estimation procedure results in an overall average of 15% - 25% errors in electron density measurements. Large errors of upto 50% is assumed for measured electron density, when this error estimation procedure led to values of FWHMs that exceeded the tabulated values (only at very early times of spark evolution). The dependence of electron density on temperature was also investigated but was found that even 30% change in plasma temperature didn't change the electron density significantly (<1%). This is consistent with past research that showed that the Stark broadening width is mostly a function of free electron concentration and is a weak function of temperature<sup>1,30</sup>.

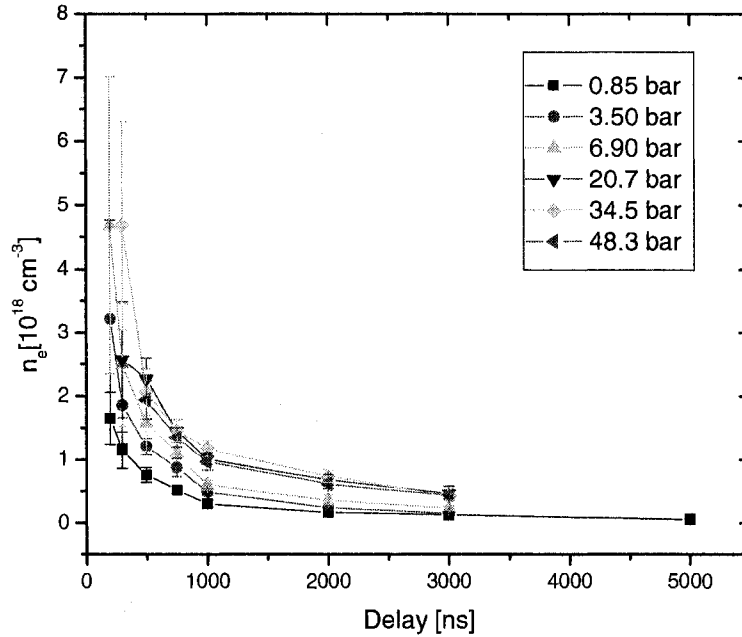


Figure 2.9: Temporal evolution of electron number density ( $n_e$ ) for different pressures.

In Fig 2.9 measured electron density ( $n_e$ ) versus time from initial breakdown is plotted for plasmas formed in pressures from 0.85 bar to 48.3 bar. Plasma electron density could be measured as early as 0.2  $\mu\text{s}$  only for atmospheric pressure condition. For higher pressures, electron densities are plotted only for delay times for which the plasma temperature could be measured. Plasma electron densities are observed to increase progressively as pressure is increased from atmospheric condition. In order to highlight the temporal change in electron density more clearly, temporal evolution of plasma electron densities for 0.85 bar, 20.7 bar and  $\sim$ 34.5 bar condition are plotted in Fig 2.10.

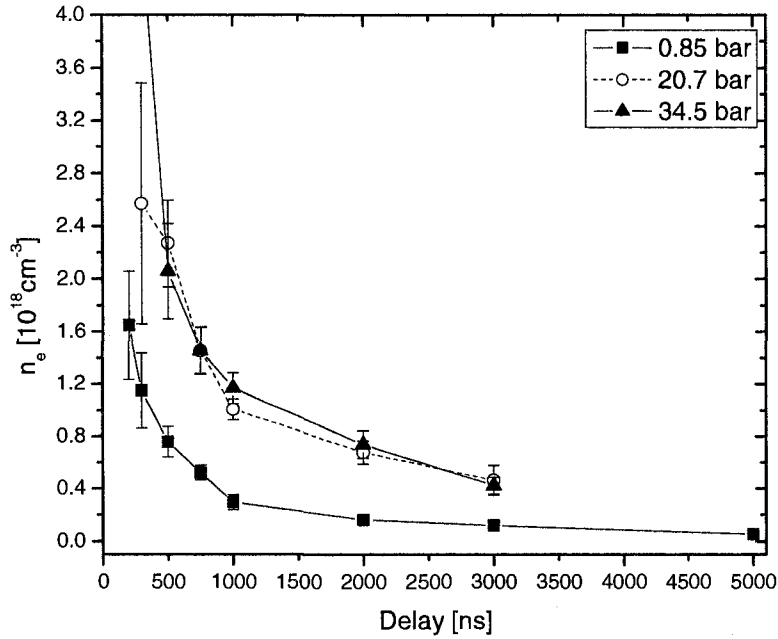


Figure 2.10: Temporal evolution of electron number density ( $n_e$ ) for 0.85 bar, 20.7 bar and 34.5 bar. ( $n_e$  of  $4.67 \times 10^{18} \text{ cm}^{-3}$  is observed at a delay of  $0.3 \mu\text{s}$  at 34.5 bar and is not shown in order to clearly highlight the temporal change in electron density for the three pressure conditions).

In atmospheric pressure condition (0.5 bar), one observes a rapid drop in electron density from an initial value of  $1.6 \times 10^{18} \text{ cm}^{-3}$  (at  $0.2 \mu\text{s}$ ) to  $0.3 \times 10^{18} \text{ cm}^{-3}$  (at  $1 \mu\text{s}$ ) after which  $n_e$  then drops slowly to  $0.05 \times 10^{18} \text{ cm}^{-3}$  (at  $5 \mu\text{s}$ ). The measured values of  $n_e$  are in good agreement with those reported in past references. For  $\sim 20.7$  bar,  $n_e$  is  $2.57 \times 10^{18} \text{ cm}^{-3}$  (at  $0.3 \mu\text{s}$ ) which is twice compared to the value of  $n_e$  at atmospheric condition at this delay. A similar rapid drop in  $n_e$  for initial plasma times (less than  $1 \mu\text{s}$ ) is observed for 20.7 bar and 34.5 bar. The  $n_e$  is measured to be  $1 \times 10^{18} \text{ cm}^{-3}$  and  $1.16 \times 10^{18} \text{ cm}^{-3}$  at  $1 \mu\text{s}$  for 20.7 bar and 34.5 bar respectively but is still higher than at atmospheric condition

by a factor of approximately three. As the plasma evolves,  $n_e$  becomes comparable at all delays for these two pressures. At 3  $\mu\text{s}$ ,  $n_e$  is measured to be  $0.42 \times 10^{18} \text{ cm}^{-3}$  and  $0.46 \times 10^{18} \text{ cm}^{-3}$  for 20.7 bar and 34.5 bar which is approximately 3.6 times larger than the corresponding  $n_e$  at atmospheric condition.

It might be expected that the plasma size at higher pressures would be smaller in size. But at early times of plasma evolution ( $< 1 \mu\text{s}$ ) the pressure inside the plasma can be in the order of  $> 1000$  bars resulting in a minimal compressive effect of ambient pressures on initial plasma size. However, as the plasma cools down and expands (longer delays), the external ambient pressure has a greater effect on the plasma resulting in a smaller plasma volume and higher electron density. These results also indirectly suggest faster recombination rate of electrons (hence higher recombination heating rate) for plasmas formed at atmospheric pressure compared to higher pressures. This higher heating rate may be a reason for observed higher temperatures (at later times) in plasmas formed at atmospheric pressures compared to the plasmas formed at higher pressures. In general as pressure is increased, denser plasmas compared to plasmas at atmospheric pressure are observed which is consistent with results from Litvak's experiment.

With the measured spark electron density, the validity of existence of LTE can be checked by using a necessary (but not sufficient) condition for LTE <sup>32</sup>:

$$n_e \geq 1.6 \times 10^{12} T_e^{\frac{1}{2}} (\Delta E)^3 \text{ cm}^{-3} \quad (4)$$

Where,  $n_e$  is the minimum electron density for the plasma to exist in local thermodynamic equilibrium,  $T_e$  is the plasma temperature (in K), and  $\Delta E$  is the largest energy difference expected in the transitions (in eV). So, for example with plasma  $T_e$  of

22,000 K and conservative  $\Delta E$  of 10eV,  $n_e$  should exceed  $\sim 10^{17} \text{ cm}^{-3}$  for LTE to exist. The measured electron density for all pressures and delays are higher than the  $n_e$  found from eqn. (4). Hence, assumption of existence of LTE in the plasmas is considered to be valid.

## 2.4 Conclusions

A spectroscopic study of laser sparks produced by 1064 nm Nd:YAG laser in air at pressures ranging from 1 bar to  $\sim 48$  bar was conducted. For a fixed input laser energy, the percentage of laser energy was observed to increase rapidly from atmospheric pressure to some initial higher pressures and remained constant at increasingly higher pressures. This suggested that the laser plasmas might have become opaque to laser beam, at least for some initial durations. Plasma temperatures for various pressures were measured and they were found to be comparable ( $\sim 10,000\text{K}$ ) at later times for all high pressures. However, a strong dependence of pressure on electron number density was observed. Within measurement errors, the plasma electron densities at later times of plasma evolution were comparable for high pressures and were significantly higher ( $\sim 3.5$  times) than that at atmospheric condition. The observed higher electron number density might also be due to the compressive effects of the ambient high pressures on the plasma.

Overall, as the pressure was increased, a hot ( $\sim 10,000\text{K}$ ) and much denser plasma ( $n_e \sim 10^{18}$ ) was found to exist at 1  $\mu\text{s}$  delay from the initial breakdown. For LIBS in methane-air mixtures, the intensities of hydrogen and oxygen lines would depend on the plasma temperature and electron density, since higher temperature would suggest higher intensities and higher electron density would suggest more collisional quenching and

broadening of lines. Since, high BMEP engines can run at different load conditions (and hence different in-cylinder pressures during ignition timing), one would expect varying effect of these high pressures on LIBS signal. However, this work shows no significant change in temperature and electron density when pressures were varied from 20.7 bar to 48.3 bar. This would suggest that varying pressures (at least for pressures of our interest) would have relatively little impact on performing LIBS for in-cylinder equivalence ratio monitoring.

## References

1. H. El-Rabii, S. B. Victorov, and A. P. Yalin, "Time-resolved spectroscopy of an air plasma generated by UV-nanosecond laser pulses," In submission to *J. Phys D*.
2. J. D. Dale, P. R. Smy, and R. M. Clements, "Laser ignited internal combustion engine-an experimental study," *SAE (SAE Paper 780329)*, 1539-1548 (1979).
3. P. D. Ronney, "Laser versus conventional ignition of flames," *Opt. Eng.* **33**, 510-521 (1994).
4. H. Kopecek, H. Maher, G. Reider, F. Winter, and W. E., "Laser ignition of methane-air mixtures at high pressures," *Exptl. Therm. and Fluid Sci.* **27**, 499-503 (2003).
5. G. Herdin, J. Klausner, E. Wintner, M. Weinrotter, and J. Graf, "Laser ignition-a new concept to use and increase the potentials of gas engines," in *ASME Internal Combustion Engine Division 2005 Fall Technical Conference*, (2005), pp. 1-9.
6. T. X. Phuoc and F.P.White, "Laser-Induced Spark Ignition of CH<sub>4</sub>/Air Mixtures," *Combustion and Flame* **119**, 203-216 (1999).
7. I. C. E. Turcu, M. C. Gower, and P. Huntington, "Measurement of KrF laser breakdown threshold in gases," *Opt. Commun.* **134**, 66-68 (1997).
8. J. P. Davis, A. L. Smith, C. Giranda, and M. Squicciarini, "Laser-induced plasma formation in Xe, Ar, N<sub>2</sub>, and O<sub>2</sub> at the first four Nd:YAG harmonics," *Applied Optics* **30**, 4358-4364 (1991).
9. R. Tambay and R. K. Thereja, "Laser-induced breakdown studies of laboratory air at 0.266, 0.355, 0.532, and 1.06  $\mu\text{m}$ ," *J. Appl. Phys.* **70**, 2890-2892 (1991).
10. G. V. Ostrovskaya and A. N. Zaidel, "Laser spark in gases," *Soviet Physics Uspekhi* **16**, 834-855 (1973).
11. D. Bradley, C. G. W. Sheppard, I. M. Suardjaja, and R. Wooley, "Fundamentals of high-energy spark ignition with lasers," *Combustion and Flame* **138**, 55-77 (2004).
12. C. G. Morgan, "Laser-induced breakdown of gases," *Rep. Prg. Phys.* **38**, 621-665 (1975).
13. T. X. Phuoc, "Laser spark ignition: experimental determination of laser-induced breakdown thresholds of combustion gases," *Opt. Commun.* **175**, 419-423 (2000).
14. N. Glumac and G. Elliott, "The effect of ambient pressure on laser-induced plasmas in air," *Optics and Lasers in Engineering* **45**, 27-35 (2007).

15. S. Yalcin, D. R. Crosley, G. P. Smith, and G. W. Faris, "Influence of ambient conditions on the laser air spark," *Appl. Phys. B* **68**, 121-130 (1999).
16. M. M. Litvak and D. F. Edwards, "Electron Recombination in Laser-Produced Hydrogen Plasma," *Journal of Applied Physics* **37**(12), 4462-4474 (1966).
17. L. J. Radziemski and D. A. Cremers, eds., *Laser-induced plasmas and applications* (1989).
18. M. Young and M. Hercher, "Dynamics of Laser-Induced Breakdown in Gases," in *Journal of Applied Physics*, (1967), pp. 4393-4400.
19. S. G. Dinev, K. V. Stamenov, K. A. Stankov, and N. K. Uluchev, "Saturation effects in laser plasma X-ray emissions," *Optical and Quantum Electronics* **13**(3), 255-257 (1980).
20. H. R. Griem, *Principles of Plasma Spectroscopy* (2005).
21. R. W. Schmieder, "Techniques and applications of laser spark spectroscopy," presented at the Laser 83 Conference Proceedings, New Orleans, 1983.
22. D. A. Cremers and L. J. Radziemski, *Handbook of laser-induced breakdown spectroscopy* (John Wiley, Chichester, England; Hoboken, NJ, 2006), pp. xviii, 283 p., [210] p. of plates.
23. NIST, "Atomic Spectra database," <http://physics.nist.gov>.
24. M. Akram, "Two-dimensional model for spark discharge simulation in air," *AIAA J.* **34**, 1835-1842 (1996).
25. H. R. Griem, *Spectral Line Broadening by Plasmas* (Academic, New York), 1974), pp. 282-296.
26. L. L. Wiese and J. A. Augis, "Time and space resolved spectroscopic studies of electrical breakdowns in an argon-hydrogen mixture," *J. Appl. Phys.* **48**, 4528-4535 (1977).
27. S. Busher, T. Wruble, S. Ferri, and H.-J. Kunze, "The Stark width and shift of the hydrogen H $\alpha$  line," *Journal of Physics B: Atomic Molecular and Optical Physics* **35**, 2889-2897 (2002).
28. E. Oks, *Stark Broadening of Hydrogen and Hydrogenlike Spectral Lines in Plasmas* (Alpha Science International Ltd., 2006).
29. O. A. Bukin, I. V. Bazarov, N. S. Bodin, A. A. Il'an, and B. D. Kiselev, "Influence of the pressure of a gaseous atmosphere on the characteristics of the emission spectra of a laser plasma generated on the surfaces of solid targets," *Quantum Electronics* **28**(8), 685-688 (1998).
30. C. O. Laux, T. G. Spence, C. H. Kruger, and R. N. Zare, "Optical diagnostics of atmospheric pressure air plasmas," *Plasma Source Science and Technology* **12**, 125-138 (2003).
31. C. G. Parigger, D. H. Plemmons, and E. Oks, "Balmer series H $\beta$  measurements in laser induced hydrogen plasma," *Applied Optics* **42**(30), 5992-6000 (2003).

32. J. P. Singh and S. N. Thakur, *Laser-Induced Breakdown Spectroscopy* (2007).

# Chapter 3

---

## Experimental Study of Optical Fibers for Spark Delivery and Laser Ignition in Gases

Fiber optic delivery of sparks in gases is challenging as the output beam must be refocused to high intensity ( $\sim 300 \text{ GW/cm}^2$  for ns pulses). Analysis suggests the use of coated hollow core fibers, fiber lasers and photonic crystal fibers (PCFs). The effects of launch conditions and bending for 2-m long coated hollow fibers are studied and an optimum launch f# of  $\sim 55$  allowing spark formation with  $\sim 98\%$  reliability for bends up to Radius of Curvature (ROC) of 1.5 m in atmospheric pressure air is found. Spark formation using the output of a pulsed fiber laser is described and delivery of 0.55 mJ pulses through PCFs is shown.

### 3.1 Introduction

Initial demonstrations of the use of laser sparks to ignite combustible mixtures were performed in the late 1960s<sup>1,2</sup> and in recent years a relatively large number of studies have been performed<sup>3-12</sup>. By tightly focusing the beam from a high power pulsed laser, a

combustion-initiating spark can be created. The first use of laser ignition for operation of an engine was performed by J.D. Dale using a CO<sub>2</sub> laser<sup>2</sup>. Since then, a number of studies have investigated laser ignition for engine operation<sup>13-15</sup>. Laser ignition is of particular interest in stationary reciprocating gas engines<sup>9,11,13,16</sup>, in gas turbine engines where igniter lifetime is a limitation and in aircraft engines where flame extinction and relighting in adverse high altitude operation can be problematic<sup>17</sup>. Laser ignition for this work is primarily intended for large (Megawatt class) stationary gas engines that are typically used for power generation and natural gas compression. Technology drivers include the need for increased efficiency and reduced pollutant emissions which are trending advanced engines towards lean (reduced emissions) and high pressure (increased efficiency) operation. Achieving this mode of operation is intimately connected to the ignition and relatively high cost can be tolerated for an advantageous ignition system. Laser ignition is viewed as an attractive candidate technology as studies have shown potential for increased lean limits<sup>2,16</sup>. Further, in contrast to conventional spark ignition (where the voltage requirement, dielectric breakdown and erosion increase with pressure), laser ignition becomes easier at elevated pressures (breakdown threshold intensity decreases)<sup>18</sup>. Briefly, the differences (potential benefits) of laser spark ignition stem from two sets of effects: the first is associated with the ability to freely locate the spark within the combustion volume (by selection of appropriate focusing optics) and obviation of electrodes (which act as heat sinks and may provide catalytic chemistry), while the second is related to inherent physical differences between the two types of spark, for example, the higher pressure and temperature of laser sparks can lead to elevated (“overdriven”) early flame speed in laser ignition<sup>12</sup>.

A key challenge for practical laser ignition systems is the need for fiber optic delivery. The open beam paths used in most laboratory experiments are not considered practical for field (commercial) implementation due to safety, maintenance, thermal and vibrational issues. For gas engines of interest several approaches are under investigation: i) use of a laser per cylinder<sup>19</sup>, ii) use of a single laser per engine multiplexed through fibers to individual cylinders<sup>20</sup>, and iii) an intermediate approach in which (laser) pump light is fiber delivered from a single source to gain elements (amplifiers) located on each cylinder<sup>21</sup>. Current research interest is in the second approach for which fiber delivery of high peak-power (~MW) pulsed laser beams is required in such a way that allows spark formation (in the gas phase) after exiting the fiber. This capability would have general application for ignition of many other combustion devices in which laser ignition may have applicability (turbines, aircraft etc.).

The ability to fiber optically deliver laser sparks (in the gas-phase) would also advance practical Laser Induced Breakdown Spectroscopy (LIBS) systems. Although fiber delivery and signal collection are routinely used for solid- and liquid- phase LIBS (where breakdown thresholds are orders of magnitude lower), gas-phase LIBS systems do not currently use fiber delivery. Note that laser ignition of engines affords the possibility of a range of optical diagnostics including LIBS (with the combustion initiating spark), and optical emission spectroscopy (of the combustion light). The laser delivery inherently provides a “window” into the combustion cylinder. Further, while existing optical sensors in engines often suffer from window-fouling, there is evidence that passage of the high-power beam through the window can maintain window cleanliness<sup>22</sup>. These in-cylinder

diagnostics have the potential to monitor ignition vitality, knock-formation, air-to-fuel ratio formation of pollutant species etc<sup>23-25</sup>.

Owing to the relatively high breakdown intensity in gases ( $300 \text{ GW/cm}^2$ )<sup>6,9,15,26-29</sup>, the required fiber delivery is optically challenging<sup>14</sup>. The essential problem is the need to deliver relatively high power energy with sufficient beam quality to refocus the light to the intensity required for breakdown. Solid core silica fibers have been investigated but without success in forming optical sparks in air (at atmospheric pressure)<sup>14,17</sup>. As will be further discussed, photonic crystal fibers have been used for spark delivery at elevated pressure but only for low pulse energies ( $< \sim 1 \text{ mJ}$ ) that are insufficient for ignition of lean fuel/air mixtures. In earlier work, Yalin et al. showed the first fiber delivery of sparks in atmospheric pressure through the use of coated hollow core fiber optics<sup>28</sup>.

The layout of this chapter is as follows. In Section 3.2, a Figure of Merit (FOM) analysis for assessing intensity delivery capability of candidate fibers is presented. Based on the analysis, the potential of candidate fibers is discussed. In Section 3.3, results of experiments with 2-m long hollow core fibers including effects of launch and bending are presented. In Section 3.4, PCF fibers for spark delivery are discussed including a study of energy delivery through a 25 micron large mode area (LMA) fiber. Section 2.5 shows the use of high peak-power pulsed fiber laser for spark formation and the last section of the paper presents conclusions including outlook for a multi-pulse approach to obtain sparks with enough ignition energies.

### 3.2 Optical requirements for Fiber Delivered Ignition

For laser ignition in our work common Q-switched nanosecond laser sources (e.g. Nd:YAG lasers) is considered. For nanosecond optical pulses, non-resonant breakdown of gases is generally an intensity limited process<sup>6,9,15,26-29</sup>. As discussed in Chapter 1, in addition to achieving breakdown, successful ignition requires a minimum (ignition) pulse energy. The combination of delivered pulse energy and focused intensity is determined by the focusing optics and the beam's energy, time duration, and beam spatial quality ( $M^2$ ). The advanced high BMEP gas engines in interest are generally for lean-operation, for which at least 15-20 mJ of pulse laser energy is required<sup>9</sup>.

In the absence of fiber optics, it is straightforward to focus the output of a Q-switched (nanosecond) laser with pulse energy ~15 mJ (and reasonable beam quality) to form a gas-phase spark. However, spark formation after passage through a fiber is more challenging (as the fiber degrades the beam quality). To ground the discussion, the problem can be framed in terms of a standard solid silica fiber. In that case, owing to the damage intensity of the fiber material ( $\sim 1\text{-}3\text{GW}/\text{cm}^2$ )<sup>14,17,30</sup>, one requires a relatively large diameter multimode fiber ( $\sim 300\ \mu\text{m}$ ) to transmit the needed ignition energy ( $\sim 15\text{-}20\ \text{mJ}$ ). However, light exiting such a fiber is spatially multimode ( $M^2 \sim 100$  from simple estimation based on a waist of  $150\ \mu\text{m}$  and base NA of 0.22) which limits the ability to focus to a small spot in order to reach the intensity required for breakdown. Indeed, experimental work (in gases at atmospheric pressure) using conventional fibers has failed to show delivery of nanosecond pulses to form sparks<sup>14,17</sup>.

In order to explore potential fiber delivery candidates a Figure of Merit approach is presented to assess the intensity achievable after refocusing the light. The FOM is (approximately) equal to the achievable optical intensity (at the desired spark location downstream of the fiber) divided by the breakdown intensity requirement for atmospheric pressure air (for typical 5-10 ns pulses of Q-switched lasers). Therefore, a candidate fiber should have a FOM exceeding approximately unity for spark formation in air. The achievable intensity is found from the intensity at the fiber exit and the magnification of the post-fiber optical (imaging) system. The relevant parameters are shown in Figure 3.1.

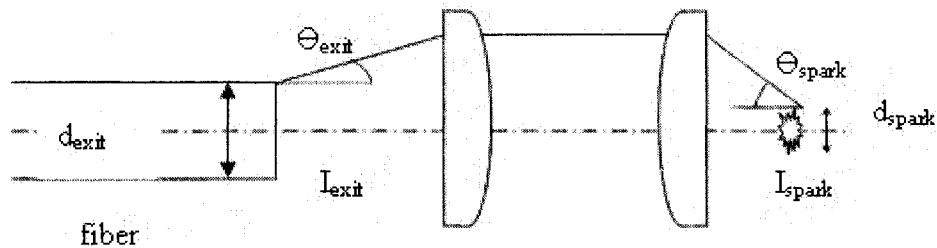


Figure 3.1: Schematic of the laser light exiting the fiber.

The diameter and intensity of light at fiber exit face are represented by  $d_{\text{exit}}$  and  $I_{\text{exit}}$  respectively, while the corresponding quantities at the (intended) spark location are given by  $I_{\text{spark}}$  and  $d_{\text{spark}}$ . The angular divergence of light exiting the fiber and converging at the spark location are represented with  $\Theta_{\text{exit}}$  and  $\Theta_{\text{spark}}$  respectively.

Ray tracing (geometric optics) or the Lagrange invariant gives the magnification of the imaging system as  $\Theta_{\text{exit}}/\Theta_{\text{spark}}$  so that the dimension of light at the spark location is:

$$d_{spark} = \frac{\theta_{exit}}{\theta_{spark}} d_{exit} \quad (1)$$

Assuming negligible loss through the lenses, the corresponding intensity at spark location becomes:

$$I_{spark} = I_{exit} \left( \frac{\theta_{spark}}{\theta_{exit}} \right)^2 \quad (2)$$

We define the Figure of Merit (FOM) as the optical intensity at the spark location divided by the breakdown intensity for atmospheric pressure air,  $I_{BD,atm}$ :

$$FOM \equiv \frac{I_{spark}}{I_{BD,atm}} = \frac{I_{exit}}{I_{BD,atm}} \left( \frac{\theta_{spark}}{\theta_{exit}} \right)^2 \quad (3)$$

The FOM expression in equation 3 shows that in order to achieve a high intensity at the intended spark location, one requires a high intensity at the fiber exit ( $I_{exit}$ ) as well as low divergence  $\theta_{exit}$  at the fiber exit. The latter requirement corresponds to a high beam quality (low  $M^2$ ). Further one wants highly converging light at the spark location corresponding to high  $\theta_{spark}$  (a low  $f\#$  final lens or imaging system). For fiber comparison the fiber-independent parameters is fixed as  $I_{BD,atm} = 300 \text{ GW/cm}^2$  and a (relatively low) final  $f\# = 2$  ( $\theta_{spark} = 0.25$ ) is assumed. These parameters are selected somewhat conservatively in the sense that somewhat lower intensities may provide breakdown and higher  $\theta_{spark}$  may be possible (ultimately limited by aberrations). Under these assumptions the FOM for candidate fibers is calculated by using representative values for achievable exit intensity and exit divergence angle (fiber NA) from the literature.

Table 3.1: Calculated FOM values for different fibers.

<b>Fiber</b>	<b><math>I_{\text{exit}}</math> (GW/cm<sup>2</sup>)</b>	<b><math>\theta_{\text{exit}}</math> (rad)</b>	<b>FOM</b>
Solid core silica fiber (base NA)	3	0.05	0.25
Coated Hollow Fiber	2	0.01	4.17
Fiber Laser	8	0.02	4.17
Photonic Crystal Fiber	12	0.04	1.56

Table 3.1 shows the resulting FOM values for multimode solid core fibers<sup>14</sup>, coated hollow core fibers<sup>28</sup>, photonic crystal fibers<sup>31</sup> and fiber lasers<sup>32</sup>. The values in Table 3.1 are initial values for rough assessment and should not be viewed as exhaustive. Outlook and comments for each fiber type are given below.

FOM values are proportional to the intensity achievable after refocusing laser pulses exiting the candidate fibers. For a given fiber, the magnitude of the FOM is indicative of the ability to spark at atmospheric pressure (requiring  $\text{FOM} \geq 1$ ). The analysis is somewhat idealized in terms of effects such as spatial mode distribution and hot-spots; however, the Figure of Merit (FOM) can also be found from  $M^2$  concepts by using

embedded Gaussian method concepts to determine the beam waist at the spark location<sup>33</sup>. If one assumes an initial beam waist located at the fiber exit and equal to the fiber radius, and a second waist located at the spark location and equal to the spark radius then the Figure of Merit can be equivalently expressed as:

$$FOM \equiv \frac{I_{spark}}{I_{BD,atm}} \approx \frac{I_{exit}}{I_{BD,atm}} \left( \frac{\pi d_{exit} \theta_{spark}}{2M_{exit}^2 \lambda} \right)^2 \quad (4)$$

The adopted values of  $I_{BD,atm}$  and  $\Theta_{spark}$  are also somewhat problematic as published data for the intensity breakdown threshold has considerable scatter ( $\sim \pm 50\%$ )<sup>26, 27, 29</sup>, and the minimum achievable f# will vary with the details of the light's spatial mode and focusing optics (ultimately limited by aberrations). Despite these limitations the FOM analysis provides a useful framework for fiber assessment and interpretation of experimental results.

In terms of the outlook for various fiber candidates for gas-phase spark ignition at atmospheric condition following results are presented: The FOM for solid fibers with base NA of 0.22 is considerably less than unity showing them to be unsuitable for atmospheric pressure fiber delivery, an outlook that is consistent with experiments<sup>14</sup>. On the other hand, the FOM does suggest the potential utility of solid fibers when operated with lower output NA and at high pressures where the breakdown threshold intensity ( $I_{BD}$ ) decreases<sup>17</sup>. Coated hollow fibers differ from solid fibers primarily in regards to having lower exit divergence (lower  $M^2$ ) resulting in  $FOM > 1$  and showing potential for spark delivery, as has been demonstrated<sup>28</sup>. For both hollow and solid fibers, the intensity limit is related to optical damage thresholds. For solid silica fibers, the upper limit of intensity is due to laser-induced damage of bulk fused silica, though as discussed in

Reference 35 (and references therein), measured damage intensities for multimode fibers are generally lower. The intensity limit for coated hollow fibers is generally due to optical damage of the reflective coating<sup>34</sup>. Fiber laser and PCFs both have FOM>1 indicating their utility for high intensity delivery, and spark formation has been demonstrated with fiber lasers (this work) at atmospheric pressure and with hollow core PCFs at elevated pressure<sup>35</sup>. Note that these demonstrations have been for delivered energies is in the range of ~ 1 mJ which is not sufficient for ignition of lean mixtures. In principle, fiber lasers can have different type of fibers as output, but for initial FOM assessment parameters from published reports of high power fiber lasers are used<sup>32</sup>.

### **3.3 Hollow Core Fiber Testing**

Initial research on the use hollow fibers for laser spark delivery proved unsuccessful<sup>14</sup>. Past work showed that with an appropriate fiber launch laser air sparks could be delivered through the cyclic olefin polymer coated hollow fiber shown in Fig. 3.2<sup>28</sup>. From initial experiments with 700  $\mu\text{m}$  core fibers, successful spark formation (~97%) at atmospheric condition was obtained for launch f# of ~ 72. In this case, the exit beam divergence was measured at 0.011 corresponding to  $M^2$  of 11 and focal intensity of about 300  $\text{GW}/\text{cm}^2$  at the spark location. A similar setup with 1m long fiber was also used on a single cylinder of an engine demonstrating (the first) successful fiber delivered ignition of a gas engine<sup>36</sup>.

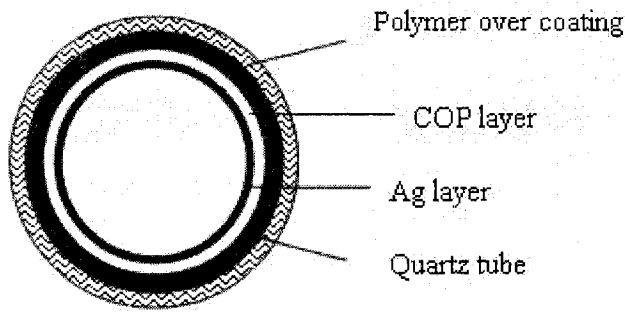


Figure 3.2: Cross-sectional view of the coated hollow core fiber.<sup>10,28</sup>

---

In order to develop more flexible systems suitable for engine environments, longer fibers are required. For example, the cylinders of modern megawatt class gas-engines are typically separated from one another by as much as 2-m. In this work, investigation of a 2 m long cyclic olefin polymer (COP) coated hollow core fiber with core diameter of 1mm is reported. The experimental set-up is shown in Fig. 3.3.

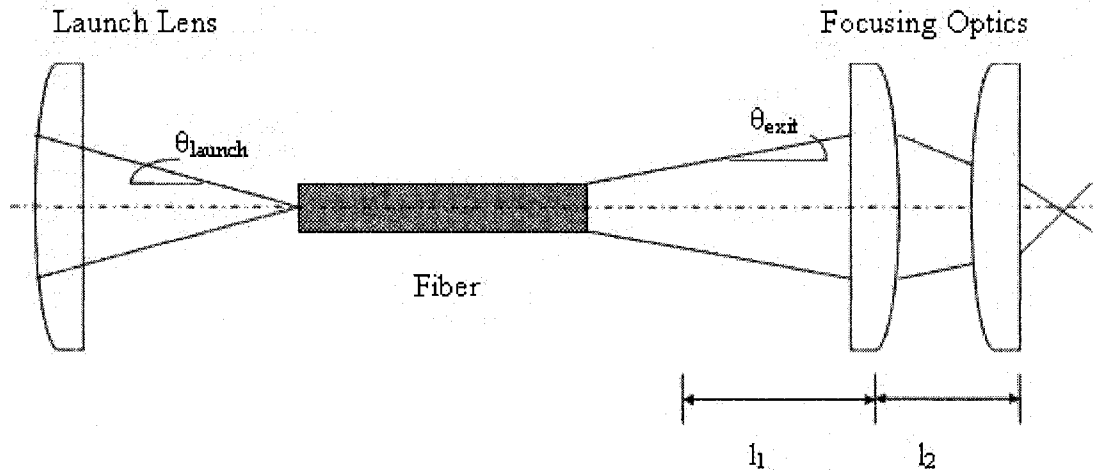


Figure 3.3: Schematic Setup for 2m long hollow core fiber.

---

The light source was the fundamental 1064 nm beam of a Q-switched Nd:YAG laser (Big Sky) with pulse duration of 8 ns, repetition rate of 10 Hz, and spatial beam quality  $M^2 < 2$ . The light was focused into the fiber with a single plano-convex lens. In order to understand the effect of input launch f# on the beam properties of the fiber, experiments with three input f#s: 35, 55 and 85 were conducted. In some cases, air breakdown was observed at the input face of the fiber due to high intensity at the input focal area. A weak helium purge was used in order to prevent sparking at the input of the fiber. It is well understood that the launch condition has a significant impact on mode coupling, transmission and the output beam quality of the hollow core fiber<sup>28,37,38</sup>. A 5-axis fiber holder was used for optimizing the launch alignment. For initial tests, the fiber was kept relatively straight. The exit beam was focused using a pair of lens with focal length of 120 mm and 8 mm empirically found to be an effective focusing combination. The first (longer focal length) lens was placed at approximately 300mm ( $l_1$ ) downstream of the fiber exit, with the final focusing lens about 20 mm ( $l_2$ ) downstream of the first focusing lens. Spot diameters were calculated using a Spiricon beam profiler.

Table 3.2: Effect of Launch Geometry on 2m Long Hollow Waveguides.

$f_{\text{launch}}$	$f_{\text{input}}$	$w_{\text{launch}}$	$\theta_{\text{exit}}$	$M^2_{\text{exit}}$	$I_{\text{exit}}$	$w_{\text{focus}}$	$I_{\text{focus}}$	Transmission	Sparking
(mm)		( $\mu\text{m}$ )	(rad)		( $\text{GW}/\text{cm}^2$ )	( $\mu\text{m}$ )	( $\text{GW}/\text{cm}^2$ )	(%)	(%)
135	35	27	0.014	21	0.58	35	120	80	<10
215	55	39	0.01	15	0.6	27	470	86	98
335	85	140	0.015	22	0.5	44	68	80	0

Table 3.2 summarizes the effect of launch condition on the performance of the fiber. The focal length of the launch lens and input f-number are represented by  $f_{\text{launch}}$  and  $f_{\#}$  respectively while the angular beam divergence at the fiber exit is given by  $\Theta_{\text{exit}}$ . The (measured) focal spot size at the waist and final focused (spark) location are represented by  $w_{\text{launch}}$  and  $w_{\text{focus}}$ . The intensities at the fiber exit and final focused (spark) location are represented by  $I_{\text{exit}}$  and  $I_{\text{focus}}$  (where the former is computed based on the fiber area and the latter based on  $w_{\text{focus}}$ ). We also report the  $M^2$  exit of the beam, fiber transmission, and the percentage of delivered sparks resulting in spark delivery.

Of the conditions tested, optimal spark formation (~98% of laser shots) and exit beam parameters was found for input  $f_{\#}$  ~55. This launch configuration resulted in the lowest beam exit divergence ( $\Theta_{\text{exit}}$  ~ 0.014) corresponding to  $M^2$  of ~15 at the fiber exit. With pulse energy of ~35 mJ for this condition, the focal intensity was as high as ~ 470

GW/cm<sup>2</sup> well above the break down threshold intensity. The occasional (2%) misfires are thought to be due to varying multimode spatial profile (hot spots) in the exit beam<sup>28, 39</sup>. It was also found that as the f# was increased (f# ~85) or decreased (f# ~35) in relation to this condition, the fiber transmission and the exit beam quality degraded suggesting an optimum launch f#. This behavior is consistent with past findings for hollow fibers and is associated with the mode coupling and mode distribution of light in the fiber<sup>37</sup>.

Table 3.3: Effect of Bending Configuration for input f# = 55.

$1/R$	$w_{\text{launch}}$	$\theta_{\text{exit}}$	$M^2_{\text{exit}}$	$I_{\text{exit}}$	$w_{\text{focus}}$	$I_{\text{focus}}$	Transmission	Sparking
(m <sup>-1</sup> )	( $\mu\text{m}$ )	(rad)		(GW/cm <sup>2</sup> )	( $\mu\text{m}$ )	(GW/cm <sup>2</sup> )	(%)	(%)
0	39	0.01	15	0.6	17	470	86	98
0.66	39	0.011	16	0.58	21	300	83	98
1	39	0.019	29	0.5	49	53	80	0

The effects of fiber bending on the fiber performance were also explored. Tests were conducted for the input f# of 55, which provided the highest sparking at straight configuration. In these experiments, the first 100 cm of the fiber was kept straight while the remaining 100 cm was bent into arcs of different radii of curvature (R). As shown in Table 3.3, and consistent with past research<sup>28,38</sup> it was found that as the fiber was bent,

transmission of the fiber dropped and the exit beam divergence and corresponding  $M^2$  increased. It was also found that for small bending ( $R=1.5$  m) the performance remained comparable to that of straight configuration and provided enough spatial beam quality at fiber output to give a high sparking rate ( $\sim 98\%$ ). With further bending (i.e.  $R= 1$ m), the sparking reduced to zero due to increase in the exit beam divergence ( $\sim 0.019$ ) and corresponding increase in  $M^2$ . This shows that while moderate fiber bending is possible, bending-loss (transmission and beam-quality) is one of the limitations of hollow fibers in this application.

### **3.4 Photonic Crystal Fiber Testing**

Photonic crystal fibers (PCFs) are a rapidly developing fiber technology which may have potential for spark delivery (Table 3.1). Output beam for these fibers are approximately single mode giving the potential to deliver high intensity. Recent research has investigated the use of both Large Mode Area (LMA) solid core PCF and hollow core photonic band gap (PBG) fibers for delivery of high power nanosecond pulses<sup>31, 40</sup>. S.O.Konorov et al., delivered a sequences of picosecond pulses with a total energy in the pulse train of about 1mJ through a hollow-core photonic-crystal fiber (PBG) with a core diameter of approximately  $14\mu\text{m}$ <sup>41</sup>.

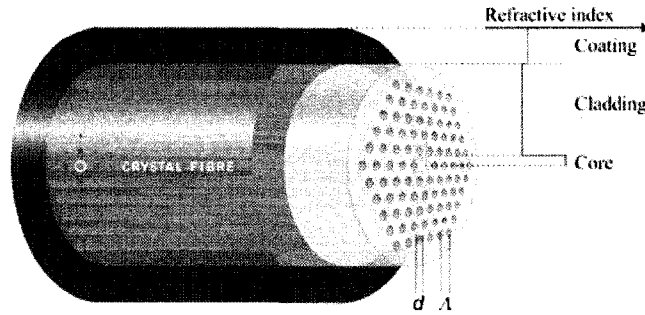


Figure 3.4: Large Mode Area solid core PCF fiber (from Crystal Fiber A/S).

Successful delivery of energy of 0.37 mJ for 1064 nm 65 ns pulses through hollow core PBG fibers has been demonstrated<sup>40</sup>. Transmitted pulse energies of 0.15 mJ through a hollow core PBG fiber been reported to run rich methane-air mixtures at high pressures<sup>35</sup>. However, in all published cases, the transmitted energy is well below the target of ~15mJ required for lean mixture operation in engines. In this work, a delivery of high energy pulses with sufficient fiber exit beam quality for spark delivery is targeted. To this end, large mode area (LMA) photonic crystal fibers (Fig.3.4) are investigated. While PBG fibers are also of interest, the published work indicates that as the core diameter is increased to transmit higher energy, PCFs can (in practice) sustain higher damage threshold than PBG fibers<sup>31</sup>. The periodic hole-silica structure in the PCF fiber (Fig.3.4), modifies the refractive index of the cladding and maintains an appropriate relationship between the refractive index of the core and the cladding so as to operate it in a single mode.

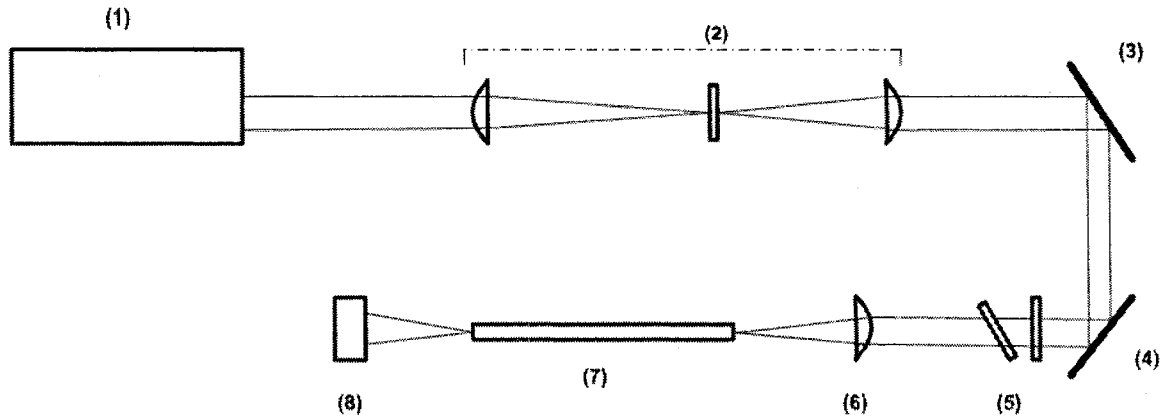


Figure 3.5: Experimental Setup for photonic Crystal Fiber; (1) Laser, (2) Spatial filter setup, (3) Mirror ,(4) Mirror, (5) Variable attenuator, (6) Focusing lens, (7) PCF and (8) Energy meter.

---

Experimental investigation was conducted to characterize LMA PCF of length 2-m and core diameter of 25  $\mu\text{m}$ . The fiber used has a relatively low input NA of 0.04 - 0.07. The experimental setup is shown in Fig 3.5. The ends of the fiber were connectorized with high power SMA connectors. A spatial filter setup was used to improve the beam quality of the laser ( $M^2 \sim 1.4$  after the spatial filter). A variable attenuator allows controlled attenuation of the beam from a few mJ down to  $\mu\text{J}$  of energy without displacing the beam. The beam was launched with a 50 mm focal length lens onto the fiber input which was held with a 5-axis fiber holder.

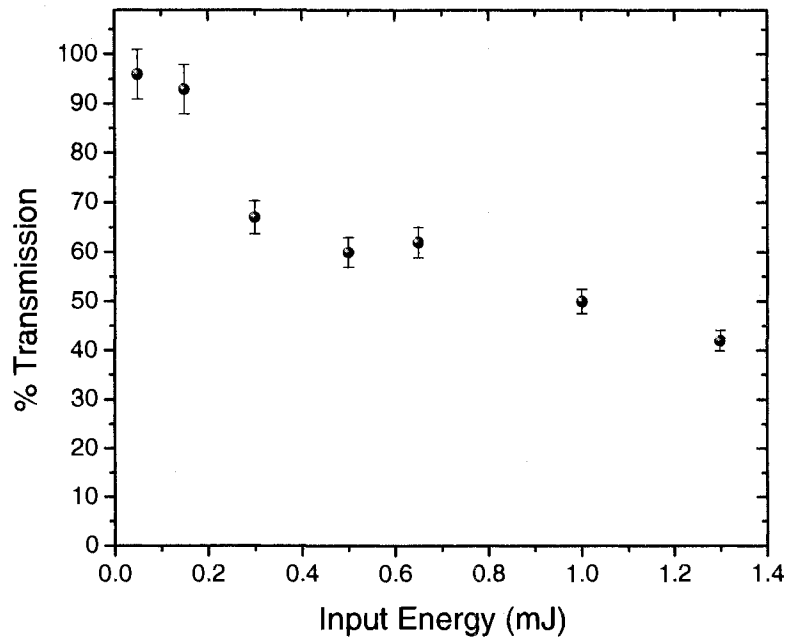


Figure 3.6: Transmission of a 25 $\mu$ m core LMA-PCF.

Figure 3.6 shows the fiber transmission measured as a function of the input pulse energy. A discontinuous behavior in the transmission is observed. This might be due to slight shifts in the beam position or profile between measurements. It was found that as the pulse energy increased, the fiber transmission decreased from around  $\sim 97\%$  to  $\sim 45\%$ . In these tests, the maximum achievable input energy was 1.3 mJ corresponding to an output of 0.55 mJ. This output energy is still too low for ignition of lean mixtures, but is amongst the highest reported for PCFs and is more than 3 times higher than that achieved in past PBG experiments showing ignition of rich methane-air mixture<sup>35</sup>.

### 3.5 Solid Core Silica Fiber Testing

Previous attempts to deliver laser sparks at atmospheric condition with multimode solid core silica fibers have been unsuccessful due to the high degree of beam quality degradation. However, the reduction in breakdown threshold intensity ( $I_{thr}$ ) with pressure facilitates spark formation at higher pressures<sup>18,42</sup>. According to FOM analysis, solid core fibers (with base NA) are incapable of laser spark formation at atmospheric conditions. However, their use may become feasible with a reduction in output NA or at high pressure conditions. For example, if the output NA could be reduced by a factor of 2 (example by tailoring the input launch) and the ambient pressure were 15 bar, then the FOM would improve by  $\sim 12$  ( $2^2/15^{-0.4}$ , see eqn. 3 and Section 1.2.3 in Chapter 1) and such a configuration would be expected to spark. Indeed, Gaborel et al. showed optical spark formation ( $\sim 90\%$  of the laser shots) through 940  $\mu\text{m}$  diameter solid core step index fibers at 6 bars with input energy of  $\sim 52\text{mJ}$  (6 ns pulses) for appropriate launch conditions<sup>17</sup>. These results show promise for use of solid core fibers for engine applications with high cylinder pressures.

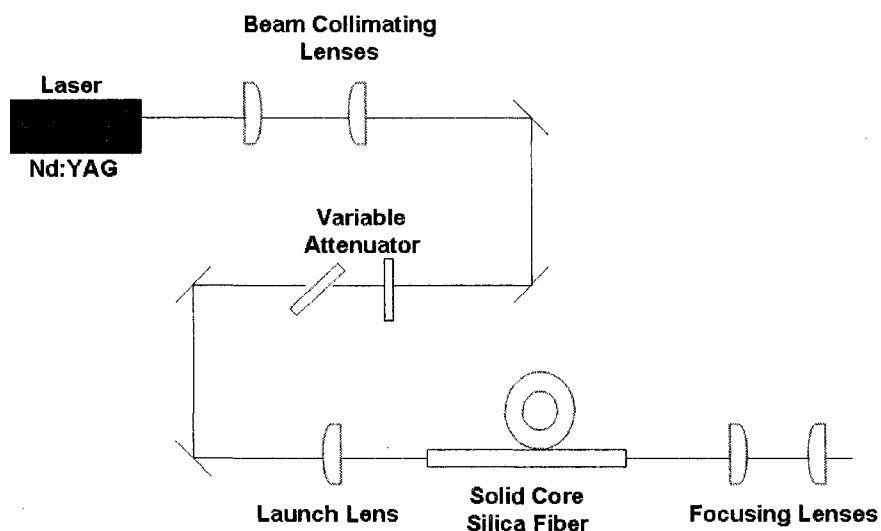


Figure 3.7: Experimental Setup for solid core fibers.

---

To characterize solid core fibers for potential laser spark formation and delivering required pulse energies, performance of 2 m long solid core step index fibers with core diameters of 400, 600 and 910  $\mu\text{m}$  were studied. For testing at engine conditions, a high pressure test cell pressurized to  $\sim 15$  bar (corresponding to lower side of typical in-cylinder pressures,) was used. At this pressure, the breakdown threshold intensity  $I_{\text{thr}}$ , was directly measured and found as approximately  $100 \text{ GW}/\text{cm}^2$  for reliable sparking (consistent with published data). Based on the published energy requirements for ignition<sup>9</sup>, a minimum transmitted energy of 15-20 mJ was (conservatively) assumed to be required. Figure 3.7 shows the experimental setup. A 1064 nm Nd:YAG laser operating at 10 Hz (with 8 ns pulses and 50 mJ pulse energies) was used as the light source. A plano-convex lens of focal length 100 mm and beam diameter 2.8 mm provided a launch NA of 0.014. In order to not exceed the damage limit of the fiber, the input face of the

fiber was placed downstream of the focused spot size so that the expanding laser beam filled around 80% of the core diameter. A variable beam attenuator was used to adjust the beam power. An overlapping low power He-Ne laser was used for aligning the fiber with the pulsed laser. A smaller beam diameter at the fiber output (imaged with a CCD monitor) with near Gaussian structure was used as an indication of good alignment. The first 100 cm of the fiber was kept straight and the remaining section was bent to a radius of 50 cm (to emulate practical requirements for on-engine applications). The beam at the exit of the fiber was focused to a spot size of diameter ( $d_f$ ) with a pair of two lens. The achievable intensity at the spark location depends on the focal spot size which in turn varies with the core diameter ( $d$ ) and the magnification of the imaging system , as shown in eqn. 1.

The first collimating lens had a variable focal length  $f_1$  (which depends on the degree of beam divergence at the fiber exit) while the second focusing lens had a focal length ( $f_2$ ) of approximately 9 mm (with clear aperture of 8mm). Higher demagnifications can be achieved by using collimating lenses with longer focal lengths, but this is constrained by the maximum possible collimated beam diameter of 8 mm (which is equal to the clear aperture of the final focusing lens).

Table 3.4: Beam properties at the solid core step index fiber exit.

Core Diameter, d ( $\mu\text{m}$ )	$\theta_{\text{exit}}$ (rad)	$M^2$	Focal spot size, $d_f$ ( $\mu\text{m}$ )	FOM
400	0.064	38	64	0.46
600	0.047	42	71	1.13
910	0.036	48	82	1.11

As shown in Table 3.4, the beam quality ( $M^2$ ) increased with increasing core diameter while the beam divergence at the fiber exit decreased with increasing core diameter. Corresponding focal spot diameter at the focal spot ( $d_f$ ) are also shown. The 400  $\mu\text{m}$  core diameter fiber has the lowest  $M^2$  of around 38 while the 910  $\mu\text{m}$  core fiber has  $M^2$  of around 48, which indicates that smaller focal spot sizes for 400  $\mu\text{m}$  is possible compared to 910  $\mu\text{m}$  (or 600  $\mu\text{m}$ ). The table also provides possible FOM values calculated from eqn. 4 assuming  $\theta_{\text{spark}}$  of 0.4 and  $I_{\text{BD}}$  of  $100 \text{ GWcm}^{-2}$ . As can be seen the FOM for 600 and 900  $\mu\text{m}$  core fibers are barely larger than 1, that is required for spark formation.

Table 3.5: Safe Energy limit for solid core step index fibers.

<b>Core Diameter</b>	<b>Safe Energy Limit</b>	<b>Safe Energy Limit</b>
<b>(<math>\mu\text{m}</math>)</b>	<b>(From Fiber Manufacturer)</b>	<b>(Experiment)</b>
	<b>(mJ)</b>	<b>(mJ)</b>
400	18	12
600	27	35
910	40	46

Table 3.5 (right-most column) shows the maximum input energies possible prior to fiber damage (in this experiment). Pulse energies of 12 mJ were possible for the 400  $\mu\text{m}$  core fiber, while 35mJ and 46 mJ input pulse energies were possible for 600  $\mu\text{m}$  and 910  $\mu\text{m}$  core fibers respectively. (Note that as much as 67 mJ of input pulse energy was occasionally possible for the 910  $\mu\text{m}$  fiber, but damage resulted above 46 mJ). Also shown in Table 3.5 (middle column) is the safe energy limit for the solid core fibers as determined from an energy limit nomograph from a fiber manufacturer (Fiber guide industries). Comparison of the two series of values shows that the experimental test results are reasonably consistent with expectations from fiber manufacturers (with slight discrepancy likely due to detailed variation in launch conditions and fiber fabrication and composition details. From the energy point of view the 400  $\mu\text{m}$  solid core fibers were deemed unsuitable (given the aforementioned criterion of 25 mJ and FOM). The higher core diameter fibers such as 600 and 910  $\mu\text{m}$  fibers (with a bend of 0.5m radius), are

capable of delivering the required energy; however, their relatively low beam quality (high  $M^2$ ) and barely high enough FOM makes it challenging to operate the fibers at safe energy limits and focus to the threshold intensity level of  $\sim 100 \text{ GW/cm}^2$ .

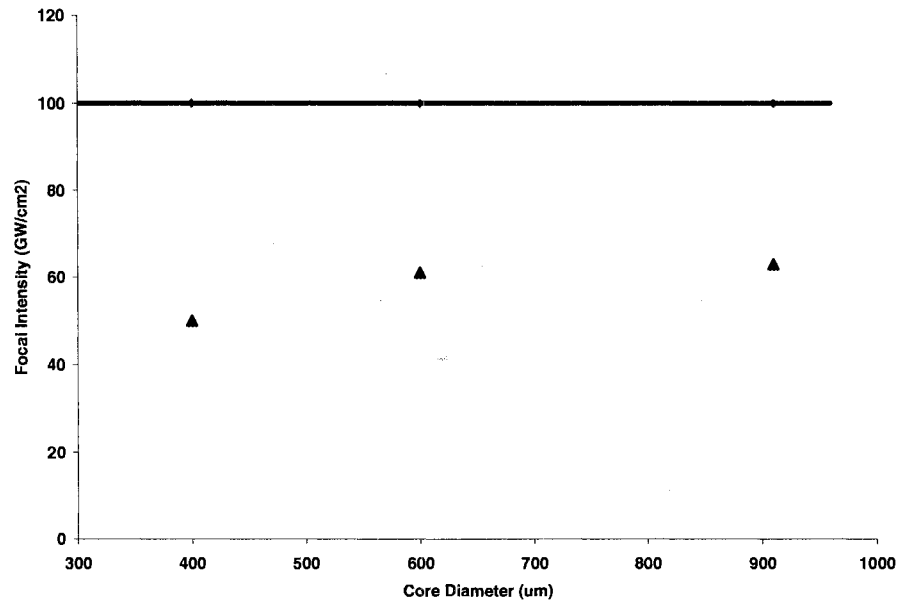


Figure 3.8: Achievable focal intensity for the solid core fibers: triangles – experimental results, line – required for spark formation at typical engine pressures.

Figure 3.8 shows (with triangles) the achievable focal intensity for the three fibers along with the required threshold intensity (straight line). Note that these results are for bent conditions. On the other hand similar experiments conducted with  $600 \mu\text{m}$  core diameter fibers at straight orientation did achieve spark formation at  $\sim 15$  bar with input energies of  $\sim 40 \text{ mJ/pulse}$ . It was noted during the experiments that a very accurate alignment of the fiber with the laser beam was required to prevent fiber damage.

### 3.6 Fiber Lasers

Fiber laser is one of the most attractive technologies for delivering laser sparks. The lasing medium in a fiber laser is the rare earth doped fiber itself and the output is delivered through the same lasing fiber. Therefore, fiber lasers form a basis for conveniently integrating the seed diode laser and the fiber delivery medium. An example of a setup of fiber laser is shown in Fig 3.9. The initial low power laser beam from 1064nm seed diode laser is amplified through a series of single mode amplifier (fibers) which is then fed to a series of rare earth Ytterbium (Yb) –doped multimode fibers. The rare earth Yb acts as a lasing material and amplifies the laser beam along its length. The output of this fiber laser can be focused to create laser sparks. Recent developments in fiber lasers include generation of 2.4 MW peak power for 4-ns pulses<sup>32</sup>.

The main technological development in fiber lasers have been the fiber core size increase. Experiments showing the ability to form optical sparks at the output of a pulsed fiber laser were conducted in collaboration with University of Michigan.

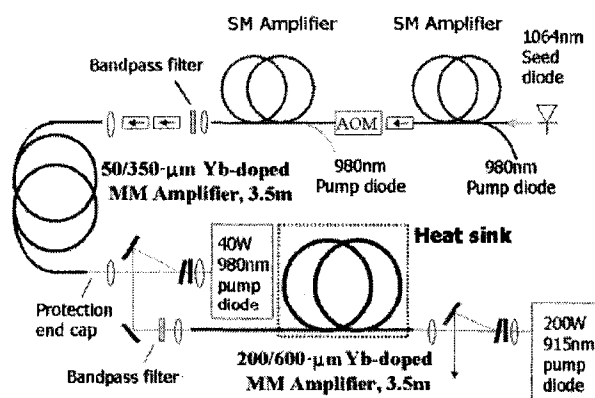


Figure 3.9: Experimental setup of the fiber laser.<sup>32</sup>

A multi-stage fiber amplifier system, seeded with electronically controlled nanosecond diode pulses, similar to the one described in Fig.3.9 was used. In the current system, however, the last amplification stage was constructed with an 80- $\mu\text{m}$  diameter core Yb-doped fiber, producing output beam quality of better than  $M^2 \sim 1.5$ . This combination of large core and high beam quality allowed to achieve spark-generation with 0.7-ns duration fiber laser pulses (corresponding to 2.4-mJ pulse energy and 3.4-MW peak power) at 50-Hz repetition rate. This demonstration was the first proof that fiber lasers were well suited for formation of optical sparks and confirms the findings of FOM analysis in section 3.2. Note that although the pulse duration is low, these sparks can readily allow ignition of gas engines operating at near stoichiometric conditions. Further optimization of laser pulse parameters, including further pulse energy increase is anticipated. Such an increase in parameters would then lead to parameters allowing ignition of targeted lean fuel engines.

### **3.7 Conclusions**

Fiber optic delivery of laser sparks is generally viewed as a requirement for practical laser ignition systems and may also enable other applications such as fiber-delivered gas-phase LIBS. A Figure of Merit analysis was used to identify candidate fibers from the point of view of intensity delivery as is required for spark formation. The analysis showed that high intensity and low divergence ( $M^2$ ) at fiber exit are required characteristics. For initial comparison of different fiber types, representative FOM values based on published values were calculated and favorable FOM values were found for hollow core fibers, fiber lasers and photonic crystal fibers.

An investigation of spark delivery using 2-m long coated hollow core fibers (a reasonable length for practical laser ignition systems on multi-cylinder engines) was conducted. It was found that with an optimum launch condition ( $f\# \sim 55$ ) for fiber transmission and exit beam quality reliable (98%) spark formation with transmission of pulses of  $\sim 35$  mJ could be obtained. It was shown that output energies of 0.55 mJ was achieved from LMA PCFs. First demonstration of spark formation at the output of a pulsed fiber laser having parameters  $\sim 0.7$  ns, 2.4 mJ was also presented. Based on these results, one can argue use of larger mode area fibers ( $40\mu\text{m} - 80\mu\text{m}$ ) to increase pulse energies (even at the expense of some degradation in the exit beam quality, since a somewhat elevated  $M^2$  would still allow spark formation).

According to the FOM analysis, solid core fibers (with base NA) were incapable of laser spark formation at atmospheric conditions. However, their use can become feasible with reduction in output NA and at higher pressure conditions. Indeed, laser spark formation using solid core fibers with reduced output NA (at straight orientation) and at higher elevated pressures (15 bar) was demonstrated in this experiment. A similar experiment was also demonstrated by G. Gaborel with 90% reliability at 6 atm pressure<sup>17</sup>. Fiber lasers were used to create laser spark at air with 0.7 ns and 2.4 mJ pulse energies.

None of the fibers except the hollow core coated fibers are capable to deliver laser spark with enough ignition energies. A multi pulse approach can be used for these fibers for lean ignition. This approach would allow PCFs and fiber lasers to create an initial spark with low energy short pulse laser beam followed by a long pulse with high energy

that can deposit the required ignition energy in the spark. This approach would allow for the delivery of ignition energies without exceeding the damage thresholds of the fibers.

## References

1. J. H. Lee, and Knystautas, R., "Laser spark ignition of chemically reactive gases," *AIAA Journal*, **7**(2)(1969).
2. J. D. Dale, P. R. Smy, and R. M. Clements, "Laser ignited internal combustion engine-an experimental study," *SAE (SAE Paper 780329)*, 1539-1548 (1979).
3. P. D. Ronney, "Laser versus conventional ignition of flames," *Opt. Eng.* **33**, 510-521 (1994).
4. T. A. Spiglanin, A. Mcilroy, E. W. Fournier, R. B. Cohen, and J. A. Syage, "Time-resolved imaging of flame kernels: laser spark ignition of H<sub>2</sub>/O<sub>2</sub>/Ar mixtures," *Combustion and Flame* **102**, 310-328 (1995).
5. J. X. Ma, T. W. R. III, and J. P. Buckingham, "Nd:YAG Laser Ignition of Natural Gas," presented at the ASME ICE - Spring Technical Conference, 1998.
6. T. X. Phuoc and F.P.White, "Laser-Induced Spark Ignition of CH<sub>4</sub>/Air Mixtures," *Combustion and Flame* **119**, 203-216 (1999).
7. T. X. Phuoc, "Brief Communication - Single Point Versus Multi-point Laser Ignition: Experimental Measurements of Combustion Times and Pressures," *Combustion and Flame* **122**, 508-510 (2000).
8. Y. L. Chen and J. W. L. Lewis, "Visualization of laser-induced breakdown and ignition," *opt. Exp.* **9**, 360-372 (2001).
9. H. Kopecek, H. Maher, G. Reider, F. Winter, and W. E., "Laser ignition of methane-air mixtures at high pressures," *Exptl. Therm. and Fluid Sci.* **27**, 499-503 (2003).
10. J. L. Beduneau, B. Kim, L. Zimmer, and Y. Ikeda, "Measurements of minimum ignition energy in premixed laminar methane/air flow by using laser induced spark.," *Combustion and Flame* **132**, 653-665 (2003).
11. M. Lackner and e. al., "Investigation of the early stages in laser-induced ignition by Schlieren photography and laser induced fluorescence spectroscopy," *Opt. Exp.* **12**, 4546-4557 (2004).
12. D. Bradley, C. G. W. Sheppard, I. M. Suardjaja, and R. Wooley, "Fundamentals of high-energy spark ignition with lasers," *Combustion and Flame* **138**, 55-77 (2004).
13. M. Weinrotter, H. Kopecek, M. Tesch, E. Wintner, M. Lackner, and F. Winter, "Laser ignition of ultra-lean methane/hydrogen/air mixtures at high temperature and pressure," *Exptl. Therm. and Fluid Sci.* **29**, 569-577 (2005).

14. A. Stakhiv, R. Gilber, H. Kopecek, A. M. Zheltikov, and E. Wintner, "Laser ignition of engines via optical fibers?" *Laser Phys.* **14**, 738-747 (2004).
15. G. Herdin, J. Klausner, E. Wintner, M. Weinrotter, and J. Graf, "Laser ignition-a new concept to use and increase the potentials of gas engines," in *ASME Internal Combustion Engine Division 2005 Fall Technical Conference*, (2005), pp. 1-9.
16. H. Kopecek, S. Charareh, M. Lackner, C. Forsich, F. Winter, J. Kausner, G. Herdin, and E. Wintner, "Laser Ignition of Methane-Air Mixtures at High Pressure and Diagnostics," *Jnl. of Eng. for Gas Turb. and Power* **127**, 213-219 (2005).
17. G. Gaborel, H. El-Rabii, P. Scouflaire, and J. C. Rolon, "Toward the development of laser ignition system for aircraft engines," presented at the Proceedings of First INCA, Workshop, Snecma, 2005.
18. T. X. Phuoc, "Laser spark ignition: experimental determination of laser-induced breakdown thresholds of combustion gases," *Opt.Commun.* **175**, 419-423 (2000).
19. M. McMillian and e. al., "Laser-Spark Ignition for Natural Gas Fueled Reciprocating Engines," presented at the Gas Machinery Conference, 2003.
20. A. P. Yalin, A. Reynolds, S. Joshi, M. Defoort, B. Willson, Y. Matsuura, and M. Miyagi, "Development of a fiber delivered laser ignition system for natural gas engines," in *ASME ICE Division 2006- Spring Technical Conference*, (Aachen, Germany, 2006).
21. M. Weinrotter, H. Kopecek, and E. Winter, "Laser ignition of engines," *Laser Phys.* **15**, 947-953 (2005).
22. T. X. Phuoc, "A comparative study of the photon pressure force, the photophoretic force, and the adhesion van der Wals force," *Opt.Commun.* **245**, 27-35 (2005).
23. F. Ferioli, P. V. Puzinauskas, and S. G. Buckley, "Laser-Induced Breakdown Spectroscopy for On-Line Engine Equivalence Ratio Measurements," *Applied Spectroscopy* **57**(9), 1183-1189 (2003).
24. Y. Hardalupas, M. Orain, C. S. Panoutsos, A. M. K. P. Taylor, J. Olofsson, H. Seyfried, M. Richter, H. Hult, M. Alden, F. Hermann, and J. Klingman, "Chemiluminescence sensor for local equivalence ratio of reacting mixtures of fuel and air (FLAMESEEK)," *Appl. Therm. Eng.* **24**, 1619-1632 (2004).
25. T. D. Fansler, B. Stojkovic, M. C. Drake, and M. E. Rosalik, "Local fuel concentration measurements in internal combustion engines using spark-emission spectroscopy," *Appl. Phys. B* **75**, 577-590 (2002).
26. I. C. E. Turcu, M. C. Gower, and P. Huntington, "Measurement of KrF laser breakdown threshold in gases," *Opt. Commun.* **134**, 66-68 (1997).
27. J. P. Davis, A. L. Smith, C. Giranda, and M. Squicciarini, "Laser-induced plasma formation in Xe, Ar, N<sub>2</sub>, and O<sub>2</sub> at the first four Nd:YAG harmonics," *Applied Optics* **30**, 4358-4364 (1991).

28. A. P. Yalin, M. Defoort, B. Willson, Y. Matsuura, and M. Miyagi, "Use of hollow-core fibers to deliver nanosecond Nd:YAG laser pulses to form sparks in gases," *Optics Letters* **30**(16), 2083-2085 (2005).
29. R. Tambay and R. K. Thereja, "Laser-induced breakdown studies of laboratory air at 0.266, 0.355, 0.532, and 1.06  $\mu\text{m}$ ," *J. Appl. Phys.* **70**, 2890-2892 (1991).
30. S. W. Allison, G. T. Gillies, D. W. Magnuson, and T. S. Pagano, "Pulsed laser damage to optical fibers," *Applied Optics* **24**, 3140-3145 (1985).
31. L. Michaille, D. M. Taylor, C. R. Bennett, T. J. Shephard, C. Jacobsen, and T. P. Hansen, "Damage threshold and bending properties of photonic crystal and photonic bandgap optical fibers," presented at the Proc. SPIE 5618, 20004.
32. M. Y. Cheng, Y. C. Chang, A. Galvanauskas, P. Mamidipudi, R. Changkakoti, and P. Gatchell, "High-energy and high-peak-power nanosecond pulse generation with beam quality control in 200  $\mu\text{m}$  core highly multimode Yb-doped fiber amplifiers," *Opt. Lett.* **30**, 358-360 (2005).
33. A. E. Siegman, "Output beam propagation and beam quality from a multimode stable cavity laser," *IEEE J. Quantum Electron* **29**, 1212-1217 (1993).
34. J. P. Parry, T. J. Stephens, J. D. Shephard, J. D. C. Jones, and D. P. Hand, "Analysis of optical damage mechanisms in hollow-core waveguides delivery nanosecond pulses from a Q-switched Nd:YAG laser," *Applied Optics* **45**(36), 9160-9167 (2006).
35. A. H. Al-Janabi, "Transportation of nanosecond laser pulses by hollow core photonic crystal fiber for laser ignition," *Laser Phys. Lett.* **2**, 529-531 (2005).
36. A. P. Yalin, M. Defoort, S. Joshi, D. B. Olsen, B. Willson, Y. Matsuura, and M. Miyagi, "Laser ignition of natural gas engines using fiber delivery," in *ASME ICE Division 2005 Fall Technical Conference*, (Ottawa, 2005).
37. R. K. Nubling and J. A. Harrington, "Launch conditions and mode coupling in hollow-glass waveguides," *opt. Eng.* **37**, 2454-2458 (1998).
38. A. Inberg, M. B. David, M. Oksman, A. Katzir, and N. Croitoru, "Theoretical model and experimental studies of infrared radiation propagation in hollow plastic and glass waveguides," *Opt. Eng.* **39**, 1316-1320 (2000).
39. Y. Matsuura, K. Hanamoto, S. Sato, and M. Miyagi, "Hollow-fiber delivery of high-power pulsed Nd:YAG laser light," *Opt. Lett.* **23**, 1858-1860 (1998).
40. J. D. Shephard, J. D. C. Jones, D. P. Hand, G. Bouwmans, J. C. Knight, P. S. J. Russell, and B. J. Mangan, "High energy nanosecond laser pulses delivered single-mode through hollow-core PBG fibers," *Opt. Exp.* **12**, 717-723 (2004).
41. S. O. Konorov, A. B. Fedotov, O. A. Kolevatova, V. I. Beloglazov, N. B. Skibina, A. V. Shcherbakov, E. Wintner, and A. M. Zheltikov, "Laser breakdown with millijoule trains of picosecond pulses transmitted through a hollow-core photonic-crystal fiber," *J. Phys. D.* **36**, 1375-1381 (2003).

42. A. Sircar, R. K. Dwivedi, and R. K. Thereja, "Laser induced Breakdown of Ar, N<sub>2</sub>, and O<sub>2</sub> gases using 1.064, 0.532, 0.35 and 0.266um radiation," Applied Physics B **63**, 623-627 (1996).

## Chapter 4

---

### **Development of a Multiplexed Fiber Delivered Laser Ignition System for Natural Gas Engines**

Past research has demonstrated the feasibility of using laser sparks for gas engine ignition, and has shown potential benefits associated with reduced cyclic variability, extension of the lean operating limit, reduced NO<sub>x</sub> emissions and increased engine efficiencies. This chapter details the design, bench-top testing and on-engine demonstration of a fiber-optic delivery system for ignition of natural gas engines. The system is designed for use on a Caterpillar G3516C engine and is comprised of a single neodymium yttrium aluminum garnet (Nd:YAG) laser as the energy source, a multiplexer to switch the laser beam between cylinders, hollow core fiber optics, and optical spark plugs to create sparks inside the cylinders. Design considerations for engine integration are introduced and preliminary results are presented.

## 4.1. Introduction

Laser ignition has been demonstrated as an effective ignition source for lean burn natural gas engines<sup>1-3</sup>. It has been shown that a spark in atmospheric air can be created if the optical density of focused laser beam is  $\sim 300 \text{ GW/cm}^2$ <sup>3-6</sup>. Moreover, elevated in-cylinder pressures in gas engines facilitate the formation of spark (threshold intensity requirement decreases with increasing pressure)<sup>7, 8</sup>. Most of the research on laser ignition for gas engines have employed open beam paths, i.e, the laser is directed to the cylinders in open air by a series of mirrors mounted in free space. This approach has inherent drawbacks including potential for misalignment, safety hazards, beam steering and lack of reliability etc. On the other hand, fiber delivered laser ignition systems have the potential to transport laser pulses to the engine cylinders in a safe and reliable manner with less susceptibility to the aforementioned problems. However, the use of fibers for laser spark delivery is technically challenging because of the need to delivery high power without damaging the fiber and preserving the quality ( $M^2$ )<sup>9</sup> of the beam to achieve the required threshold optical intensity for laser spark formation.

The early input from engine manufacturers associated with U.S. Department of Energy's (DOE) Advanced Reciprocating Engine System (ARES) program regarding the issues of safety, ease and reliability of laser ignition system have led this work to focus on development and demonstration of a practical fiber optic delivery system for laser ignition of gas engines. In Chapter 3, the potential of using hollow coated fibers and fiber lasers for successful spark delivery was shown. Yalin et al. demonstrated the first fiber optic laser ignition of a gas engine via a 1 m long coated hollow core fiber<sup>10</sup>. Tests were

performed on a single cylinder of an in-line six cylinder Waukesha VGF -18 engine with a nominal rating of 400 bhp continuous at 1800 rpm. Engine loading was achieved using a 1200 hp Midwest eddy current dynamometer. During the testing, the engine speed was limited to 1500 rpm and load was limited to 35% of rated load. Combustion pressure in each cylinder was measured using Hi-Techniques Win600 combustion analysis system. The laser ignition system was used to ignite just a single cylinder (No. 5) while the remaining cylinders were run with conventional spark ignition. The timing of ignition was kept at 14 degrees Before Top Dead Center (BTDC) for all the cylinders while the ignition timing for the laser ignited cylinder was retarded to 8 degrees BTDC. It was shown that even with retarded ignition timing for the laser ignited cylinder, its peak pressure was reached before all other cylinders indicating faster heat release rate. Calculated initial mass burn fraction duration (0-10% burn) of the methane-air mixture in the laser ignited cylinder showed comparatively shorter duration than the conventional ignited cylinders. The laser ignited cylinder was reported to have 100% firing and had one of the lowest coefficients of variation (COV) of peak pressure (~5.65%).

However, a practical laser ignition system should be able to ignite multiple cylinders with a single laser source. This chapter describes work that extends the abovementioned work on fiber optic laser ignition of a single cylinder of Waukesha engine towards a multiplexed laser ignition of a sixteen-cylinder Caterpillar G3516 C engine.

The layout of the chapter is as follows. In section 4.2 the multiplexer design and bench-top testing with 2 m long hollow core fiber optics is discussed. In section 4.3 the approach to overall system integration for an on-engine spark delivery system for two-cylinder laser ignition testing of a Caterpillar G3516C engine is discussed. In section 4.4,

preliminary results from the engine testing are presented. Finally, in section 4.5, conclusions and possibility of using the optical spark plugs for optical diagnostics are presented.

## 4.2. Multiplexer Design and Benchtop Testing

The use of fiber spark delivery (in contrast to, for example, using an individual laser mounted on each cylinder) affords the possibility of using a single laser source multiplexed via multiple fibers to multiple engine cylinders. In a past reference [11], a bench top experiment on using a mirror controlled by a galvanometer (or, galvo) to multiplex a laser beam was reported. The mirror was stepped through a series of positions with a continuous helium-neon (HeNe) laser beam being multiplexed to each stopped positions (“Step and hold” approach). As shown in the fig. 4.1, the continuous laser beam from the HeNe laser (on the bottom right corner of the figure) is multiplexed to six spots (shown by bright spots on the black portion of the paper) by a galvo (on the bottom left corner of the figure).

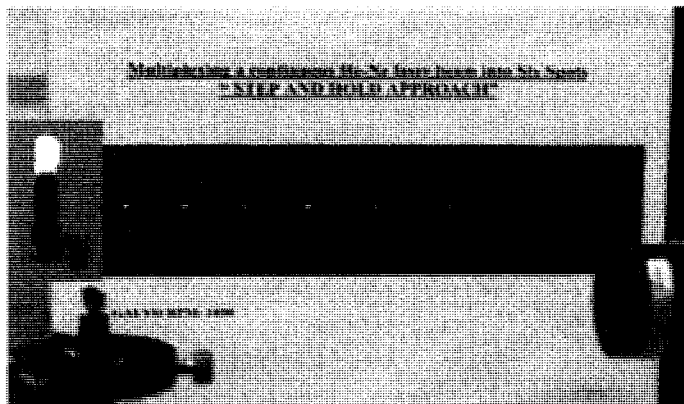


Figure 4.1: HeNe laser beam multiplexed into six spots using a galvo. The inset shows the galvo mirror. The faint line between the spots is due to continuous nature of the laser beam.

This experiment was followed by a bench top demonstration of multiplexed sparking through two 2 m long coated hollow core fibers. 100% sparking was observed at atmospheric air for these multiplexed fiber delivered sparks<sup>11</sup>.

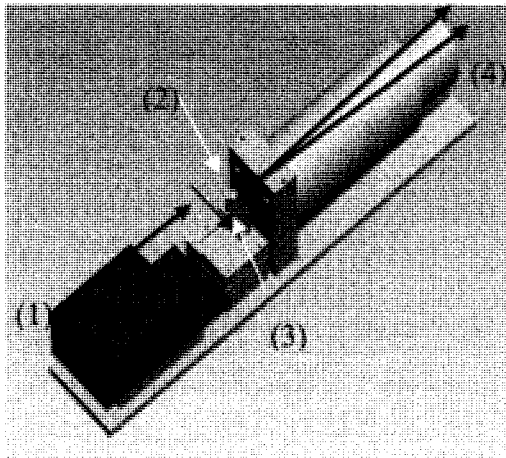


Figure 4.2: Modified multiplexer for use with a step-and-hold galvanometer. The beam (black arrows) comes from the laser (1) on the left and is turned by a fixed mirror (2), and encounters the galvanometer (3), which switches between fibers held in fiber holder (4). Black arrows show the path of the laser beam

---

Building on the past bench-top demonstrations<sup>11</sup>, a solid robust multiplexer was developed in collaboration with Woodward Industries, Fort Collins. Figure 4.2 shows a schematic of the Woodward multiplexer for this step-and-hold setup. The multiplexer components were made out of aluminum and attached to a reinforced aluminum base. The associated optical spark plugs were made out of stainless steel to ensure strength. Although the multiplexer was designed for eight fibers, i.e. for one bank of the Caterpillar G3516C engine, the current focus was on spark delivery through two fibers.

The choice of two-channels was to match the repetition rate of the laser that was used in the experiments, though it is emphasized that the multiplexer design would be essentially unchanged for additional channels and that higher repetition rate lasers are commercially available. The current setup employed one galvanometer. The optical spark-plugs designed for use on the engine is shown in Fig. 4.3.

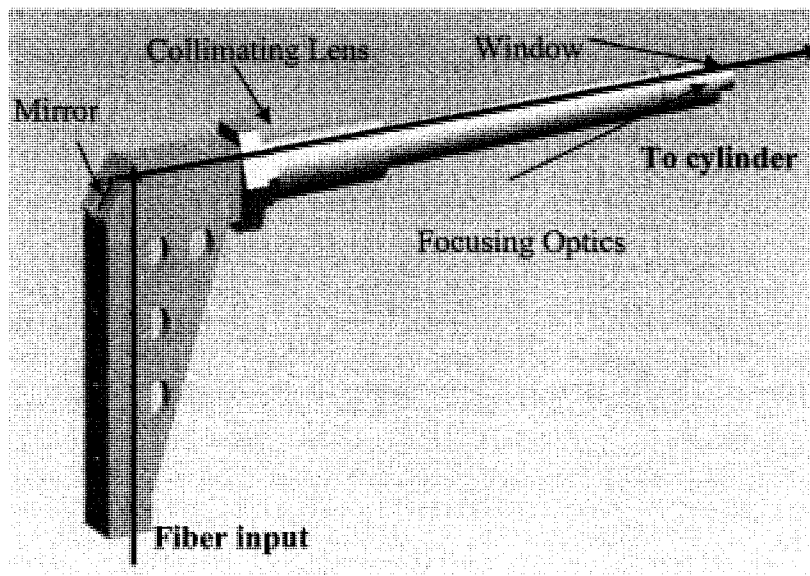


Figure 4.3: Optical spark plug. (Actual plug is vertical, not horizontal.) Barrel (shown at right) screws into the spark plug port on the cylinder. Arrows show laser beam path.

The spark plug consisted of suitable fiber holders and a coated mirror (held at 45 degree with respect to the fiber axis) which turned the laser beam from the fiber exit onto a collimating lens and a focusing lens assembly held at the end of the spark plug. The focusing lens assembly consisted of an uncoated focusing lens with focal length of 9mm and an uncoated 2.5 mm thick sapphire window chosen for its excellent mechanical and thermal properties. The clear aperture of the window was only 8 mm in diameter and was

dictated by the available space in the engine head. The end of the optical plug had suitable spark plug threads so that it could be screwed onto the engine head.

In order to characterize the multiplexer system, bench-top testing and characterization of energy transmission (throughput), beam quality, and reliability of sparking was conducted. Figure 4.4 shows various locations in the setup where energy measurements were conducted.

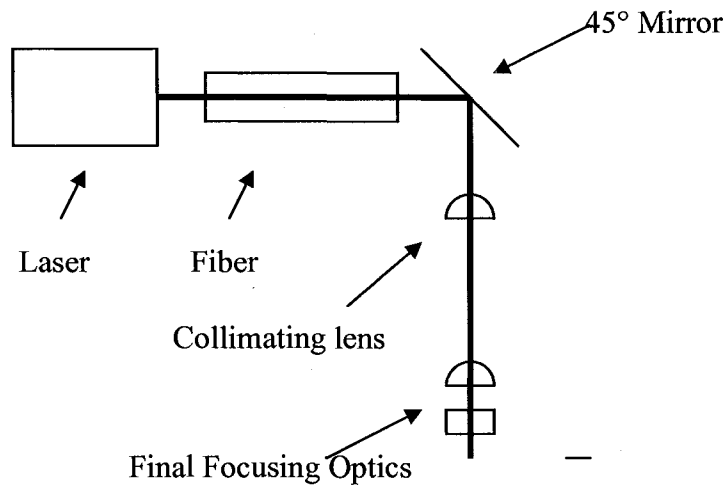


Figure 4.4: Schematic of optics used in optical plug. Numbers indicated positions used for measurements of energy transmission and loss. The solid black line indicates the laser beam.

---

To test for energy transmission (loss) through individual component, the central section of the multiplexer was removed, and the energy was measured with a power meter at a series of locations (indicated with numbers in Fig. 4.4. Measuring the energy before and after a given component allowed direct determination of the component's transmission. Table 4.1 shows the energy losses for the two channels including the

individual fibers, turning mirror, collimating lens and focusing optics. The losses for the fibers are between 10% and 20% which is consistent with earlier findings<sup>12</sup>. The losses through the optics are also consistent when losses are assumed to be ~4% at each surface for uncoated lens and window and ~2% at each surface for antireflection coated collimating lens. The total transmission is found as the product of transmission through each component (and is consistent with an overall in/out measurement), and the total percentage loss is found as 100% minus the transmission. With proper setup, energy throughput was found to be 86 - 88% (consistent with earlier findings).

Table 4.1: Measured transmission (%) for individual components of the multiplexer unit.

	<b>Fiber</b>	<b>Turning mirror and collimating lens</b>	<b>Focusing optics</b>	<b>Total transmission</b>	<b>Total loss</b>
<b>Channel 1</b>	83	96	85	68	32
<b>Channel 2</b>	87	96	79	66	34

To test for beam quality, calculations of the  $M^2$  of the beam was made by taking beam profiles with burn paper at 10 cm from the fiber end, and measuring the diameter of the beam from the burn paper. The  $M^2$  parameter was approximately determined as:

$$M^2 = \frac{w_0 \pi}{\lambda} \theta \quad (1)$$

where,  $w_0$  is the radius of the beam at the fiber output (in this case 0.5 mm),  $\lambda$  is the wavelength (1064 nm),  $\theta$  is the divergence of the beam exiting the fiber. The divergence of the beam for fibers 1 and 2 were measured to be approximately 0.0127 and 0.0104. This resulted in values of M2 of  $\sim 18$  and  $\sim 15$  for fibers 1 and 2 respectively, which matched our earlier results<sup>12</sup> and hence favored sparking at atmospheric pressure conditions.

The ability to spark was investigated by setting up the multiplexer on the bench with the two fibers enclosed by nylon tubing and going straight into the optical spark plugs. A vacuum was drawn through the entire system in order to reduce the chance of sparking on the optical fiber faces. A high pressure test chamber pressurized to 15 bar (roughly equivalent to the motored pressure at ignition timing of the Caterpillar G3516 C engine) was used to investigate the sparking. By direct observation, it was found that 100% sparking could be obtained when the energy was at sufficient level.

### **4.3. System Integration**

In this section engine integration issues for initial tests employing two-cylinder laser ignition of a 4-stroke Caterpillar G3516C series natural gas engine are presented. An approach for selecting the cylinders for laser ignition and some of the controls and vibration isolation systems that was developed during this work are discussed.

#### **4.3.1 Selection of Laser Ignited Cylinders**

As mentioned above, initial design was for two cylinders of a 4-stroke G3516C C engine that had two banks of 8 cylinders on each side, as shown schematically in Fig 4.4.

Note that the constraints were related to the relatively low repetition rate of our current laser (30Hz). Lasers with significantly higher repetition rates are available and would allow ignition of a full bank of the engine.

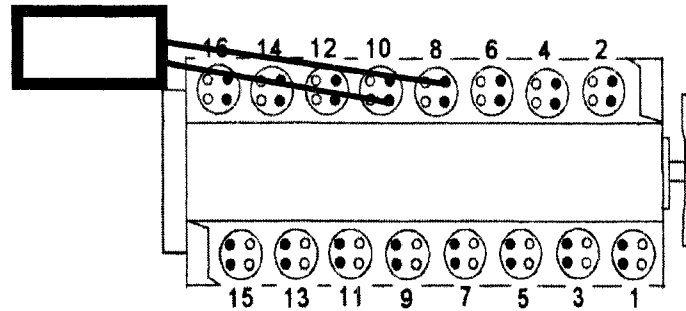


Figure 4.5: Diagram showing the engine from the top with the cylinders numbered. The box on the left shows the placement of the laser/multiplexer assembly, with the lines showing the fibers going to their respective cylinders. (Actual fibers have slight curvature.)

---

The selection of the two cylinders for testing was based on the following criteria:

1. Each cylinder needed to be sparked at 15Hz for the corresponding 1800 rpm of the engine. The maximum firing speed of the laser was 30 Hz sufficient for sparking of two cylinders that were opposite in the engine cycle.
2. The performance of end cylinders inherently differ from the middle cylinders in the engine due to various factors including mixing, poor fuel/air mixture distribution, jacket water cooling etc. Hence, two cylinders on the inside of the bank were preferred.

Given these constraints, cylinders 8 and 10 on the engine were chosen and instrumented with Kistler Pressure transducers. This allowed the mounting of the laser and multiplexer in a horizontal orientation for use with our right-angle optical

spark plugs (Fig.4.3), and would require relatively small curvature imposed on the fibers.

### 4.3.2 Vibration Isolation

The whole multiplexer system (including the laser) was isolated from the engine vibration. The multiplexer was therefore mounted on a rigid aluminum base-plate, which was isolated from engine vibration by a set of 4 air springs that could be inflated to a design height to work within an optimum region. These air springs provided a low enough spring constant such that the resonant frequency was much lower than the engine vibration frequency (30Hz) and its first half frequency (15Hz), thereby providing adequate vibration isolation. An additional set of 4 rubber dampers were also installed to provide some level of damping. This setup is shown in Fig. 4.6

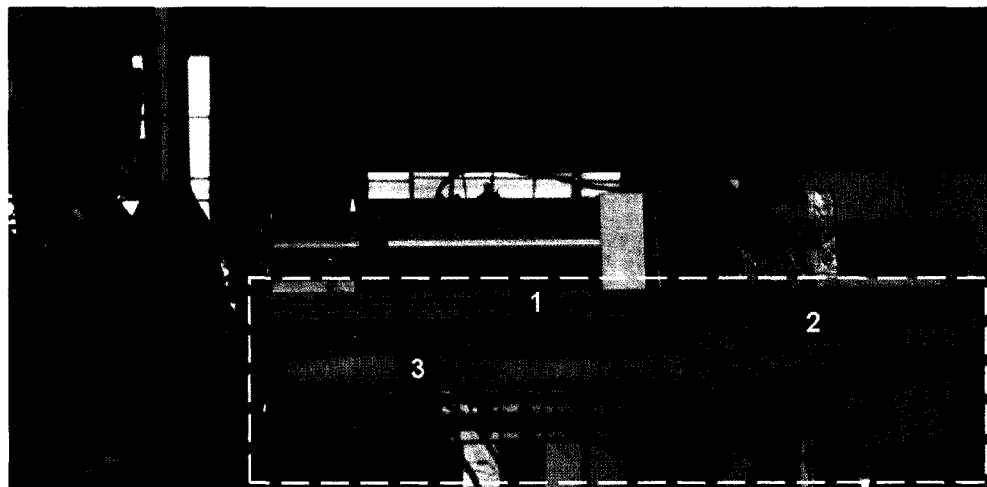


Figure 4.6: Vibration isolation setup. The multiplexer is attached to an aluminum base (1) which sits on air springs (2). The entire setup is fixed to a separate post (3).

---

Because of space limitation on the engine itself, the entire vibration damped multiplexer assembly was mounted on the engine skid. The assembly was placed in line with the first bank of 8 cylinders (in which the two cylinders reside as chosen above), with the fibers exiting the multiplexer parallel to the floor (with minimum amount of bending), and going to each of the two cylinders on the engine. The overall multiplexer system, as mounted on the engine, is shown in Fig. 4.7.

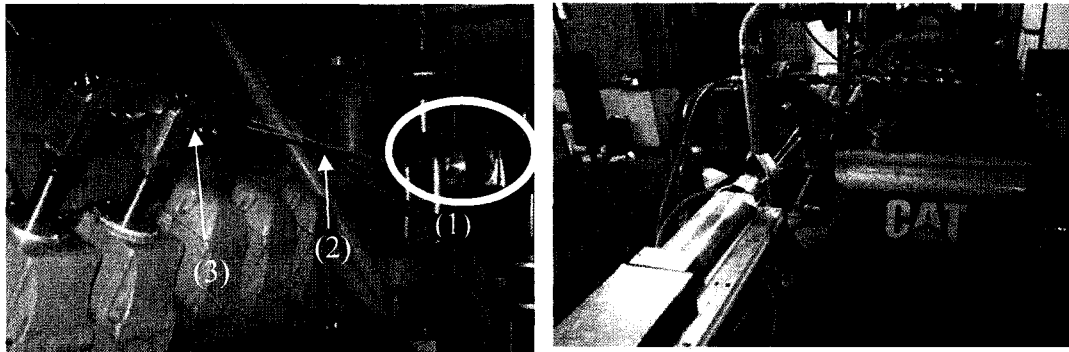


Figure 4.7: Multiplexer system for Caterpillar G3516 C engine. In the picture on the left, the multiplexer (1) is circled. Hollow core fibers are housed in the white nylon tubes, labeled (2). The output ends of the fibers are held in the spark plugs, labeled (3). The picture on the right is the view of multiplexer from another angle.

### 4.3.3 Multiplexer Control System

The laser and galvanometer in the multiplexer were both controlled by a custom LabView program. The program controlled the outputs on a digital acquisition card (DAQ), which triggered the laser and directed the galvanometer. The galvanometer received a voltage from -10 to 10V to control the mirror position and the laser received a

square wave pulse to control its firing time. The LabView program sent out the proper series of voltage pulses to the laser and galvanometer in time with the engine. In order to synchronize the LabView™ control program with the engine, a simple approach was taken. Triggers were taken from inductive sensors affixed to the ignition coil wires of the cylinders which fired immediately previous to the two laser ignited cylinders. These triggers, along with an input giving the engine speed at the time of the trigger, allowed the control program to calculate an approximate delay from which to fire the laser ignited cylinders. This approach allowed for a minimum of timing error during engine acceleration. Once the engine was at its operating speed of 1800rpm, the control program took the exact engine speed along with a once-per-rotation trigger pulse in order to calculate the delays required for firing the laser ignited cylinders. Note that the ultimate system would have the laser ignition control integrated into the main engine control software and the approach reported herein is just for demonstration purpose.

#### 4.4. Preliminary Engine Test Results

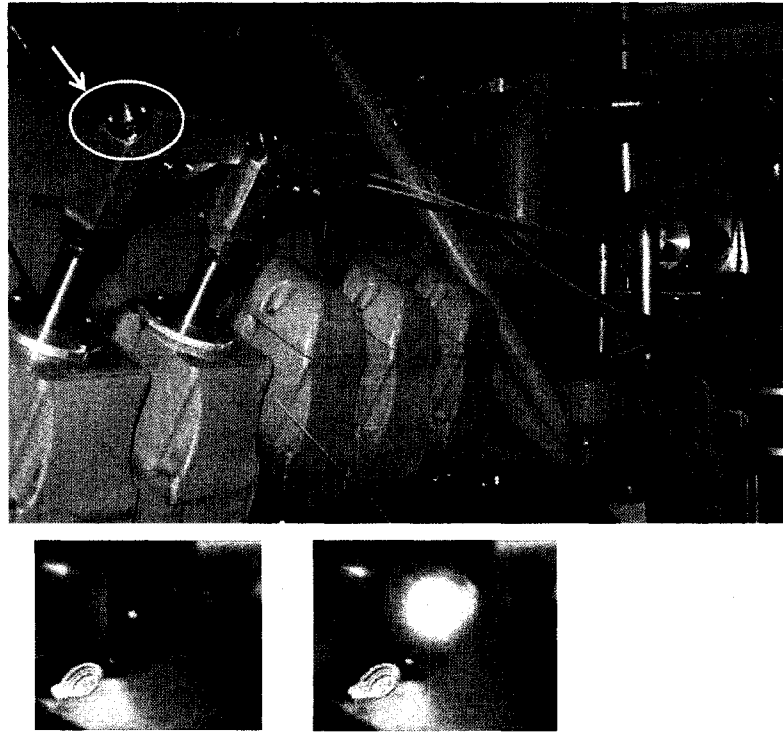


Figure 4.8: Laser spark (tiny white light) and subsequent combustion (bright white flash) are shown in the bottom left and right pictures respectively. The combustion is viewed through the mirror (marked with a white circle) in the optical spark plug as shown in the top picture.

---

Figure 4.8 shows the multiplexer setup on the engine. Initial demonstration of the multiplexer system on Caterpillar G3516 C engine was done at idle conditions (no load). Successful laser ignition was demonstrated for both targeted cylinders (Nos. 8 and 10).

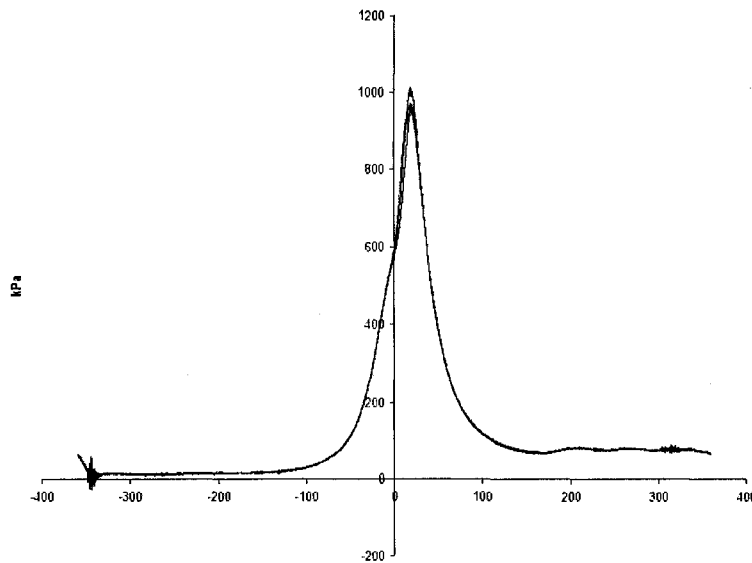


Figure 4.9: Pressure curves for laser ignited cylinder.

Spark formation and combustion were confirmed both visually (by taking photographs through the turning mirror of the plug into the cylinders) as well as by pressure traces as shown in Fig. 4.8 and Fig 4.9 respectively. In Fig.4.8, the spark formation (tiny white light) as well as the subsequent combustion (bright flash) in the combustion chamber can be seen. Fig 4.9 shows a typical pressure trace at idle condition (1100 rpm). Note that this demonstration was only for initial demonstration of the multiplexer. The ignition timing was set at 24 degrees before top dead center (BTDC). One can observe peak pressures of  $\sim 950 - 1000$  kPa few degrees after the top dead center (0 degrees in the Figure). The measured in-cylinder pressure at ignition timing was  $\sim 300$  kPa or, 3 bar less than the pressures tested in the optical cell. This suggested an ease in sparking inside engine cylinders due to impurities that are inherently present in the cylinder. However, the observed reliability in sparking was less than 100% (i.e, there

were misfires), owing to triggering and misalignment problems. But, this showed proof of principle operation of a multiplexed laser ignition system for natural gas engine. Furthermore, it also showed the potential of performing optical diagnostics through the turning mirror to monitor misfires as well as equivalence ratio monitoring.

## 4.5. Conclusions

This chapter is concerned with the design, development, and bench-top testing of a multiplexed laser ignition system appropriate for gas engine operation. The multiplexer employed a single laser source, a moving mirror based on a galvo, and two hollow core fibers to transmit laser pulses to two engine cylinders. The system was tested on the bench-top to measure energy losses and transmission measurements of the spark plug components. Total throughput for the two channels was measured to be around 66% and 68%. With these transmissions, reliable sparking was observed at 15 bar (in a pressure chamber) with focal intensities of  $\sim 100 \text{ GW/cm}^2$ . These test results demonstrate successful bench-top operation of the multiplexer at anticipated engine conditions. The multiplexer was tested for a dual-cylinder laser ignition of a Caterpillar G3516C engine and laser ignition of the two cylinders was confirmed. Operation with a larger number of cylinders would require a higher repetition rate laser (which is commercially available). Although 100% firing was not observed, the demonstration nonetheless showed a proof of principle operation of a multiplexer. Further development of the multiplexer system with accurate control of laser launch into the fiber optics is needed. The demonstration also showed the possibility of using the current configuration (the focusing optics and the turning mirror) to perform LIBS for monitoring equivalence ratio. This would be a value added component to the laser ignition.

## References

1. J. D. Dale, P. R. Smy, and R. M. Clements, "Laser ignited internal combustion engine-an experimental study," SAE (SAE Paper 780329), 1539-1548 (1979).
2. M. Weinrotter, H. Kopecek, M. Tesch, E. Wintner, M. Lackner, and F. Winter, "Laser ignition of ultra-lean methane/hydrogen/air mixtures at high temperature and pressure," *Exptl. Therm. and Fluid Sci.* **29**, 569-577 (2005).
3. G. Herdin, J. Klausner, E. Wintner, M. Weinrotter, and J. Graf, "Laser ignition-a new concept to use and increase the potentials of gas engines," in *ASME Internal Combustion Engine Division 2005 Fall Technical Conference*, (2005), pp. 1-9.
4. T. X. Phuoc and F.P.White, "Laser-Induced Spark Ignition of CH<sub>4</sub>/Air Mixtures," *Combustion and Flame* **119**, 203-216 (1999).
5. H. Kopecek, H. Maher, G. Reider, F. Winter, and W. E., "Laser ignition of methane-air mixtures at high pressures," *Exptl. Therm. and Fluid Sci.* **27**, 499-503 (2003).
6. I. C. E. Turcu, M. C. Gower, and P. Huntington, "Measurement of KrF laser breakdown threshold in gases," *Opt. Commun.* **134**, 66-68 (1997).
7. T. X. Phuoc, "Laser spark ignition: experimental determination of laser-induced breakdown thresholds of combustion gases," *Opt. Commun.* **175**, 419-423 (2000).
8. D. H. Gill and A. A. Dougal, "Breakdown minima due to electron-impact ionization in super-high-pressure gases irradiated by a focused giant -pulse laser," *Physical Review Letters* **15**(22), 845-847 (1965).
9. A. E. Siegman, "Output beam propagation and beam quality from a multimode stable cavity laser," *IEEE J. Quantum Electron* **29**, 1212-1217 (1993).
10. A. P. Yalin, M. Defoort, S. Joshi, D. B. Olsen, B. Willson, Y. Matsuura, and M. Miyagi, "Laser ignition of natural gas engines using fiber delivery," in *ASME ICE Division 2005 Fall Technical Conference*, (Ottawa, 2005).
11. A. P. Yalin, A. Reynolds, S. Joshi, M. Defoort, B. Willson, Y. Matsuura, and M. Miyagi, "Development of a fiber delivered laser ignition system for natural gas engines," in *ASME ICE Division 2006- Spring Technical Conference*, (Aachen, Germany, 2006).

12. A. P. Yalin, M. Defoort, B. Willson, Y. Matsuura, and M. Miyagi, "Use of hollow-core fibers to deliver nanosecond Nd:YAG laser pulses to form sparks in gases," *Optics Letters* **30**(16), 2083-2085 (2005)

## Chapter 5

---

# Laser Induced Breakdown Spectroscopy for In-Cylinder Equivalence Ratio Measurements in Laser Ignited Natural Gas Engines

In this chapter we present the simultaneous use of laser sparks for engine ignition and Laser Induced Breakdown Spectroscopy (LIBS) measurements of in-cylinder equivalence ratios. A 1064 nm neodymium yttrium aluminum garnet (Nd:YAG) laser beam is used with an optical spark plug to ignite a single cylinder natural gas engine. The optical emission from the combustion initiating laser spark is collected through the optical spark plug and cycle by cycle spectra are analyzed for  $H_{\alpha}$  (656 nm), O (777 nm) and N (742 nm, 744 nm and 746 nm) neutral atomic lines. The line area ratios of  $H_{\alpha}/O_{777}$ ,  $H_{\alpha}/N_{746}$  and  $H_{\alpha}/N_{tot}$  (where  $N_{tot}$  is the sum of areas of the aforementioned N lines) are correlated with equivalence ratios measured by a wide band Universal Exhaust Gas Oxygen sensor (UEGO). Experiments are performed for input laser energy levels of 21 mJ and 26 mJ, compression ratios of 9 and 11 and equivalence ratios between 0.6 to 0.95.

The results show a reasonable linear variation and linear correlation ( $R^2 > 0.99$ ) of line intensity ratio with equivalence ratio, thereby suggesting an engine diagnostic method for cylinder resolved equivalence ratio measurements.

## 5.1. Introduction

Laser ignition is viewed as a potential ignition technology for advanced high brake mean effective pressure (BMEP) megawatt class natural gas engines<sup>1-4</sup>. When a high peak power laser beam is tightly focused in a gaseous medium, a breakdown of the medium ensues and a combustion initiating plasma (spark) is formed. Typical breakdown intensities for the conditions of interest are  $\sim 100\text{-}300 \text{ GW/cm}^2$ <sup>5,6</sup>. The spark can be used for igniting combustible mixtures, for example within engine cylinders. Laser induced ignition is characteristically different from conventional spark ignition due to its different plasma characteristics such as higher initial temperature and pressure. These parameters can lead to elevated flame speeds at early times<sup>7</sup>. Laser ignition in natural gas engines has the potential to extend the lean limit in high bmeep engines, thereby leading to reduced nitrous oxides ( $\text{NO}_x$ ) and higher combustion efficiency<sup>1,8</sup>. Furthermore, in contrast to conventional spark ignition (where the voltage requirement, dielectric breakdown, and rate of spark plug erosion increase with pressure)<sup>1,9</sup>, laser ignition becomes easier at elevated pressures since the breakdown threshold intensity decreases<sup>10,11</sup>. The latter point is especially important for modern advanced engines having increasingly high in cylinder pressures at time of ignition.

A practical laser ignition system requires a clean optical window to the combustion chamber (engine cylinder in our case). There is evidence that high laser

fluence at the window can keep the optical access window clean of any soot produced during engine operation<sup>1</sup>. The mechanism of window cleaning has been attributed to high photon pressure forces and photophoretic forces (from the laser beam) that detach soot particles from the window<sup>12,13</sup>. Optical access to the engine cylinder provides new possibilities to monitor equivalence ratio, ignition performance and other useful diagnostic parameters on an individual cylinder basis. The present work incorporates Laser Induced Breakdown Spectroscopy (LIBS) to measure equivalence ratio in natural gas engines with simultaneous laser ignition. The impact of equivalence ratio on engine performance is well known. In particular, lean spark-ignition combustion strategies are commonly employed to reduce NO<sub>x</sub> in stationary large-bore natural gas engines<sup>14</sup>; however overly lean conditions, can result in degraded engine performance and higher misfire rates<sup>4</sup>. Consequently, it would be of great benefit to be able to operate each cycle at the optimum equivalence ratio, which could be facilitated with a feedback measurement that is fast enough to measure individual cycle equivalence ratios in the combustion region within the cylinder<sup>15</sup>. Currently, the equivalence ratio measurements in engines are made either by an oxygen sensor placed in the common exhaust or by using ion-sensing method that uses spark plugs. In addition to not being cylinder resolved, the equivalence ratio control using an oxygen sensor suffers from a significant amount of warm-up time and slow response times<sup>16</sup>. Although the ion-sensing method can provide cycle by cycle and cylinder resolved equivalence ratio measurements of the fuel/air mixtures, it still uses conventional electric spark plugs that are not suitable for operating high BMEP gas engines.

LIBS has been extensively used as an analytical tool to measure elemental composition of solids, liquids and gases<sup>17,18</sup>. The basic premise of LIBS is to monitor the light emitted from a laser spark formed by focusing a high peak power laser in the medium. During the early times of laser spark formation, the medium is broken down into a high temperature (peak temperature  $\geq 100,000$  K<sup>19-21</sup>) plasma consisting of its constituent atoms, ions and electrons which are excited to high energy states. As the plasma cools down, these atoms and ions relax to lower energy levels and in emit light in form of continuum and line emissions. The intensity of these emission lines can be used to deduce the elemental conditions of the environment in which the spark is formed.

LIBS has been used by several researchers to measure equivalence ratio in combustible mixtures<sup>22,23</sup>. Typically, the equivalence ratio ( $\Phi$ ) of methane and air mixtures is measured from the ratio of a hydrogen line (from methane) to an oxygen or nitrogen (from air) lines. Stavropoulos et al. used LIBS to determine local equivalence ratio in laminar premixed methane-air flames with  $H_{\alpha}$  and O atomic lines ratios<sup>24</sup>. Phuoc and White used simultaneous measurements of the  $H_{\alpha}$  line and O lines in order to correlate intensity ratios with equivalence ratio in non-reacting and reacting jets of methane and air<sup>23</sup>. They also measured the intensities of  $H_{\alpha}$  and O lines from methane and air mixtures in a high pressure optical cell and showed a linear correlation between intensity ratios and equivalence ratios for pressures ranging from 100 to 500 kPa<sup>22</sup>. Ferioli et al. conducted LIBS analysis of exhaust gas of an engine and correlated ratios of C/N lines and C/O lines to the equivalence ratios (from  $\Phi = 0.8$  to  $\Phi = 1.2$ ). The equivalence ratio was measured by a UEGO sensor installed in the exhaust manifold of a spark-ignited engine<sup>16</sup>.

Our primary interest is in natural gas, which consists primarily of methane. Previously, the coauthors of the present work collaborated to show that LIBS analysis performed on laser sparks delivered through a hollow core fiber<sup>25</sup> into ultra-lean methane-air mixtures produced a linear correlation between the  $H_{\alpha}$  and  $N_{\text{tot}}$  emission line ratio and the mixture equivalence ratio. Here,  $N_{\text{tot}}$  represents the total integrated area of three atomic nitrogen lines at 742, 744 and 746nm. The equivalence ratios were varied from  $\Phi = 0.1$  to 0.4 and the mixtures were maintained at atmospheric pressure.

In this study, laser sparks formed from the 1064 nm beam of a Nd:YAG laser were used to ignite a single cylinder variable compression ratio Cooperative Fuel Research (CFR) engine modified to operate with natural gas fuel, and the emission spectra from these ignition sparks were analyzed to determine relative concentration proportions of  $H_{\alpha}$ , N and O atoms from which equivalence ratio at the spark location could be inferred. The tests were performed at two energy levels and two compression ratios. To the best of our knowledge, this is the first demonstration of internal combustion engine laser spark ignition coupled with simultaneous LIBS analysis.

The layout of the chapter is as follows. In Section 5.2 the experimental setup to perform LIBS on a single cylinder CFR engine is discussed. The engine configuration, optical plug for laser ignition and LIBS are described. In Section 5.3 spectroscopic results are presented. Cycle resolved spectra as well as averaged spectra are shown and results from correlating the line intensity ratios with equivalence ratios are presented. The effects differing laser energy and compression ratio are studied. The variability in the observed line intensity ratios is examined and the factors that can cause observed fluctuations are discussed. Finally Section 5.4 of the chapter presents conclusions including an outlook on

practical diagnostic configurations for measuring in-cylinder equivalence ratios and monitoring engine misfires.

## 5.2. Experimental Setup

### 5.2.1 Overview

Figure 5.1a is an overall schematic diagram of the experimental setup. In summary, the CFR engine was laser ignited with an optical spark plug. The optical emission from the laser spark was then collected through the optical spark plug (window, spark focusing optics and the mirror) and focused into a fiber connected to a spectrometer. The light was dispersed by the spectrometer and imaged with an Intensified Charged Couple Device (ICCD) camera.

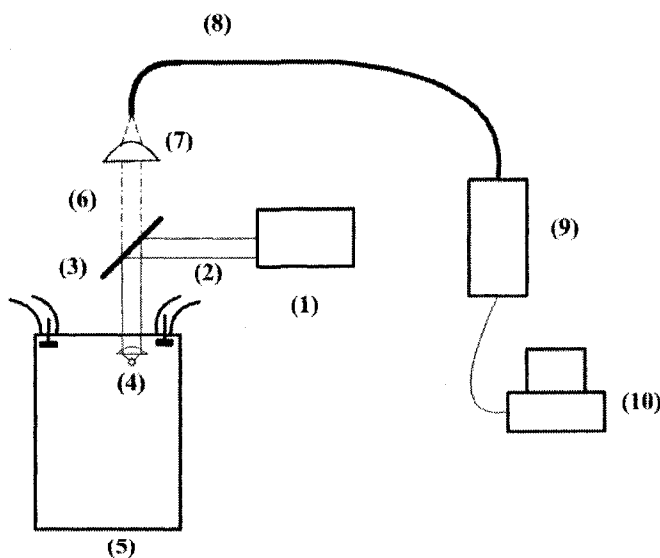


Figure 5.1a: Experimental Setup for laser ignition and LIBS. The labels indicate the following: (1)laser, (2) laser beam, (3) 45 degree mirror, (4) spark focusing optics, (5) CFR engine, (6) light emission from spark collected through the focusing optics and the mirror, (7) focusing lens, (8) optical fiber, (9) spectrometer/ICCD , (10) data acquisition device.

In Section 5.2.1 and 5.2.2, we discuss the engine setup for laser ignition and optical setup for collecting light to perform LIBS respectively. In Section 5.2.3, we discuss post-processing of the spectra to obtain intensity ratios and correlation of the intensity ratios with the measured equivalence ratios.

### **5.2.1 Engine Set up**

The engine used in this experiment was a variable compression single cylinder CFR engine designed for octane rating of gasoline fuel<sup>26</sup>. The engine was converted to run on gaseous fuels for measuring Methane Number (MN) of alternative fuels, for example natural gas and other blended fuels with varying concentrations of methane<sup>27</sup>. The CFR engine is loaded with a synchronous motor and has a nominal speed of 900 rpm.

The engine was equipped with a Kistler Pressure transducer to record individual cycle pressure traces. A wide band UEGO sensor was installed in the exhaust to monitor the equivalence ratio. The sensor was used to control an EGC-2 electronic carburetor that (approximately) fixed the desired equivalence ratio in the engine. In this work, high purity methane (99.99%) from high pressure cylinders was used as fuel. The engine was operated with compression ratios (CR) of 9 and 11 corresponding to measured in-cylinder pressures of 14 bar and 18 bar at time of ignition ( $15^\circ$  before top dead center (BTDC)) respectively.

## 5.2.2 Optical Setup

The optical spark plug used in this experiment was a custom made spark plug developed for fiber delivered laser ignition of G3516C caterpillar engine. Details on the spark plug can be found in our earlier paper [28]. This spark plug was modified so that a Big Sky Nd:YAG laser (1064 nm beam) was attached directly to it. This setup is shown in Fig 5.1b.

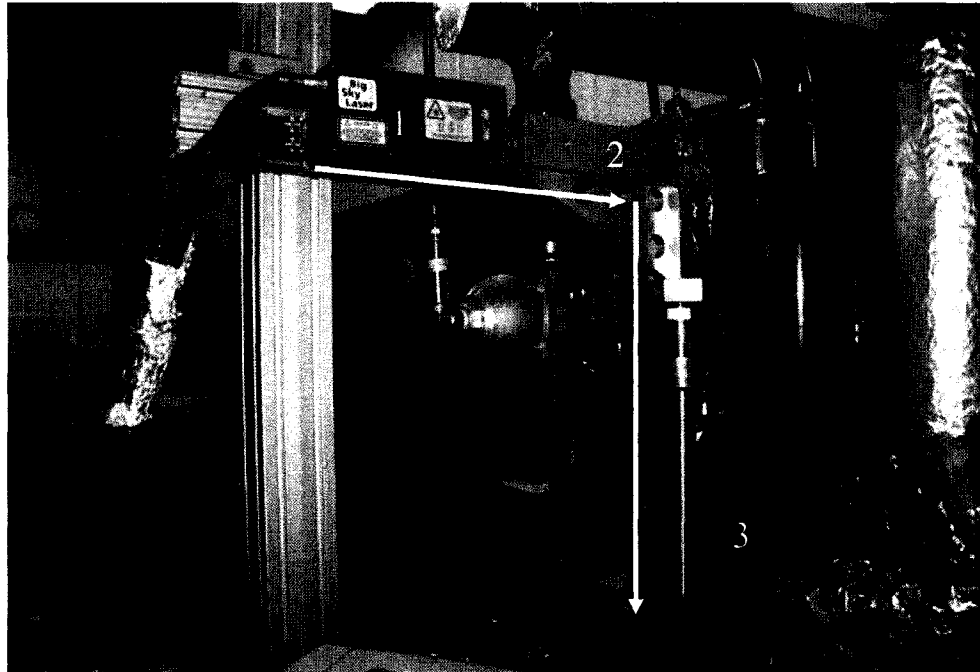


Figure 5.1b: Experimental Setup for laser ignition and LIBS on CFR engine. The white arrow indicates the laser beam from the Big Sky Nd:YAG laser to the spark plug . The labels indicate the following: (1) laser, (2) optical spark plug, and (3) CFR engine.

---

The laser beam has pulse duration of 8 ns. This configuration ensured that there was no open beam path between the laser and the engine in order to reduce any

misalignment or safety hazards. The optical spark plug houses a Nd:YAG high energy laser mirror (from CVI laser) at a forty five degree angle to the incoming laser beam. The mirror turns the laser beam ninety degrees downwards towards the focusing optics. The mirror reflects 1064 nm light while transmitting other wavelengths. The laser beam was focused inside the combustion chamber through a 2.5 mm thick sapphire window (9mm in diameter) by a 9 mm focal length plano-convex lens. The laser spark light emission was collected through the same focusing optics system and transmitted through the high energy laser mirror, after which it was focused by a 35 mm focal length lens into a 1 mm diameter fiber optic cable which transmitted the signal to a spectrometer (0.3 m Acton Spectra Pro 2300i). A 300 grooves/mm grating blazed at 750 nm dispersed the light in a spectral window from 646 nm to 783 nm and the output of the spectrometer was imaged by a Roper Scientific PI-MAX ICCD camera. The instrumental full width half maximum (FWHM) of the system was measured with a 543.5 nm helium-neon laser and found as 0.6 nm.

The laser was triggered at 15 Hz (corresponding to an engine speed of 900 rpm) by a signal obtained from an inductive pickup placed around the spark plug wire of the ignition coil. This signal corresponded to a timing of 15° BTDC of the engine. The ICCD camera exposure was triggered by the laser's Q-switch synchronization signal using a 1  $\mu$ s gate delay (from the laser spark onset) and a 5 $\mu$ s gate window. These values were not optimized and were chosen in order to get maximum light from the laser spark.

A relative intensity calibration was performed for the optical collection system (optical spark plug, optical fiber, spectrometer and camera) with a tungsten lamp (Ocean

Optics LS1-cal). The relative intensity calibration was applied to each individual LIBS spectrum.

### 5.2.3 Analysis of Spectra

Figure 5.2 illustrates a spectrum collected from a single laser spark for equivalence ratio of 0.6 at compression ratio of 11. Table 5.1 provides the atomic data for studied lines<sup>33</sup>. In the table,  $E_i$  and  $E_k$  correspond to higher and lower transition energy level and  $A_{ki}$  correspond to transition probability for the particular transition. The  $H_{\alpha}$ ,  $O_{715}$  and  $O_{777}$  atomic lines are clearly identifiable. The peaks of  $N_{742}$ ,  $N_{744}$  and  $N_{746}$  atomic lines are resolved but partially overlap due to instrumental broadening. No other identifiable peaks are visible in the spectral window from 646 nm to 783 nm in the figure. The Stark broadening of the atomic hydrogen line is apparent<sup>29</sup>.

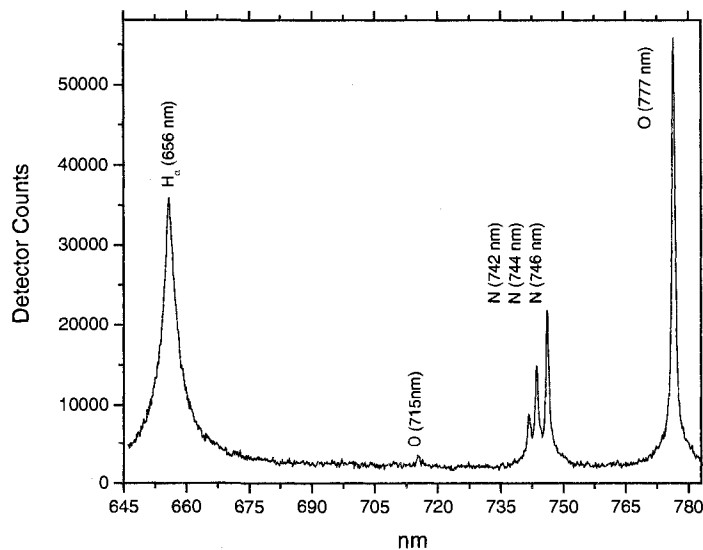


Figure 5.2: A single shot spectrum for  $\Phi = 0.6$  and CR = 11 at energy level of 21mJ

Table 5.1: Relevant atomic data for the observed spectral lines<sup>33</sup>.

Atomic lines	Wavelength (nm)	$E_i (\text{cm}^{-1}) - E_k (\text{cm}^{-1})$	$A_{ki} (\text{s}^{-1})$
H $_{\alpha}$	656.28	82,259.28 – 97,492.35	6.46e+07
O $_{715}$	715.67	102,662.02 – 116,631.09	5.05e+07
O $_{777}$	777.19	73,768.20 – 86,631.45	3.69e+07
O $_{777}$	777.41	73,768.20 – 86,627.77	3.69e+07
O $_{777}$	777.53	73,768.20 – 86,628.75	3.69e+07
N $_{742}$	742.36	83,284.07 – 96,750.84	5.95e+06
N $_{744}$	744.22	83,317.83 – 96,750.84	1.24e+07
N $_{746}$	746.83	83,364.62 – 96,750.84	1.93e+07

In order to ensure a good statistical sample, a set of 300 individual spectra were collected at each measurement condition and averaged. The averaged spectrum was then post-processed using PEAKFIT<sup>TM</sup> software. Areas of H $_{\alpha}$ , N $_{742}$ , N $_{744}$ , N $_{746}$  and O $_{777}$  atomic lines were determined from fitted Voigt profiles. The areas of the three N atomic lines were added together to obtain a single value for N emission and denoted by N $_{\text{tot}}$ . The line areas were used to obtain ratios of H $_{\alpha}$ /O $_{777}$ , H $_{\alpha}$ /N $_{746}$  and H $_{\alpha}$ /N $_{\text{tot}}$ , and the line intensity ratios were correlated with the (average) equivalence ratio measured by the UEGO sensor.

## 5.3. Results and Discussion

### 5.3.1 Overview

In this section, we present results of correlating LIBS line intensity ratios with equivalence ratios. The effect of change in compression ratio and laser energy level on the line intensity ratio is discussed. The variability in the data is presented and we discuss the different factors that play a role in introducing variability in the data.

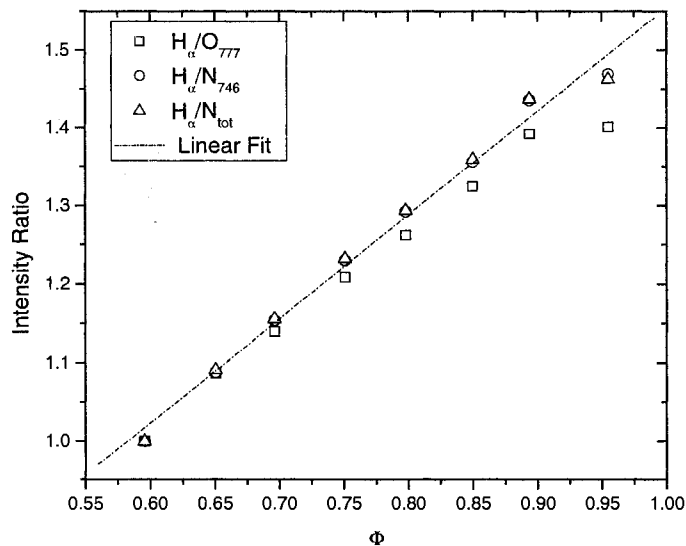


Figure 5.3: LIBS intensity ratio plotted against equivalence ratio ( $\Phi$ ) at CR =11 and input laser energy of 21mJ (data points are normalized to the initial value at  $\Phi =0.6$ ). Linear fit ( $R^2 > 0.99$ ) is to  $H_{\alpha}/N_{tot}$  ratios.

Figure 5.3 illustrates an example of the line intensity ratios for  $H_{\alpha}/N_{746}$ ,  $H_{\alpha}/N_{tot}$  and  $H_{\alpha}/O_{777}$  plotted against the equivalence ratio at CR of 11 and input laser energy (E) of

21 mJ. The ratios for each line intensity combination (i.e,  $H_{\alpha}/N_{746}$ ,  $H_{\alpha}/N_{tot}$  and  $H_{\alpha}/O_{777}$ ) are normalized by the corresponding intensity ratio at equivalence ratio of 0.6. The data points in Fig. 5.3 shows good linearity of line intensity ratios with equivalence ratios (fit coefficient  $R^2 > 0.99$ ). The linear fit shown in Fig. 3 is a fit only to the  $H/N_{tot}$  ratios. Fits to intensity ratios of  $H_{\alpha}/O_{777}$  and  $H_{\alpha}/N_{746}$  also show good linearity with fit coefficient ( $R^2$ ) greater than 0.99. The measured slope of the normalized fits for  $H_{\alpha}/N_{tot}$  (and  $H_{\alpha}/N_{746}$ ) and  $H_{\alpha}/O_{777}$  are  $1.33 \pm 0.22$  and  $1.64 \pm 0.20$  respectively. Hence, within measurement errors, the intensity ratios vary in the same proportion with increase in equivalence ratio irrespective of the choice of the atomic lines. This behavior is also observed for all energy levels and compression ratios. The observed non-zero slope of the intensity ratios with respect to equivalence ratios provide a diagnostic means to infer cylinder resolved in-cylinder equivalence ratios.

The linear increase in intensity ratios with equivalence ratio can be understood from Fig. 5.4 which shows integrated line intensities for  $H_{\alpha}$ ,  $O_{777}$  and  $N_{tot}$  plotted against equivalence ratio ( $\Phi$ ). As  $\Phi$  is increased, there is a corresponding linear increase (fit coefficient  $R^2 > 0.99$ ) in the line intensities for  $H_{\alpha}$  and a linear decrease in line intensities of  $O_{777}$  and  $N_{tot}$ . This is expected, because as equivalence ratio is increased, the proportion of methane (and hence hydrogen) with respect to air (oxygen and nitrogen) increases. In a simple analysis that neglects, for example, quenching variations, one expects proportionality between the emission signals and species concentration<sup>30</sup>.

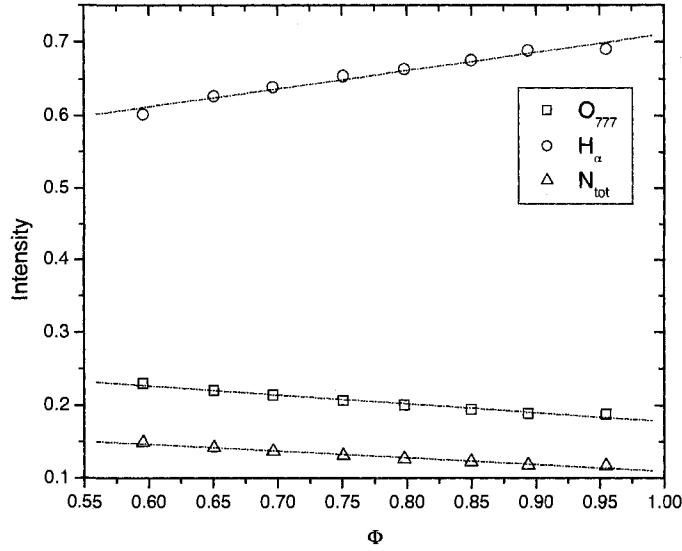


Figure 5.4: Integrated LIBS signal for  $H_{\alpha}$ ,  $O_{777}$  and  $N_{tot}$  plotted against equivalence ratio ( $\Phi$ ) at a CR = 9 and E = 26mJ. Linear fits ( $R^2 > 0.99$ ) are shown for each line ratio combination.

One can also observe in Fig.5.3 that the line intensity ratios for  $H_{\alpha}/N_{746}$  (circles) and  $H_{\alpha}/N_{tot}$  (triangles) overlap with each other for all equivalence ratios. This shows that line areas of  $N_{746}$  and  $N_{tot}$  vary in the same proportion for all equivalence ratios and hence  $H_{\alpha}/N_{tot}$  can be used equivalent to  $H_{\alpha}/N_{746}$  which is desirable since it is practically easier to use the entire (sometimes overlapping) optical emission from the three N lines. The similar behavior of the three N lines is expected since they are due to fine structure of the same transitions and have very similar energy levels<sup>31</sup>. In the rest of the section, we consider only line intensity ratios of  $H_{\alpha}/O_{777}$  and  $H_{\alpha}/N_{tot}$ .

### 5.3.2 Effect of Compression Ratios and Laser Energy

Figure 5.5 shows line intensity ratios of  $H_\alpha/O_{777}$  and  $H_\alpha/N_{tot}$  plotted against equivalence ratio for compression ratios of 9 and 11 at constant laser pulse energy of 21 mJ.

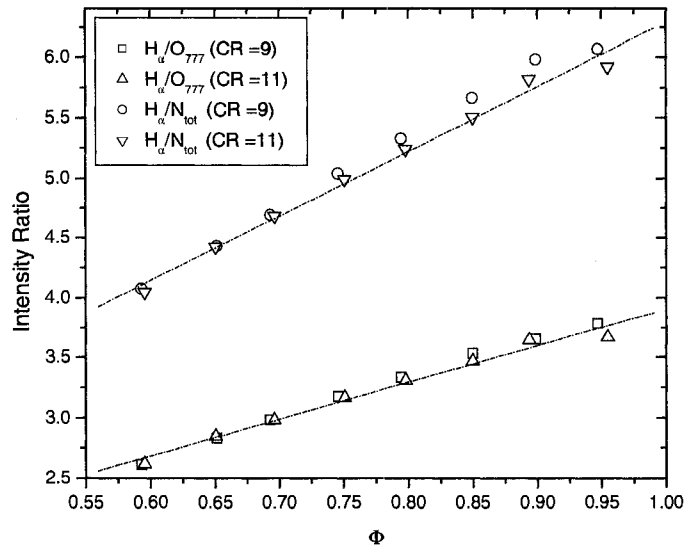


Figure 5.5: Line intensity ratios of  $H_\alpha/O_{777}$  and  $H_\alpha/N_{tot}$  plotted against equivalence ratio ( $\Phi$ ) at input energy level of 21 mJ. Linear fits are to  $H_\alpha/N_{tot}$  ratios.

A linear variation of intensity ratio with equivalence ratio is observed for these two cases and all other measured laser energy cases (with fit coefficient of  $R^2 > 0.99$ ). Within the measurement errors, no change in the line intensity ratios is observed as the compression ratio is increased from 9 to 11. This is also representative for input energy level of 26 mJ. This is consistent with the findings from our separate work on laser spark plasma characterization at high ambient pressures. It was observed that as the ambient pressure was increased, the spark plasma temperature and electron number density at later times of

spark plasma evolution became comparable at higher pressures (above 10 bar) suggesting relatively less effect of pressure on the atomic line intensities and hence on the line intensity ratios. Results from Phuoc's work on the dependence of line intensity ratio of  $H_{\alpha}/O_{777}$  on pressure also suggest a similar behavior<sup>22</sup>; although the ambient pressures in his work are relatively low (at 1 bar, 2 bar and 3 bar) than the motored in cylinder pressures in our work (14 bar and 18 bar).

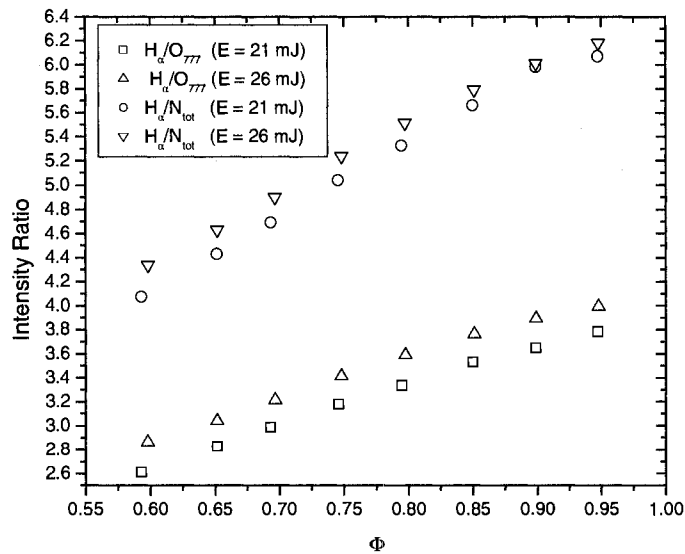


Figure 5.6: Line intensity ratios of  $H_{\alpha}/O_{777}$  and  $H_{\alpha}/N_{tot}$  plotted against equivalence ratio ( $\Phi$ ) at CR = 9.

We also examined the dependence of  $H_{\alpha}/O_{777}$  and  $H_{\alpha}/N_{tot}$  line intensity ratios for two different laser pulse energies of 21mJ and 26mJ. As illustrated in Fig.5.6, the line intensity ratios increased at all equivalence ratios when the laser pulse energy was increased from 21mJ to 26mJ at a compression ratio of 9. The increase in ratios is primarily due to increase in  $H_{\alpha}$ , which is attributed to different spark plasma conditions

(pressure and temperature) as the laser energy is changed. Nonetheless, the linear dependence of the intensity ratios for the equivalence ratios is maintained (over the measured range of laser energies and compression ratios).

### **5.3.3 Signal to Noise and Variability**

The viability of using a LIBS approach for equivalence ratio measurement requires the ability to precisely and accurately measure equivalence ratio for a given fuel air mixture. For example, an ideal homogenous fuel air mixture (with a fixed equivalence ratio) should provide a consistent line intensity ratio at all measurement times. In this work, we have shown a strong linear (non-zero slope) correlation between the measured equivalence ratios and the intensity ratios and hence we believe that in-cylinder LIBS can be used to measure equivalence ratios. However for practical application, the level of precision (based on the uncertainty observed in the measured intensity ratios for a given equivalence ratio) should also be considered.

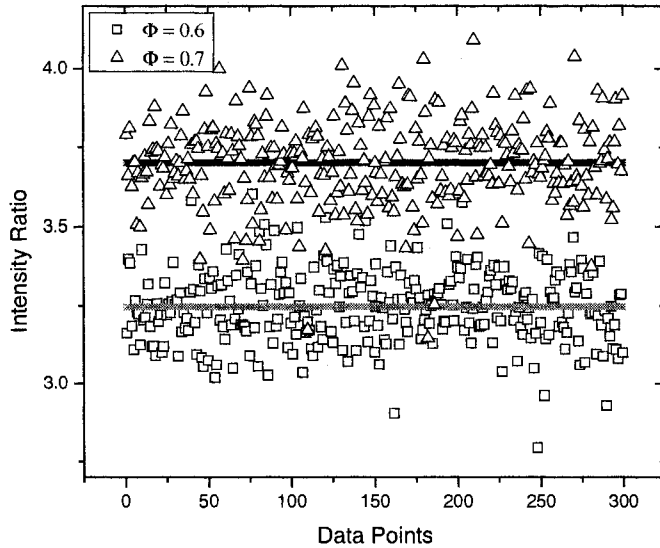


Figure 5.7: Single shot line intensity ratios of  $H_{\alpha}/O_{777}$  for  $\Phi = 0.6$  and  $\Phi = 0.7$  at CR = 11. Solid lines are the average values of intensity ratios.

---

Figure 5.7 shows the line intensity ratios of  $H_{\alpha}/O_{777}$  plotted for equivalence ratios of 0.6 and 0.7. Relative uncertainty in the ratios of  $H_{\alpha}/O_{777}$  and  $H_{\alpha}/N_{tot}$  was approximately 7% of the mean (based on  $1.96 \times$  Standard Deviation, using individual spectra). Correspondingly, for single shot measurements, the line ratios of  $H_{\alpha}/O_{777}$  allow determination of  $\Phi$  at 0.6 to within  $\sim 9\%$  relative uncertainty. Equivalently, for  $\sim 99\%$  precision in  $\Phi$ , allowable relative uncertainty in  $\Phi$  at 0.6 can be only 0.75%. As discussed below, the observed variations in intensity ratios are viewed to be real (as opposed to experimental error) and are thought to be related to inadequate mixing of our configuration, so that in a better mixed engine precision could be better. The equivalence ratio is measured by a UEGO sensor installed in the exhaust pipe, which measures the

equivalence ratio based on several factors such as exhaust composition, sensitivity of the sensor to various constituents in the exhaust, percentage of oxygen in the air etc. The measured equivalence ratios correspond to the overall average equivalence ratio of the fuel/air mixture in the cylinder; however, the LIBS measurement is localized at the spark location inside the cylinder at a given time.

In our experiment, there are various factors that can contribute to the observed fluctuation (variability) in intensity ratios - i) fluctuation in the overall equivalence ratio (which is nominally constant but can vary), ii) signal to noise (S/N) ratio of spectra, iii) probabilistic nature of the laser spark, iv) vibration, and v) fluctuation in the local equivalence ratio of the fuel/air mixture inside the cylinder.

The relative uncertainty in the measured equivalence ratio by the UEGO sensor was approximately 2%. No correlation was observed between uncertainty (extent of fluctuation) in equivalence ratio and line intensity ratios, so, we do not believe that fluctuations in the overall equivalence ratio are the dominant factor in the observed variation in the line intensity ratios.

In order to estimate the effect of noise in the spectra on the variability in the intensity ratios, signal to noise ratio for H $\alpha$ , N (742, 744 and 746nm) and O $_{777}$  lines were calculated. For each line contribution, the S/N was calculated as the ratio of the line area to the noise in the line area estimated as the product of standard deviation of the baseline multiplied by the extent of the spectral window). For all compression ratios and laser energy levels, S/N for all the atomic lines were too high (greater than 10,000) to have a significant effect on the variability observed in the line intensity ratios.

Laser induced breakdown of a medium itself is a stochastic process in nature. Hence, there exists shot to shot fluctuation in the overall light emitted by the plasma<sup>32</sup>. Fluctuations in emitted line intensities are best examined with laser sparks formed in constant environments. For example, our work on characterizing laser plasmas in high pressure air shows average shot to shot fluctuation in individual line signal intensity of approximately 1% at 21 bar (with maximum fluctuation as high as 6%). However, these fluctuations tend to similarly affect individual lines so that typical fluctuation in line intensity ratios (e.g.  $O_{777}/N_{tot}$ ) is only  $\sim 0.01\%$  (for 300 laser shots).

We do not believe that the observed fluctuations in the intensity ratios are due to the vibration associated with running the engine. Vibration can lead to misalignment of the laser beam with respect to the focusing optics and hence can result in a change in the focal spark volume. Engine vibration can also lead to misalignment of the light collection optics; however this misalignment affects the overall transmission of the light signal at all wavelengths proportionally and hence will not affect the line intensity ratios. Given the experimental setup, the change in the focal spark volume due to vibration could not be measured. However, 100% ignition was observed at all times during the experiment which might suggest relatively small change in the focal spark volume due to vibration.

Based on the above discussion, we posit that the observed variability in the line intensity ratios for equivalence ratio measurements might be due to the variability in equivalence ratio of the fuel air mixture in the local focal spark volume which is expected in a CFR engine. No other independent technique was employed to verify this inhomogeneity in fuel/air mixture inside the CFR cylinder.

## 5.4. Conclusions

Laser ignition is viewed as a potential ignition technology for advanced gas engines. Such engines are trending towards high BMEP and lean operation conditions favoring laser ignition. Laser ignition provides an opportunity to perform optical diagnostics such as equivalence ratio measurement. In this work, we have reported on simultaneous laser ignition of a single cylinder CFR natural gas engine and equivalence ratio measurement by LIBS. A linear dependence (and non-zero slope) was observed between the LIBS signal ratios of  $H\alpha/O_{777}$  and  $H\alpha/N_{tot}$  with equivalence ratio thereby showing a proof of principle for simultaneous laser ignition of gas engines and LIBS to monitor in-cylinder equivalence ratios.

A discussion on the variability on the LIBS signals ratios and the measured equivalence ratio was presented. The observed variability in the intensity ratios is thought to primarily result from fluctuation in the in-cylinder equivalence ratio due to inhomogeneous mixing. Further experiments are needed to better understand the observed variability. Nonetheless, the current configuration allows in-situ monitoring of in-cylinder equivalence ratios. A calibration chart would be needed in which LIBS signal ratios are correlated with equivalence ratios. Such data could be obtained using pre metered fuel-air mixtures combusted in a high pressure combustion test cell.

## References

1. G. Herdin, J. Klausner, E. Wintner, M. Weinrotter, and J. Graf, "Laser ignition-a new concept to use and increase the potentials of gas engines," in *ASME Internal Combustion Engine Division 2005 Fall Technical Conference*, (2005), pp. 1-9.
2. J. D. Dale, P. R. Smy, and R. M. Clements, "Laser ignited internal combustion engine-an experimental study," SAE (SAE Paper 780329), 1539-1548 (1979).
3. A. P. Yalin, M. Defoort, S. Joshi, D. B. Olsen, B. Willson, Y. Matsuura, and M. Miyagi, "Laser ignition of natural gas engines using fiber delivery," in *ASME ICE Division 2005 Fall Technical Conference*, (Ottawa, 2005).
4. H. Kopecek, S. Charareh, M. Lackner, C. Forsich, F. Winter, J. Kausner, G. Herdin, and E. Wintner, "Laser Ignition of Methane-Air Mixtures at High Pressure and Diagnostics," *Jnl. of Eng. for Gas Turb. and Power* **127**, 213-219 (2005).
5. I. C. E. Turcu, M. C. Gower, and P. Huntington, "Measurement of KrF laser breakdown threshold in gases," *Opt. Commun.* **134**, 66-68 (1997).
6. J. P. Davis, A. L. Smith, C. Giranda, and M. Squicciarini, "Laser-induced plasma formation in Xe, Ar, N<sub>2</sub>, and O<sub>2</sub> at the first four Nd:YAG harmonics," *Applied Optics* **30**, 4358-4364 (1991).
7. D. Bradley, C. G. W. Sheppard, I. M. Suardjaja, and R. Wooley, "Fundamentals of high-energy spark ignition with lasers," *Combustion and Flame* **138**, 55-77 (2004).
8. J. D. Dale, M. D. Checkel, and P. R. Smy, "Application of high energy ignition systems to engines," *Prog. Energy Comb. Sci.* **23**, 379-398 (1997).
9. A. P. Yalin, M. Defoort, B. Willson, Y. Matsuura, and M. Miyagi, "Use of hollow-core fibers to deliver nanosecond Nd:YAG laser pulses to form sparks in gases," *Optics Letters* **30**(16), 2083-2085 (2005).
10. T. X. Phuoc, "Laser spark ignition: experimental determination of laser-induced breakdown thresholds of combustion gases," *Opt. Commun.* **175**, 419-423 (2000).
11. D. H. Gill and A. A. Dougal, "Breakdown minima due to electron-impact ionization in super-high-pressure gases irradiated by a focused giant -pulse laser," *Physical Review Letters* **15**(22), 845-847 (1965).
12. T. X. Phuoc, "A comparative study of the photon pressure force, the photophoretic force, and the adhesion van der Wals force," *Opt. Commun.* **245**, 27-35 (2005).

13. H. Ranner, P. K. Tewari, H. Kofler, M. Lackner, E. Wintner, A. K. Agarwal, and F. Winter, "Laser cleaning of optical windows in internal combustion engines," *Optical Engineering* **46**(10), 1-8 (2007).
14. J. B. Heywood, *Internal Combustion Engine Fundamentals* (1988).
15. H. M. Cho and B.-Q. He, "Spark ignition natural gas engines - A review," *Energy Conversion and Management* **48**, 608-618 (2007).
16. F. Ferioli, P. V. Puzinauskas, and S. G. Buckley, "Laser-Induced Breakdown Spectroscopy for On-Line Engine Equivalence Ratio Measurements," *Applied Spectroscopy* **57**(9), 1183-1189 (2003).
17. D. A. Cremers and L. J. Radziemski, *Handbook of laser-induced breakdown spectroscopy* (John Wiley, Chichester, England; Hoboken, NJ, 2006), pp. xviii, 283 p., [210] p. of plates.
18. V. Sturm and R. Noll, "Laser-induced breakdown spectroscopy of gas mixtures of air, CO<sub>2</sub>, N<sub>2</sub> and C<sub>3</sub>H<sub>8</sub> for simultaneous C, H, O, and N measurement," *Applied Optics* **42**(30), 6221-6225 (2003).
19. Christian G. Parigger, David H. Plemmons, and E. Oks, "Balmer series H measurements in a laser-induced hydrogen plasma," *Applied Optics* **42**(30), 5992-6000 (2003).
20. S. Yalcin, D. R. Crosley, G. P. Smith, and G. W. Faris, "Influence of ambient conditions on the laser air spark," *Appl. Phys. B* **68**, 121-130 (1999).
21. N. Glumac and G. Elliott, "The effect of ambient pressure on laser-induced plasmas in air," *Optics and Lasers in Engineering* **45**, 27-35 (2007).
22. T. X. Phuoc, "Laser-induced spark for simultaneous ignition and fuel-to-air ratio measurements," *Optics and Lasers in Engineering*, **44**, 520-534 (2006).
23. T. X. Phuoc and F. P. White, "Laser-induced spark for measurements of the fuel-to-air ratio of a combustible mixture," *Fuel* **81**, 1761-1765 (2002).
24. P. Stavropoulos, A. Michalakou, G. Skevis, and S. Couris, "Laser-induced breakdown spectroscopy as an analytical tool for equivalence ratio measurement in methane-air premixed flames," *Spectrochimica Acta part B* **60**, 1092-1097 (2005).
25. C. Dumitrescu, P. V. Puzinauskas, S. Olcmen, S. G. Buckley, S. Joshi, and A. P. Yalin, "Fiber-Optic Spark Delivery for Gas-Phase Laser-Induced Breakdown Spectroscopy," *Applied Spectroscopy* **61**(12)(2007).
26. S. O. B. Shrestha and G. A. Karim, "The Operational Mixture Limits in Engines Fueled with Alternative Gaseous Fuels," *Journal of Energy Resources Technology* **128**, 223-228 (2006).
27. M. Malenshek, B. Wilson, and D. B. Olsen, "Assessment of Knock Characteristics of Alternative Gas Fuels through Methane Number Measurement," in *Gas Machinery Conference*, (Albuquerque, NM, 2008).

28. A. P. Yalin, S. Joshi, M. Defoort, and B. Willson, "Towards Multiplexed Fiber Delivered Laser Ignition for Natural Gas Engines," *J. Eng. Gas Turbines Power* **130**(4), 044502 (044504 pages) (2008).
29. E. Oks, *Stark Broadening of Hydrogen and Hydrogenlike Spectral Lines in Plasmas* (Alpha Science International Ltd., 2006).
30. T. X. Phuoc, "An experimental and numerical study of laser-induced spark in air," *Opt. and Lasers in Eng.* **43**(113-129)(2005).
31. NIST, "Atomic Spectra database," <http://physics.nist.gov>.
32. A. Borghese and S. S. Merola, "Time-resolved spectral and spatial description of laser-induced breakdown in air as a pulsed, bright, and broadband ultraviolet - visible light source," *Applied Optics* **37**(18), 3977-3983 (1998).

# Chapter 6

---

## Conclusions and Future work

Emission and efficiency benefits of laser ignited lean burn gas engines have been shown by many researchers. Furthermore, laser ignition inherently provides an optical access to engine cylinder to perform laser induced breakdown spectroscopy (LIBS) to monitor equivalence ratio of the fuel-air mixture inside the engine cylinder. However, the use of laser ignition in industrial environment has been limited due to a lack of practical robust laser ignition systems. This dissertation has described the initial steps taken towards the development of a practical fiber delivered laser ignition system and potential optical diagnostics capability of laser ignition systems.

Since laser spark formation in gas engines (or gas turbines) occurs at high pressures, it was required to undertake a series of experiments to understand the plasma environment at high pressures. Spectroscopic investigations were conducted to measure plasma temperature and electron number density at pressures ranging from 0.85 bar to 48.3 bar. Plasma temperature and electron density at later times of plasma evolution ( $\sim 1$   $\mu$ s) were found to be high ( $\sim 10,000$  K) and comparable for all high pressures. This little

variability in the plasma environment suggested a relatively little effect of any in-cylinder pressure fluctuations on LIBS measurement for monitoring equivalence ratios. The knowledge of these plasma environments are critical to assess the early flame development and subsequent combustion. A potential future research could be directed towards using these measured results into existing theoretical models such as blast wave theory to understand the plasma evolution at high pressures.

A major portion of the work was focused on characterizing commercially available optical fibers for delivering laser spark. A figure of merit (FOM) approach was utilized to compare suitability of different fibers for laser spark delivery. Transmission characteristics of 2-m long hollow core fibers (suitable for practical laser ignition system), Photonic Crystal Fibers (PCFs) and solid core fibers were experimentally investigated. A 35  $\mu\text{m}$  core diameter PCF was shown to deliver the highest level of output energy ( $\sim 0.55$  mJ), suitable for ignition of stoichiometric mixtures. Coated hollow core fibers and fiber lasers were used to demonstrate sparking at atmospheric condition. However, most of these fibers are limited by their damage thresholds to deliver sufficient ignition energies. Future research should be directed towards developing a multi pulse approach where multiple pulses are used to deliver the required ignition energies. The approach could involve use of the same fiber to deliver single low energy short duration pulse to create an initial spark followed by a longer pulse with higher energy for ignition. Investigations need to be directed towards optimizing the time duration between the pulses in order to deposit the maximum possible laser energy into the plasma.

Another focus of this work was on design and development of a multiplexed fiber laser ignition system. A multiplexer was designed and tested on two cylinders of a

sixteen cylinder CAT 3516C engine. Although the sparking was less than 100%, the demonstration showed a proof of principle of multiplexed fiber delivered laser ignition system. Although a single galvo was used in these experiments, a two galvo approach can be used in future multiplexer development for better control and launch of the laser beam into the fibers. This would help to reduce the misalignments observed during our experiments. Another approach for multiplexing the laser beam could be based on the use of electro-optic-modulators (EOMs) which can be used to switch the phase (polarization) of a laser beam passing through it by controlling the non linear crystal in the EOM with an electrical signal. These EOMs are stationary optical elements consisting of one or two pockels cell. The principle of EOM is based on pockels effect which is the modification of the index of refraction of a nonlinear crystal by an imposed electric field.

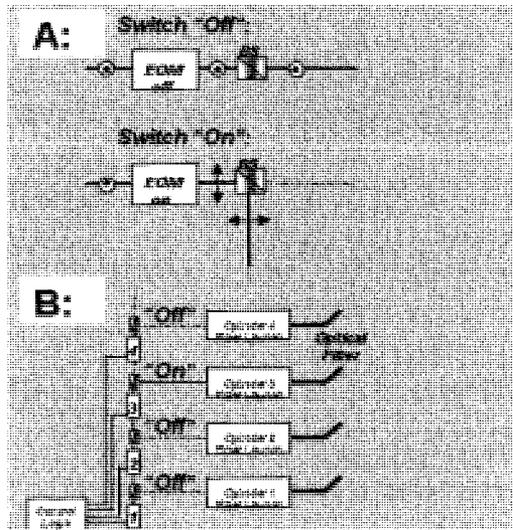


**Figure 6.1: a) A combination of an EOM and a beam splitter to change the beam direction, b) Multiple EOMs and beam splitters for multiplexing the laser beam from a single source to multiple fibers.**

A potential setup is shown in Fig 6.1a. The laser beam is indicated by the solid black line whereas the circles and the double arrows indicate the polarization state of the

laser beam. When the EOM is switched off, the laser passing through the EOM doesn't undergo a change in its polarization and hence is not redirected when passing through the beam splitter (polarizer). However, the polarization of the beam is changed when the EOM is switched on resulting in a change in the beam direction when it passes through the polarizer. So, for multiplexed operations, a series of EOMs and polarizers can be used to redirect the laser beam to the required fiber inputs depending on the "ON" or "OFF" state of the EOMs.

A second major focus of the work was on demonstrating Laser Induced Breakdown Spectroscopy (LIBS) to monitor equivalence ratio in a laser ignited engine. A single cylinder Cooperative Fuel Research (CFR) engine was used to demonstrate simultaneous laser ignition and in-cylinder LIBS, which was the first according to our knowledge. A linear correlation between  $H_{\alpha}/O$  and  $H_{\alpha}/N_{tot}$  intensity ratios with measured equivalence ratio (from a universal exhaust oxygen sensor installed at the exhaust) was shown for different compression ratios and energy levels. In this experiment, the LIBS intensity ratios corresponded to a specific spark location whereas the measured equivalence ratio was for the entire cylinder. However, in-cylinder equivalence ratio can be measured real time for methane-air mixture combustion in engines with the help of a tabulated map of intensity ratios for different equivalence ratios. Future work should be directed towards conducting careful combustion experiments to map the LIBS intensity ratios with pre-determined equivalence ratios of the methane-air mixtures (from accurate metering of fuel and air in a combustion test chamber).